Order Number 9325104

Novel results in the propagation of intense pulses and beams in nonlinear media

Gross, Barry, Ph.D.

City University of New York, 1993

U·M·I
300 N. Zeeb Rd.
Ann Arbor, MI 48106

NOVEL RESULTS IN THE PROPAGATION OF INTENSE PULSES AND BEAMS IN NONLINEAR MEDIA

by

BARRY GROSS

A Dissertation submitted to the Graduate Faculty in Engineering in partial fulfillment of the requirements for the degree of Doctor of Philosophy, The City University of New York.

1993

This manuscript has been read and accepted for the Graduate Faculty in Engineering in satisfaction for the dissertation requirement for the degree of Doctor of Philosophy.

March 26, 93
Date

Jamal S. Mansour
Chair of Examining Committee

3/26/93
Date

Gerard G. Lowen
Executive Officer

Professor Sven Hartmann

Professor Joseph Barba

Professor Paul Karmel

The City University of New York

Abstract

Novel Results in the Propagation of Intense Pulses and Beams in Nonlinear Media

by

Barry Gross

Adviser: Professor Jamal T. Manassah

The nonlinear partial differential equations describing the evolution of intense pulses or beams in various nonlinear media are solved by using a combination of spectral decomposition (F.F.T or multi-dimensional F.F.T) and adaptive Runge-Kutta techniques. In short, new results are obtained for:

1. Supercontinuum Generation
2. Nonlinear Self-Focusing
3. Pulse Propagation in Resonant Media
4. Beam Propagation in Resonant Media
5. Incoherent Signal Propagation

Acknowledgement

I wish to give my sincerest appreciation to Professor Jamal T. Manassah for his excellent guidance in all facets of my work. The time and effort expended as well as his scientific instruction were indispensable as was his emotional support during difficult times. I would also like to thank Prof. Conner for his help with the implementation and deeper understanding of Fast Fourier Transforms and Prof. Marinovic for assistance in constructing the necessary correlated random processes .

This work is dedicated to my mother Mrs. Shirley Beinhacker Gross whose love and emotional support was crucial to my development.

TABLE OF CONTENTS

1.1) Introduction

The propagation of intense pulses and beams in material media (not vacuum) manifest, during pulse evolution, different phenomena from those at low intensity . In the low intensity regime, a spatial beam undergoes diffraction while a temporal pulse undergoes dispersion. In a resonant medium, a low intensity beam will also undergo linear absorption (Beer's Law). When the field is intense enough, the field changes the material index of refraction which then modifies the propagation of the incident field. This process explains such processes as Self-Phase Modulation (Spectral Broadening), Self-Focusing (& Self-Defocusing) and Multi-Wave Mixing. In the resonant medium, intense fields cause other nonlinear processes such as gain saturation, gain dispersion and coherent transients effects to occur. It is our intention to study the propagation of intense (ultrashort) pulses and beams in nonlinear media. The motivation of our study is that Ultrashort pulses are important in Ultrafast Spectroscopy and High Speed Communications.

1.2) Thesis Outline

In 2.1, the relevant processes unique to intense pulses are explained. The classical model describing the Self-Phase Modulation effect is presented and an explanation of the supercontinuum (spectral broadening) is given. The model is systematically made more realistic by adding terms (higher order nonlinear processes) to the classical description and is used to explain observed anomalies in pulse propagation in the femtosecond regime. The classical model of the self-frequency shift is presented which explains the linear red-shift in soliton propagation. The full model is introduced and numerically integrated for typical fiber parameters. Section 2.2 deals with propagation in the normal dispersion regime. In 2.3, the model is applied to the anomalous dispersion regime. Qualitative differences in the two regimes are observed and explained.

In 3.1, the propagation of an intense axially symmetric beam in a Kerr medium is explored. Known semi-quantitative approximations in the aberrationless approximation are presented . The results of a numerical simulation are presented and compared to the approximation methods. By solving the relevant equations for various input powers, regions in which the approximation methods give accurate results are given. Further comments on their predictive powers are presented.

In 3.2, the propagation of spatial beams in a Kerr medium is extended to nonsymmetric beams (elliptic gaussian beams). This allows us to study the transition from the 2D (spatial soliton) to the 3D (self-focusing) regime by varying the ellipticity. The semi-quantitative expressions are extended to the elliptic case and

presented here. They result in a set of coupled ordinary differential equations (O.D.E's) which give qualitative understanding of the propagation. In 3.3, a numerical investigation is done by varying both the initial intensity and ellipticity. Comparisons to the approximation methods are again explored and new features not manifested in an axially symmetric beam are observed and explained.

In 4.1, we introduce the formalism required to describe pulse propagation in resonant media. This formalism, which couples the Bloch equations and the inhomogeneous Maxwell equation allows the study of propagation in optically thick materials. In 4.2, the formalism is applied to a rigorous study of Erbium Doped Fiber Amplifiers. The full model including active and passive (fiber) elements is presented and integrated and the results compared to previous models which phenemologically describe the active medium.

In 5.1, the study of a 2D C.W. beam propagating in a resonant medium is undertaken. This model extends the earlier examined Kerr model. The Bloch equations are suitably modified and an evolution equation developed. The model is shown to reduce to the Kerr model under certain achievable conditions. In 5.2, a variational approximation scheme is used to model the beam in the presence of a Kerr medium with index saturation which is equivalent to the numerical model without absorption losses. Beam parameter equations are developed and numerically integrated. In 5.3, the numerical simulations are presented by varying the pulse medium detuning (pulse center frequency - medium resonance frequency). It

is shown that various different propagation regimes are obtained for different values of the detuning.

In 5.4, the model is extended to the 3D axially symmetric case. The propagation equation is modified and presented. In 5.5, a variational procedure is again implemented to give a qualitative understanding of the problem. In 5.6, the numerical results are presented for a fixed detuning and various input powers. Catastrophic self-focusing is shown not to occur. Various properties of the beam evolution are elucidated and the waveguiding ability of this geometry demonstrated.

In 6.1, a study of incoherent signals is initiated and motivation presented. A numerical procedure is presented in detail that allows one to study the evolution of the signal coherence time in an optical fiber. The model is exhaustive and includes all the relevant nonlinear and dispersive processes. The calculation is checked against known analytic models and conclusions are drawn. We prove the possibility of significant coherence time compression and point out advantages and disadvantages of this compression scheme.

In 6.2, a study of a quasi-monochromatic incoherent 2D signal is undertaken. The similarities and differences to the previous calculation are discussed and quantitative and qualitative differences are observed and explained. Implications to the time domain are given.

In 7, the numerical algorithms used are explained in detail. Since the programs are highly modular, the subroutines are first presented and the driver functions are explained for each problem.

In 8, we summarize our results.

2.1) Supercontinuum Generation (Historical Perspective)

The ability of an intense field to affect the medium by changing the effective index of refraction which in turn affects the field as it propagates in the medium is the central problem in nonlinear optics. In the present context of supercontinuum generation, the intense pulse is considered planar. In this way, self-focusing effects will not effect the supercontinuum generation. That the self-focusing indeed can effect the supercontinuum is known but is not considered in this section. Under these conditions, the medium index of refraction is $n=n_0 + n_2 I$. Noting that the intensity is a function of time, a self-induced frequency chirp is created. Since the instantaneous frequency of the pulse is related to the time derivative of the phase (which possesses a nonlinear chirp), instantaneous frequencies which themselves are functions of the reduced time are created. This, as will be shown, is the standard mechanism of spectral broadening. In the simple model, the broadening depends linearly on the field intensity and propagation distance and is inversely proportional to the pulse duration.

The possibility, of an intense pulse being able to self-modulate its phase (frequency) was explored early in the history of nonlinear optics [1-6]. The first experimental observation of the spectral broadening process was observed [7] in the output of laser pulses propagating in liquids. In [8] , the spectral broadening effect was magnified using pico-second pulses giving a spectral bandwidth ~ (10,000 cm^{-1}).

The simplest model showing the essential features of spectral broadening is describable by

$$\frac{\partial \phi}{\partial V} = \frac{i \varepsilon K}{2}\left[|\phi|^2 \phi\right] \qquad (2\text{-}1.1)$$

where $E = E_0\,\phi$, $\varepsilon = \dfrac{n_2 |E_0|^2}{n_0}$, $V = \dfrac{z}{v_g\,\tau}$, $U = \dfrac{z}{v_g\,\tau} - \dfrac{t}{\tau}$,

τ is the initial pulse width, v_g is the group velocity at the pulse center frequency, n_0 is the linear index of refraction, n_2 is the Kerr nonlinear index of refraction including geometric factors resulting from the transverse averaging of the mode over the fibre cross-section, E_0 is the amplitude of the electric field of the incoming pulse, $K = \omega_0\,\tau$, and ω_0 is the pulse center frequency.

If $\phi = a\exp(i\alpha)$ we obtain

$$\frac{da}{dV} = 0, \qquad \frac{d\alpha}{dV} = \frac{K\varepsilon a^2}{2} \qquad (2\text{-}1.2)$$

which integrates to

$$a(U,V) = a(U,0), \qquad \alpha(U,V) = \frac{K\varepsilon(a(U,0)^2)V}{2} \qquad (2\text{-}1.3)$$

From these equations and the fact that the instantaneous frequency shift defined by $-\dfrac{\partial \alpha}{\partial U}$

we see that a nonlinear frequency chirp develops. From the phase expression, we have

$$-\frac{\partial \alpha}{\partial U} = K\varepsilon UV\exp(-U^2) = (\omega_0 - \omega)\tau \qquad (2\text{-}1.4)$$

For U>0, the instantaneous frequency is less than the center frequency and for U<0, the instantaneous frequency is greater than the center frequency.

Therefore, the leading edge of the pulse is red-shifted and the trailing edge is blue-shifted. An important application [9-10] of the spectral broadening phenomenon is to feed the modified pulse through an external dispersive delay system which is designed to compensate the self induced phase modulation. As can be seen using spectral analysis [11-13] , this in turn compresses the pulse duration. This scheme along with recent modification has produced the shortest optical pulses to date [14-16] .

The superbroadened spectrum for a gaussian envelope has a spectral bandwidth $\Delta\omega\tau \approx K\varepsilon V$ and the spectrum possesses frequency modulations $\Delta\omega_m\tau \approx 4\pi$. The frequency modulation is explained by noting that there are two values of U (of same sign) which give the same instantaneous frequency. These traveling waves of the same instantaneous frequency but differing phase will combine constructively or destructively depending on the phase delay. This yields the modulation effect observed in the spectrum.

The simple theory works well in describing pulses on the pico-second scale, but experimental results using femtosecond pulses show [17] that the spectrum is no longer symmetric but shows an asymmetry to the blue (anti-stokes) side. On the other hand, experimental work [18] on soliton propagation shows that the spectrum generates a large red shifted spectral component (stokes). Such complications in the super broadened spectrum can not be explained by the simple S.P.M theory.

If we neglect dispersion effects for the moment, the observed anti-stokes blue shift can be accounted for [19] by correcting in part the slowly varying envelope approximation (Self Steepening). Using an operator technique [20] , the corrected equation to first order in 1/K is

$$\frac{\partial \phi}{\partial V} = \frac{i \varepsilon K}{2}\left[|\phi|^2 \phi - \frac{i}{K}\frac{\partial}{\partial U}\left(|\phi|^2 \phi \right) \right] \qquad (2\text{-}1.5)$$

which shows that the correction becomes important for femto-second pulses. Analytical solutions for a gaussian (or hyperbolic secant) pulse can be found [21] which show that the self steepening causes an asymmetry to the blue. This is a consequence of a delay in the pulse amplitude ($n_2 > 0$). The trailing edge sees a more intense field and the maximum blue shift increases and similarly the decrease of the field intensity at the leading edge causes the maximal red shift to decrease.

To explain the results of the soliton experiments [22], it is first observed that the theory until now assumes that the medium response is instantaneous. In truth, the medium response is not instantaneous but has a finite response time. When the optical pulse is in the femtosecond regime, the pulse is not much longer than the response and the part of the pulse that excites the medium is not the part of the pulse which feels the medium response. The effective nonlinear index of refraction is given as

$$\Delta n(z,t) = \int_{-\infty}^{t} n_2(z,t-t')|E(z,t')|^2 \, dt' \qquad (2\text{-}1.6)$$

and the induced phase by

$$\Delta\Theta(z,t) = \frac{\omega}{c}\int_0^z \Delta n(z,t)\, dz \qquad (2\text{-}1.7)$$

One may expand the kernel in the nonlinear index equation [22], and to first order in the expansion obtain

$$\frac{\partial \phi}{\partial V} = \frac{i\varepsilon K}{2}\left[|\phi|^2\phi - \frac{i}{K}\frac{\partial}{\partial U}\left(|\phi|^2\phi\right) + \gamma\phi\frac{\partial}{\partial U}|\phi|^2\right] \qquad (2\text{-}1.8)$$

where $E = E_0\,\phi$, $\varepsilon = \dfrac{n_2|E_0|^2}{n_0}$, $\gamma = \dfrac{c_1}{\tau}$, $V = \dfrac{z}{v_g\,\tau}$, $U = \dfrac{z}{v_g\,\tau} - \dfrac{t}{\tau}$,

τ is the initial pulse width, v_g is the group velocity at the pulse center frequency, n_0 is the linear index of refraction, n_2 is the Kerr nonlinear index of refraction including geometric factors resulting from the transverse averaging of the mode over the fibre cross-section, E_0 is the amplitude of the electric field of the incoming pulse, $K = \omega_0\,\tau$, ω_0 is the pulse center frequency, and c_1 is the first moment in the expansion of the delayed response Kernel of the Raman Scattering .

The solution to this equation using multiple scale technique [23-25] has been accomplished. The magnitude of the stokes anti-stokes asymmetry is lessened in the presence of a finite relaxation time. Physically, the finite response time of the medium is due to the

nuclear vibrations (Raman Scattering). The field photon excites the atom which undergoes vibration. This vibratory mode, quantum mechanically, is an optical phonon. Using the concept of energy (momentum) conservation, the creation of the optical phonon down shifts the optical photon frequency leading to a red-shift. To leading order the Raman Scattering is mathematically equivalent to the medium possessing a finite response time.

Raman Scattering plays a dominant role in the propagation of optical solitons. The frequency shift due to Raman Scattering limits the effectiveness of using solitons as information packets in high speed communication systems. In a simple model quantifying the self-frequency shift, we assume that self-steepening and higher order dispersion are neglected. Then the field intensity is unchanged during pulse propagation but the phase is a complex function of the propagation. The result in this limit [25] is

$$\langle(\omega_0 - \omega)\tau\rangle = \frac{4}{15}\gamma\varepsilon KV \qquad (2\text{-}1.9)$$

For a soliton, the self-frequency shift scales as $1/\tau^4$ since then the field is inversely proportional to the pulse duration . The observation of the self-frequency shift in soliton propagation in optical fibers confirms the above approach .

Modelling the Raman process as a simple response delay is an approximation valid if the pulse spectra is much narrower than the Raman linewidth. When this is not the case, the response kernel must be expanded to all orders [26]. For fused silica, the Raman line ~10^{13} Hz. so that a transform limited pulse of 20 fsecs. would overlap the

Raman transition. Therefore to model the propagation of femtosecond pulses which undergo spectral broadening, the linear approximation to the Raman susceptibility is inappropriate and a better model of the Raman scattering process is required.

Until now, we have neglected material dispersion. In general, the inclusion of material dispersion into the supercontinuum model prohibits an analytic solution and one must resort to numerical simulations [27,28] . Dispersion effects in the normal dispersion regime will cause the temporal profile to broaden and thus limit the extent of the supercontinuum. In the anomalous dispersion regime, the Kerr effect couples with the Group Velocity Dispersion (G.V.D) to create solitons which are periodic states valid for special initial conditions of the field. These soliton states are derivable from a powerful technique known as the Inverse Scattering Transform [29-30] . In this work, an exhaustive model [31] of the optical fiber is developed which includes all the above processes. The equation is numerically integrated yielding information on the spectral and temporal properties. We neglect transverse effects since the propagation distances are less than the self-focusing distances for typical fiber diameters.

2.2) Supercontinuum Generation (Normal Dispersive Regime) [b]

If we define the Fourier transform of the envelope as:

$$\tilde{\phi}(\Omega,V)=\mathbf{F}[\phi(U,V)]=\frac{1}{\sqrt{2\pi}}\int_{-\infty}^{\infty}\exp(i\Omega U)\,\phi(U,V)\,dU$$ then the differential equation for $\tilde{\phi}$ is [31]

$$\frac{\partial\tilde{\phi}(\Omega,V)}{\partial V}=\frac{i\varepsilon K}{2}\left(1-\frac{\Omega}{K}\right)\mathbf{F}\left[|\phi(U,V)|^2\phi(U,V)\right]$$
$$+\frac{i\varepsilon K}{2}\mathbf{F}\left\{\phi(U,V)\mathbf{F}^{-1}\left[\chi_R(\Omega)\mathbf{F}\left[|\phi(U,V)|^2\right]\right]\right\}$$
$$+i\left(v_g\tau\right)\sum_{k=2}^{\infty}(-1)^k\frac{\beta^{(k)}\Omega^k}{k!\,\tau^k}\tilde{\phi}(\Omega,V) \qquad (2\text{-}2.1)$$

Here $\beta^{(j)}=\left.\frac{d^j k}{d\omega^j}\right|_{\omega=\omega_0}$

where k is the wave number. The first and second terms account for Kerr and Self-Steepening effects, the third term corresponds to the Raman Scattering and the terms in the summation give rise to the chromatic dispersion terms to all orders. We analyze this equation, keeping only the $\beta^{(2)}$ and $\beta^{(3)}$ terms of the chromatic dispersion series.

To account for the true Raman response, we use the generalized Raman Scattering susceptibility which can be approximated in the harmonic oscillator model [32] for the molecular vibrations by:

$$\chi_R(\Omega) = \frac{\chi_0(\Omega_R \Gamma_R)}{\Omega_R^2 - \Omega^2 + i\Gamma_R \Omega} \qquad (2\text{-}2.2)$$

where Ω_R is the Raman shift normalized to the pulse width i.e molecular vibrational frequency multiplied by τ. For example, for fused silica, Ω_R =(15.1 THZ)x ($2\pi\tau$). Γ_R is the normalized phenomological line width. $\Omega = (\omega_0 - \omega)\tau$. To match this susceptibility to the moments expansion, we Taylor expand it in Ω:

$$\chi_R(\Omega) = c_0 - i\frac{c_1 \Omega}{\tau} - \frac{c_2 \Omega^2}{2\tau^2} + \ldots\ldots \qquad (2\text{-}2.3)$$

then c_0 and γ can be identified as:

$$c_0 = \chi_0 \frac{\Gamma_R}{\Omega_R} \qquad \text{and} \qquad \frac{c_1}{\tau} = \gamma = \chi_0 \frac{\Gamma_R^2}{\Omega_R^3}$$

For fused silica, $c_0 \approx 0.28$, $\chi_0 \approx 0.275$ and $c_1 \approx 3\,fs$.

In Fig. 2-1, we plot the imaginary part of the Raman susceptibility and compare it to the linear (first moment) model. The linear Raman model is the tangent to the Lorentzian model at the origin and therefore gives good results for narrow bandwidth pulses. The evolution equation is integrated by combining F.F.T and adaptive Runge-Kutta techniques to advance the solution. The accuracy of the numerical method was tested by verifying:

1) The energy invariant was maintained to 1 per 1,000,000.
2) The solution involving dispersion alone was recreated to 1/1000.
3) The analytic solution [24,25] without dispersion was recovered to 1/1000.

Results

1) In fig. 2-2, the spectral distribution of the pulse is calculated for different propagation distances for various initial intensities. The pulse spectral distribution is obtained by taking the square of the absolute value of the Fourier transform of the pulse envelope, i.e., $|\tilde{\varphi}(\Omega, V)|^2$. The important features in the pulse spectrum are that: (i) the spectral extent increases with εV, (ii) for a particular value of εV the spectral extent decreases with a decrease in the value of ε , (iii) as εV increases the spectrum is more asymmetric between the Stokes and Anti-Stokes sides, and (iv) this asymmetry is less pronounced as the dispersion effects become more important.

2) In fig. 2-3, the amplitude of the temporal profile of the pulse is calculated for different propagation distances for various intensities. The important features in the temporal profiles are: (i) for a particular value of εV, the temporal extent decreases with ε, (ii) the asymmetry due to self steepening decreases as ε decreases. (iii) The pulse undergoes scattering at the self-steepened edge as dispersive effects become present.

3) In fig. 2-4, the ratio of the integrated spectrum on the Stokes side over the total integrated spectrum as function of εV for different values of the pulse initial energy is studied. We note modulation of the total energy in each band as a function of εV. This is due to the linear increase in the number of peaks in the spectra as the pulse propagates.

4) In figs. 2-2 and 2-3, we also note the modification to the evolution if the self-steepening term, the $\beta^{(3)}$ term, or the Lorentzian

Raman term were separately omitted from the differential equation. The modification is more apparent for higher intensity since the spectral broadening manifests itself most prominently at these intensities.

5) The average frequency shift for the spectral distribution, defined as:

$$\overline{\Omega} = \langle (\omega_0 - \omega)\,\tau \rangle = \frac{\int_{-\infty}^{\infty} \Omega \left|\tilde{\phi}(\Omega, V)\right|^2 d\Omega}{\int_{-\infty}^{\infty} \left|\tilde{\phi}(\Omega, V)\right|^2 d\Omega}$$ is studied.

For small εV, and neglecting the self-steepening term, this self-frequency shift in the linear Raman model is given by [24-25]: $\overline{\Omega} \approx \frac{4}{15}(\gamma K \varepsilon V)$ i.e. the shift is towards the red. But we note that this shift can be towards the blue for higher energy pulses. In such an instance the effects of self-steepening and $\beta^{(3)}$ can dominate over the Raman effect. We illustrate this last point by plotting, in fig. 2-5, the modification to this shift if the self-steepening term, the $\beta^{(3)}$ term, or the Lorentzian Raman term were separately omitted from the differential equation . Furthermore, even in those instances where the shift is towards the red (i.e. the lower energy pulses) , then it is not linear in the distance of propagation due to modifications in the temporal amplitude of the pulse.

2.3) Supercontinuum Generation (Anomalous Dispersive Regime) [f]

It was shown earlier that the leading part of the spectrum broadened pulse due to Kerr nonlinearity undergoes a red-shift and the trailing edge undergoes blue-shift. In the normal dispersive region, the red-shifted components move with higher group velocity than their blue-shifted components leading to pulse spreading. The reverse occurs in the anomalous dispersion regime. Therefore, the pulse undergoes temporal compression. After a while, the pulse becomes distorted and a complicated interplay between the Kerr effect and the anomalous dispersion effect occurs. For certain well defined initial sech pulses (i.e. N an integer), the propagation is periodic. These well defined modes of propagation are known as solitons and the analytical theory using the inverse scattering transform gives detailed information on these soliton states.

The theoretical prediction of soliton propagation was first given by Hasegawa and Tappert [30]. Experimental verification of soliton propagation in optical fibers was first obtained by Mollenaur et al [33]. Soliton propagation as a means of high speed optical communication due to its stable temporal pulse shape was quickly realized [30] . However, the self-frequency shift due to Raman Scattering limits the usefulness of this scheme over long distances since the pulse spectrum drifts into another band causing signals to overlap.

Furthermore, in the anomalous dispersive regime, the spectrum will never shift towards the blue since the pulse undergoes initial compression and the Raman induced frequency shift scales as $1/\tau^4$

for a soliton, the Raman induced frequency shift is stronger and is expected to overcome the blue shifts of the self-steepening effects and third order chromatic dispersion.

The model used to investigate the propagation of intense femto-second pulses in the anomalous dispersive regime is substantially the same as the normal dispersive regime. It should be noted that some models along our lines appear in the literature but are not exhaustive [34] .In this frame work, soliton units are the natural choice. In these units:

$$\frac{\partial \tilde{\phi}(\Omega,\bar{z})}{\partial \bar{z}} = i\,\mathbf{N}^2\left(1-\frac{\Omega}{K}\right)\mathbf{F}\left[\left|\phi(U,\bar{z})\right|^2\phi(U,\bar{z})\right]$$
$$+i\,\mathbf{N}^2\mathbf{F}\left\{\phi(U,\bar{z})\mathbf{F}^{-1}\left[\chi_R(\Omega)\mathbf{F}\left[\left|\phi(U,\bar{z})\right|^2\right]\right]\right\}$$
$$-i\left(\frac{\Omega^2}{2}+\frac{\delta\,\Omega^3}{6}\right)\tilde{\phi}(\Omega,\bar{z}) \qquad (2\text{-}3.1)$$

where $\bar{z}=\dfrac{z}{z_0}=\dfrac{z\left|\beta^{(2)}\right|}{\tau_*^2}$, $\delta=\dfrac{\beta^{(3)}}{\left|\beta^{(2)}\right|\tau}$, and $\mathbf{N}^2=\dfrac{\pi\tau^2}{\lambda\left|\beta^{(2)}\right|}n_2E_0^2$, i.e. the distance is measured in units of the dispersion length and the nonlinear coupling is measured in the units used for determining the order of a soliton. Note that we keep only the $\beta^{(2)}\,(<0)$ and $\beta^{(3)}$ terms of the chromatic dispersion series. The generalized Raman Scattering susceptibility can be approximated using the same harmonic oscillator model for the molecular vibrations :

$$\chi_R(\Omega) = \frac{\chi_0 \Gamma_R \Omega_R}{\Omega_R^2 - \Omega^2 + i\Gamma_R \Omega}$$ where Ω_R is the Raman shift normalized to the pulse width, i.e the molecular vibrational frequency multiplied by τ, and Γ_R is the normalized phenomological line width.

In what follows we consider incoming pulses with sech shape but with energies larger than that of the fundamental soliton (i.e. N>1).

1) In fig. 2-6, the pulse amplitude as a function of the comoving normalized time is studied for different soliton orders and propagation distances. The pulse narrows initially, then breaks up and a daughter pulse, whose delay increases with the distance of propagation, is formed. The delay of this daughter pulse is a result of the lower velocity of the Raman generated frequency components that form it. We note further that this daughter pulse behaves like a fundamental soliton. The number of these daughter-solitons would increase with an increase of the incoming pulse energy (higher N).

2) To see how each of the physical effects contributes to the signal time profile at the exit planes., we plot, in fig. 2-7, the results of the full theory and compare them to the different cases of the full theory minus one of the physical effects. It is clear that the Raman effect is responsible for the shift to the red, while the self-steepening and the $\beta^{(3)}$terms pull the soliton to the blue, i.e. they contribute a blue shift to the spectral distribution.

3) In fig. 2-8, we compare the results of the full theory to those of the Nonlinear Schrodinger equation (N.L.S). The cases illustrated

correspond to the higher order solitons of the N.L.S theory. Our algorithm's predictions for the higher order solitons is accurate to better than one part per thousand with the analytical results.

4) We compare, in fig. 2-9, the results of our model to those of ref.34 which uses the linear Raman model and twice the self-steepening contribution (which is derived from S.V.E.A.) and note that important quantitative differences exist. The details of the different contributions in the model can make important quantitative differences.

5) The spectral distribution of the pulse after propagation through the nonlinear medium is studied in fig. 2-10. The important features of the spectrum are (i) the spectral extent increases with distance, (ii) as distance increases the spectrum is more asymmetric between the Stokes and Anti-Stokes sides, and (iii) the spectral line representing the daughter soliton shifts more to the Stokes side as the distance increases.

6) To more clearly see the difference of the supercontinuum in the normal and anomalous dispersion region, we plot, in fig. 2-11, the spectral distribution for the same parameters except that we change the sign of $\beta^{(2)}$. We note that the two spectra are qualitatively quiet different. The main reason is that in the normal GVD regime, the $\beta^{(2)}$ term disperses the pulse thus narrowing the spectrum while in the anomalous regime this term compresses the pulse initially and later in conjunction with SIRS leads to its breakdown thus resulting in a much broader supercontinuum.

7) The average frequency shift of the spectral distribution is studied in fig. 2-12, and the results of the full theory compared with those of the truncated versions.We note two regimes in this figure, the first where the parameters of the initial pulse determine the value of the self-frequency shift, and the second where those of the daughter soliton do. The much shorter soliton duration in the second region accounts for the appreciable difference in the value of the shift since the shift scales as $1/\tau^4$. Furthermore the higher order processes cannot be ignored as the stokes spectral line moves far from the center frequency.

FIGURE CAPTIONS

Fig. 2-1 The imaginary part of the Raman susceptibility for "glass" is plotted as function of the normalized frequency difference $[(\omega_0 - \omega)\tau]$.

Material relaxation time $\approx 3\,fs$. For τ=50 fs., $\Omega_R = 4.76$, $\Gamma_R = 4.85$.

(i) the Lorentzian model (ii) the Linear model.

Fig. 2-2 The spectral distribution is plotted as a function of the frequency difference multiplied by the pulse duration (i.e., the normalized frequency difference).

*Pulse Parameters: τ=50 fs.. λ_0=1 μm.

*Material parameters: $\Omega_R = 4.76$, $\Gamma_R = 4.85$

$$\beta^{(2)} = 2\times10^{-26}\ \mathrm{s}^2/\mathrm{m};\ \beta^{(3)} = 5\times10^{-41}\ \mathrm{s}^3/\mathrm{m}.$$

[At $\lambda_0 = 630\,nm$ $\beta^{(2)} = 5.2\times10^{-26}\ \mathrm{s}^2/\mathrm{m}$; $\beta^{(3)} = 2.5\times10^{-41}\ \mathrm{s}^3/\mathrm{m}$.]

$$\mathbf{N}^2 = \frac{\pi\tau^2}{\lambda\beta^{(2)}} n_2 E_0^2$$

a. The model incorporates self-steepening, and Raman Scattering but not chromatic dispersion.

b, c, d, e The model incorporates self-steepening, Raman Scattering and chromatic dispersion $\left(\beta^{(2)} \text{ and } \beta^{(3)} \text{ terms}\right)$.

b. $\varepsilon = 0.7023\times10^{-2}$ or $\mathbf{N}^2 = 4000$. ($\varepsilon V = 1$ corresponds to z=1.4 mm),

c. $\varepsilon = 0.7023\times10^{-3}$ or $\mathbf{N}^2 = 400$. ($\varepsilon V = 1$ corresponds to z=1.4 cm),

d. $\varepsilon = 0.7023 \times 10^{-4}$ or $\mathbf{N}^2 = 40.$ ($\varepsilon V = 1$ corresponds to z=14 cm) .

e. $\varepsilon = 0.7023 \times 10^{-5}$ or $\mathbf{N}^2 = 4.$ ($\varepsilon V = 1$ corresponds to z=1.4 m) .

[For $n_2 = 3 \times 10^{-22}\,(mks)$, $n_0 = 1.5$ and $\varepsilon = 0.7 \times 10^{-5}$, the value of $E_0 = 1.8 \times 10^8\, V/m$ which corresponds to a maximum power flux $\approx 10^{10}\, W/cm^2$]

Fig. 2-3 The field amplitude as a function of the reduced time is plotted. The labels a,b,c,d and e represent the same field intensities as in figure 2-2.

Fig. 2-4 The ratio of the integrated Stokes spectral intensity over the total integrated spectral intensity is plotted as a function of εV. The same parameters for the nonlinear material and the pulse as those of fig. 2-2 are used. The a,b,c,d,e labeling of the graphs refer to the same value of ε as those in fig.2-2. In each graph the different curves refer to the following cases:

(i) The full model

(ii) The full model minus the self-steepening term.

(iii) The full model minus the Raman term.

(iv) The full model minus the $\beta^{(3)}$ term.

Fig. 2-5 The normalized self-frequency shift is plotted as a function of εV. The same parameters and labeling as those of fig. 2-4 are used. For τ=50 fs., $\langle \Omega \rangle = 1$ corresponds to a frequency shift of $3.18 \times 10^{12}\, Hz$.

Fig. 2-6 Evolution of the pulse with initial sech shape propagating in the anomalous GVD region.

*Pulse Parameters: τ=180 fs.. λ_0=1.55 μm.

*Material parameters: $\Omega_R = 17.136$, $\Gamma_R = 17.46$

$$\beta^{(2)} = -2\times10^{-26}\ s^2/m;\ \beta^{(3)} = 10^{-40}\ s^3/m.$$

a) N^2= 4 ; b) N^2=9 ; c) N^2=16.

The exit planes for cases a,b, and c are respectively $\bar{z} = 4$, $\bar{z} = 2$, and $\bar{z} = 1$.

Fig. 2-7 Signal profile at the exit plane for the same pulse and materials parameters of fig.2-6. (i) full model; (ii) full model minus the $\beta^{(3)}$ term ; (iii) full model minus the Raman term; (iv) full model minus the self-steepening term.

a) N^2= 4 ; b) N^2=9 ; c) N^2=16.

Fig. 2-8 Signal profile at the exit plane for the same pulse and materials parameters of fig.2-6. (i) full model; (ii) Higher order solitons of the nonlinear Schrodinger equation.

a) N^2= 4 ; b) N^2=9 ; c) N^2=16.

Fig. 2-9 Signal profile at the exit plane for the same pulse and materials parameters of fig.2-6. (i) present full model; (ii) model of ref.34.

a) N^2= 4 ; b) N^2=9 ; c) N^2=16.

Fig. 2-10 The spectral distribution is plotted as a function of the frequency difference multiplied by the pulse duration (i.e., the normalized frequency difference) for the same pulse and materials parameters of fig.2-6.

a) $N^2 = 4$; b) $N^2 = 9$; c) $N^2 = 16$.

Fig. 2-11 The spectral distribution is plotted as a function of the normalized frequency difference at the exit plane. (i) same parameters as fig.2-6 (ii) same except that $\beta^{(2)} > 0$.

a) $N^2 = 4$; b) $N^2 = 9$; c) $N^2 = 16$.

Fig. 2-12 The normalized self-frequency shift is plotted as a function of the normalized distance. The same parameters and labeling as those of fig. 2-7 are used. The self-frequency shift of the NLS case is identically zero.

a) $N^2 = 4$; b) $N^2 = 9$; c) $N^2 = 16$.

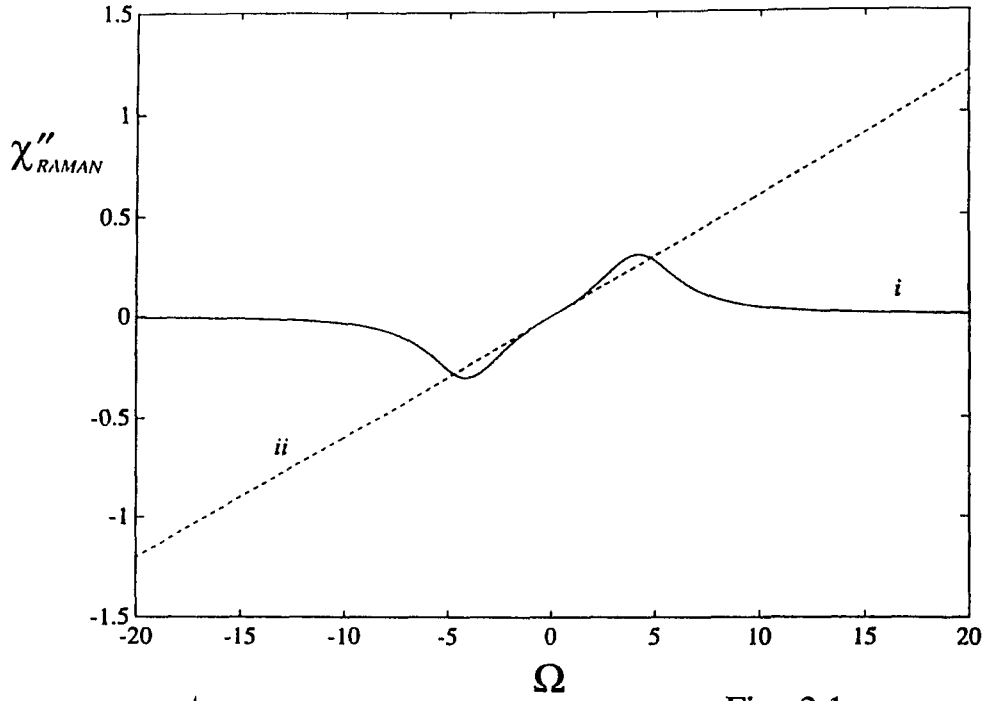

Fig. 2.1

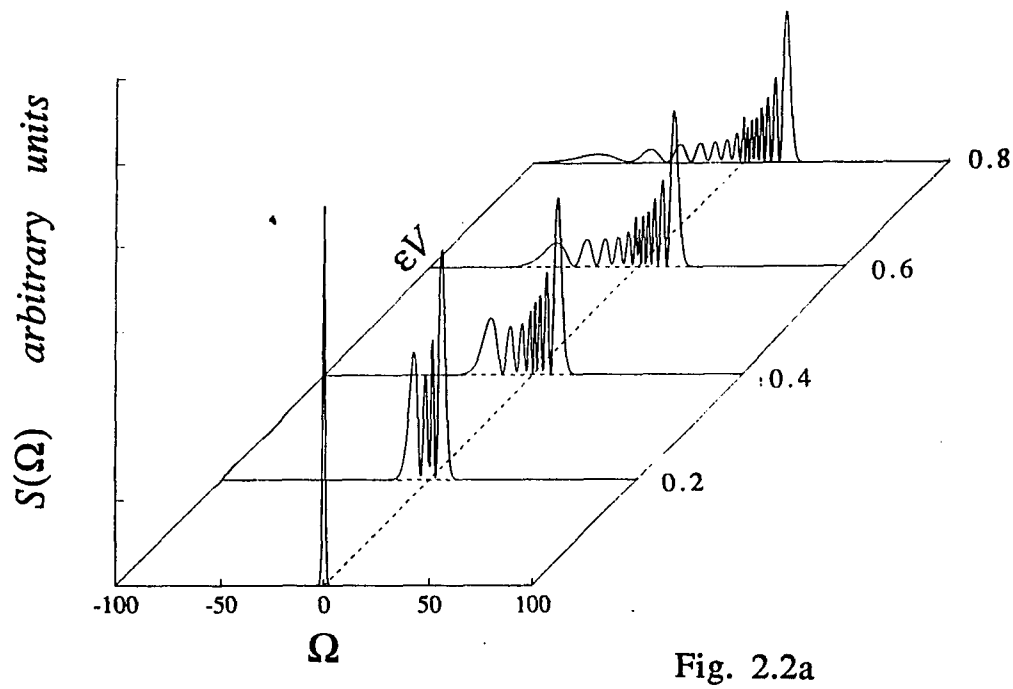

Fig. 2.2a

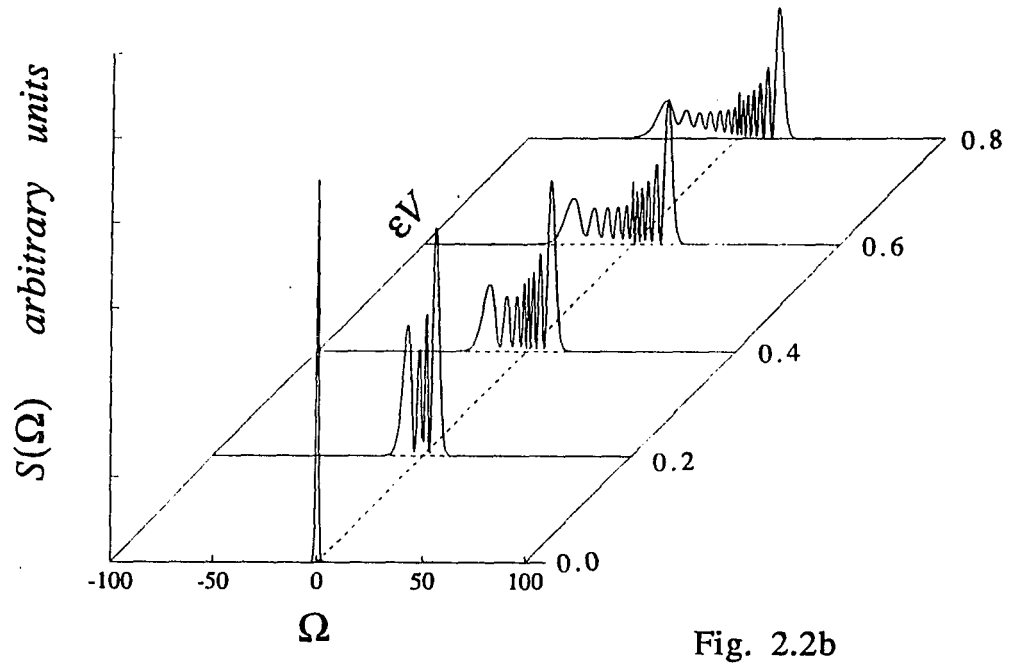

Fig. 2.2b

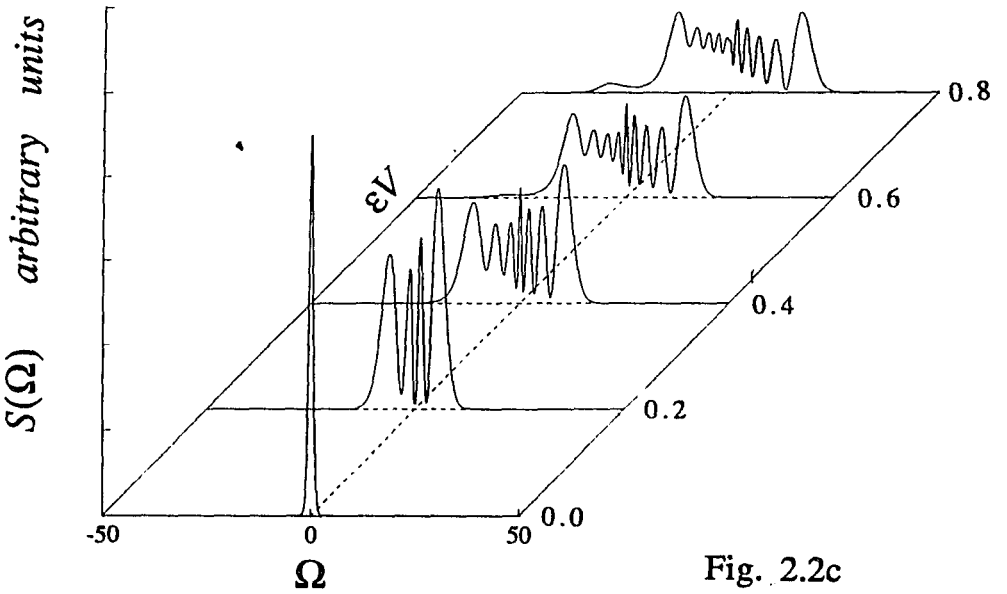

Fig. 2.2c

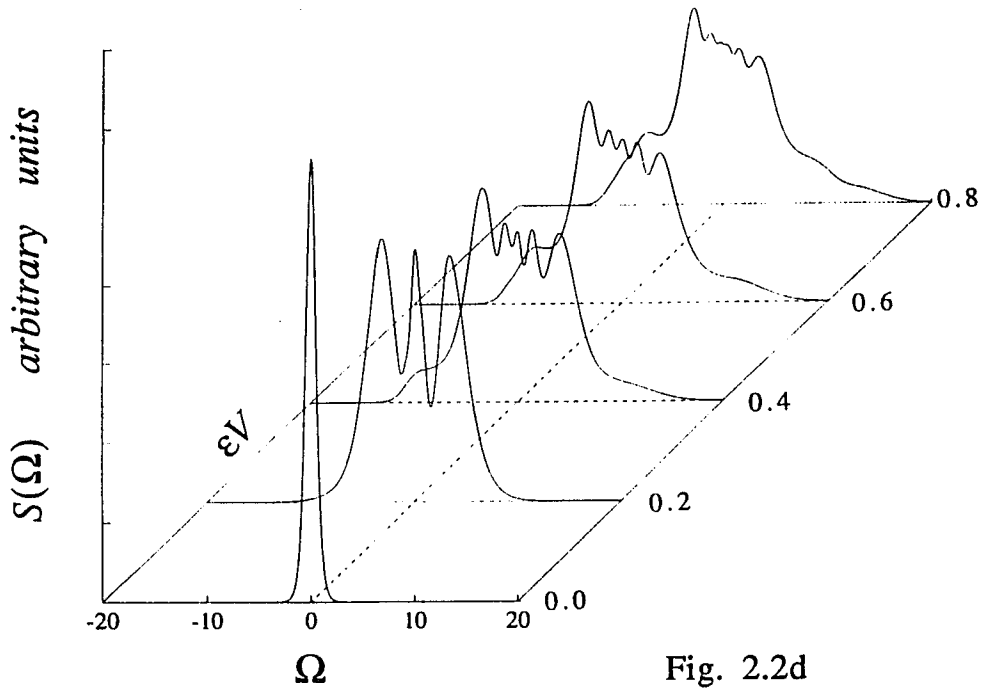

Fig. 2.2d

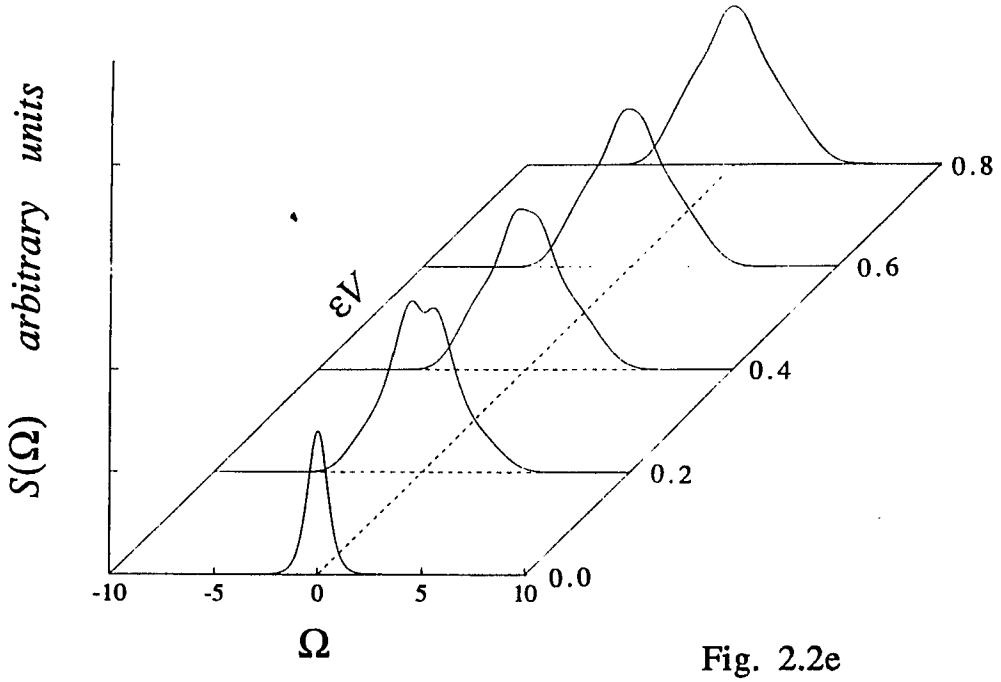

Fig. 2.2e

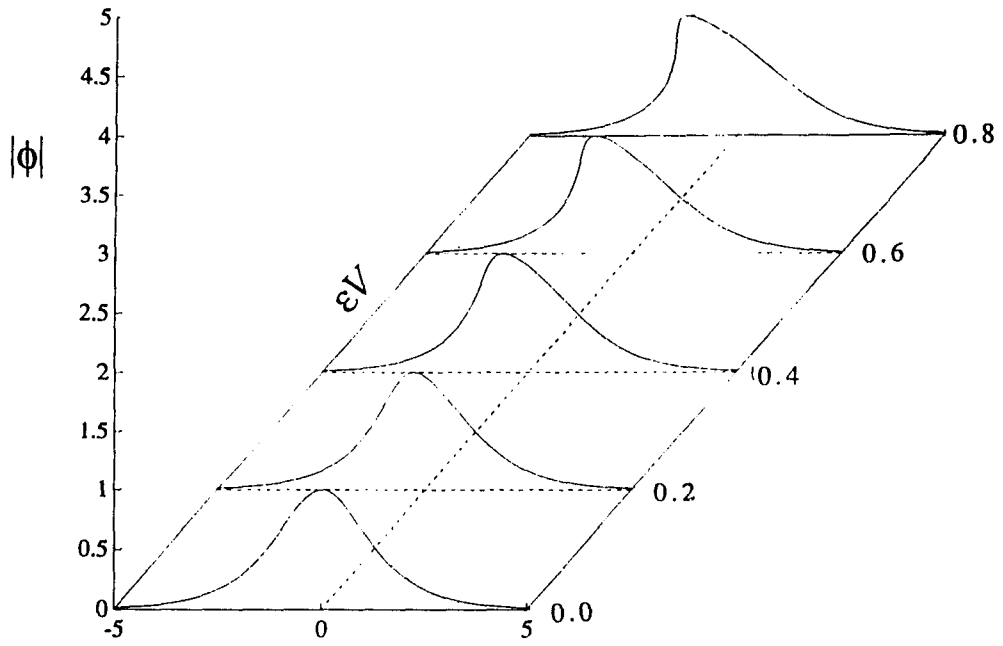

Fig. 2.3a

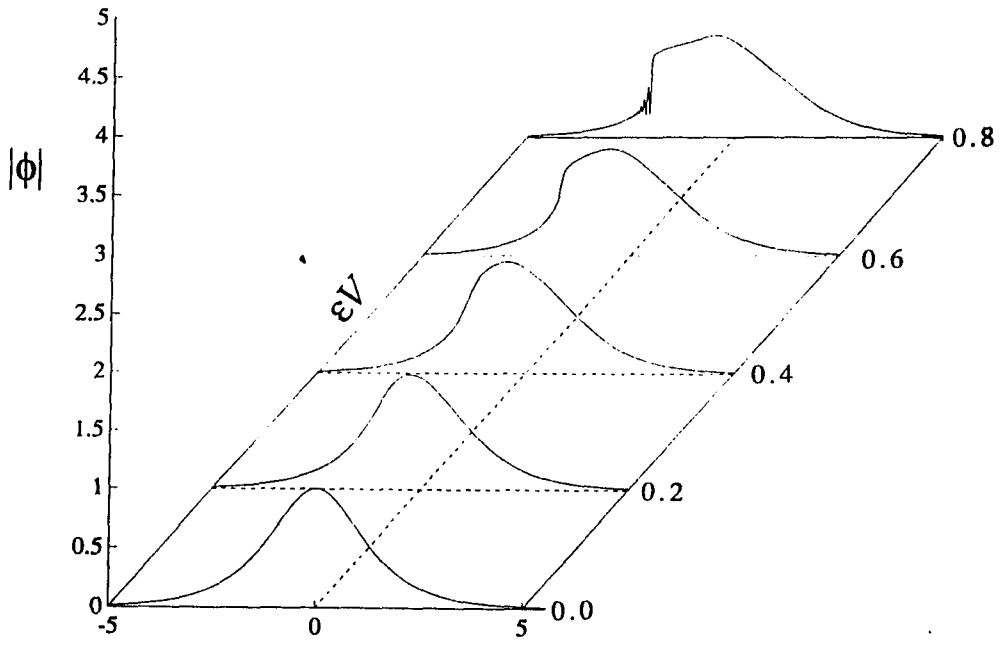

Fig. 2.3b

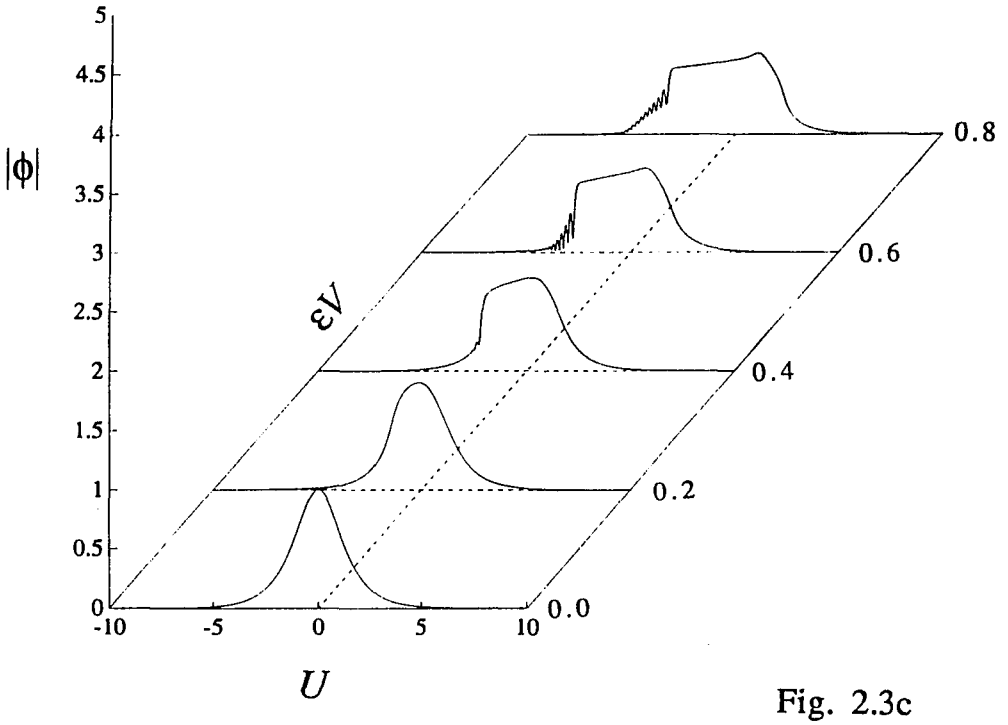

Fig. 2.3c

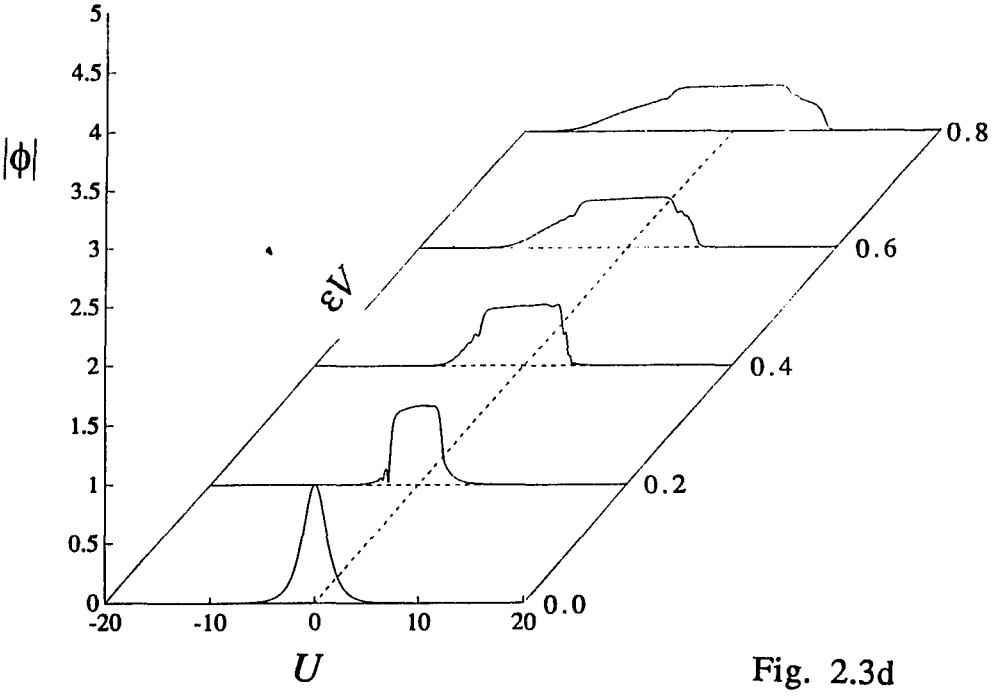

Fig. 2.3d

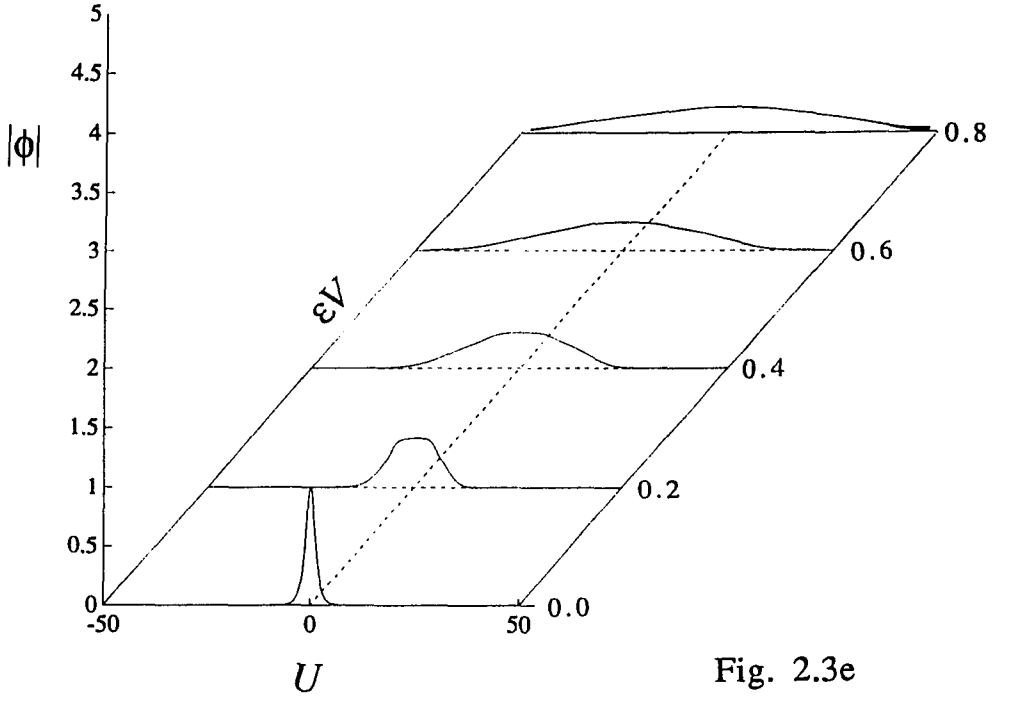

Fig. 2.3e

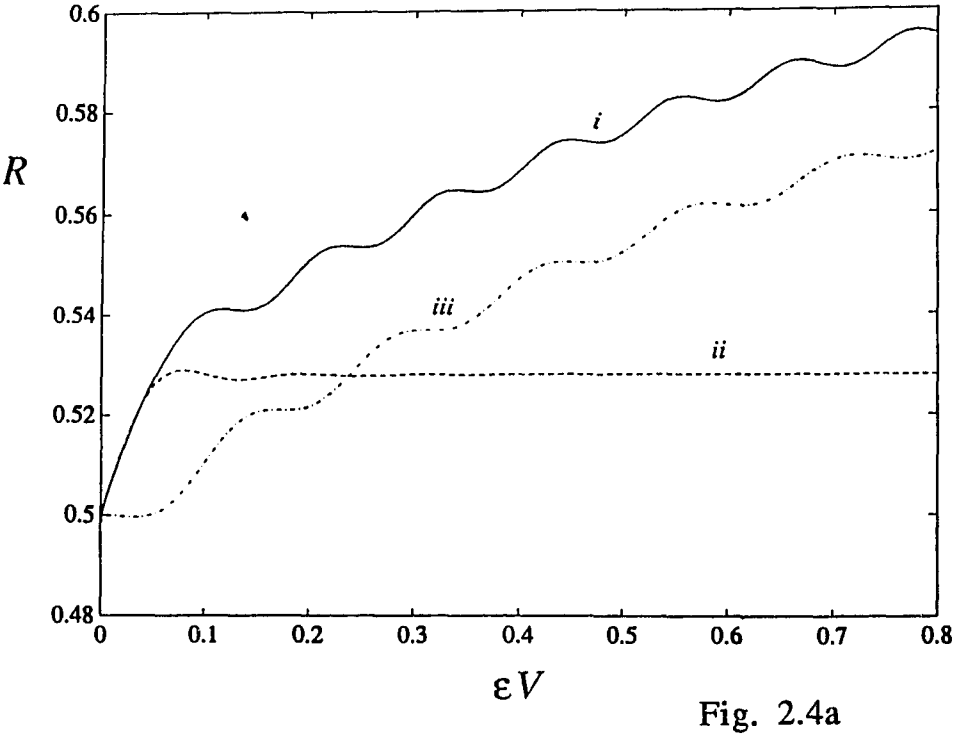

Fig. 2.4a

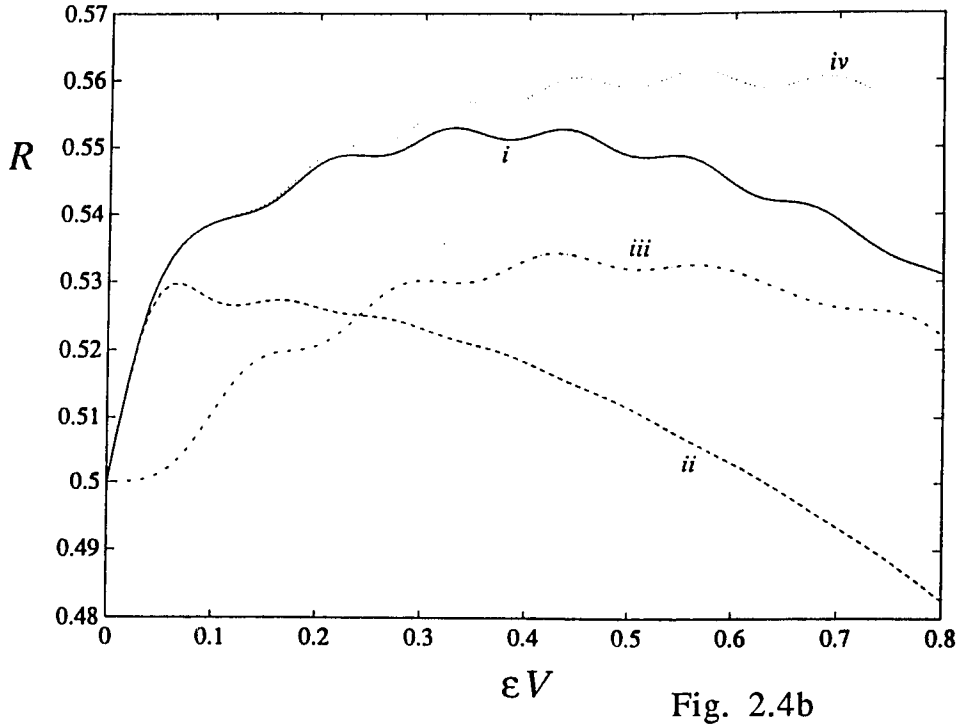

Fig. 2.4b

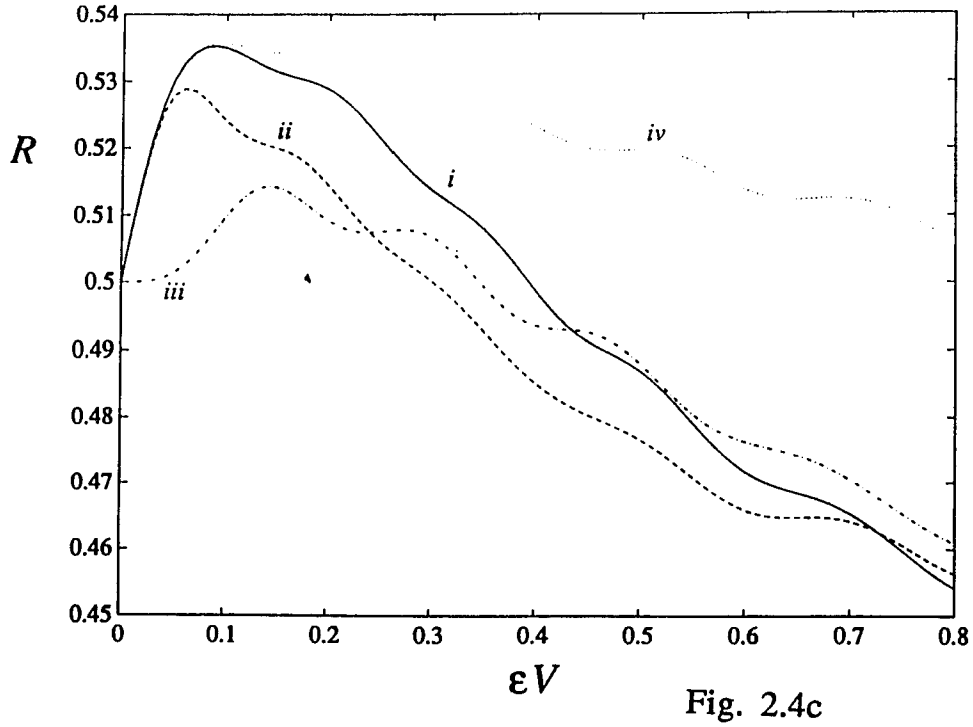

Fig. 2.4c

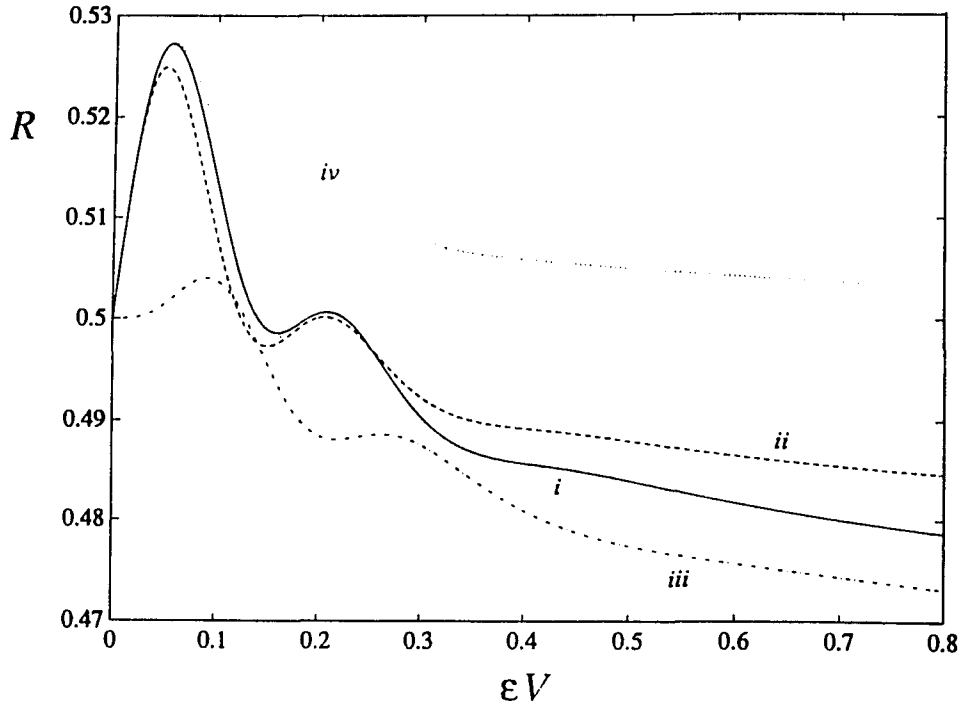

Fig. 2.4d

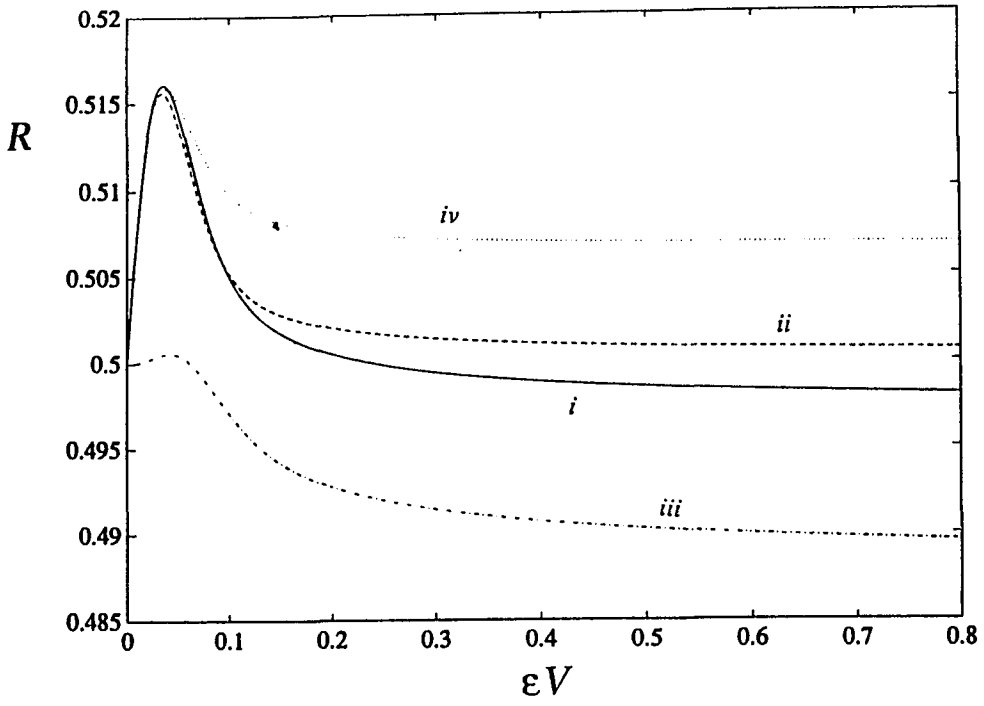

Fig. 2.4e

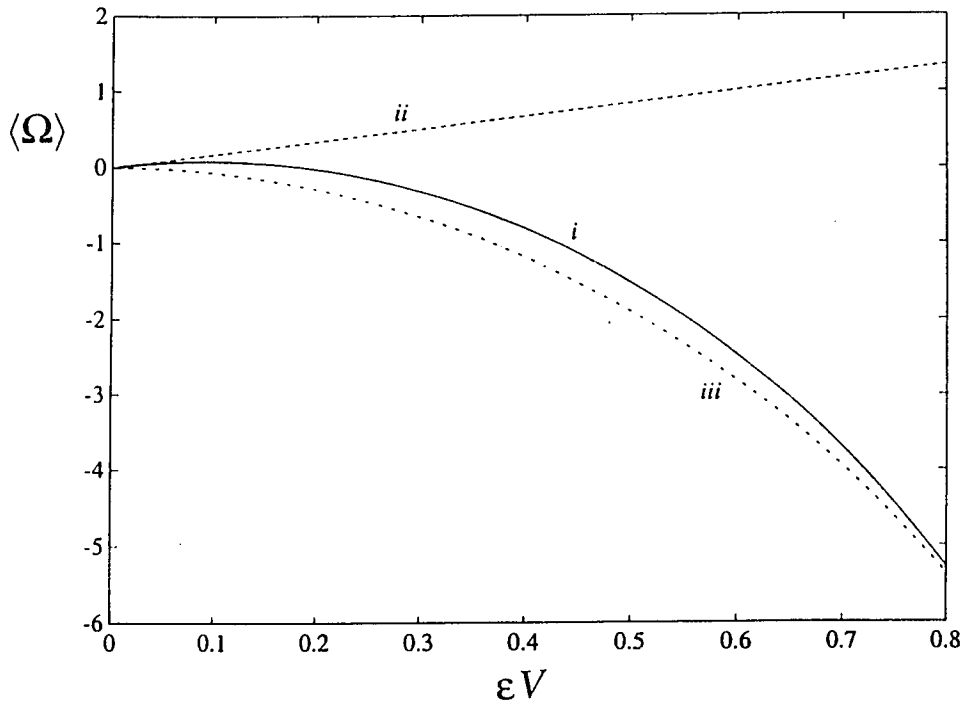

Fig. 2.5a

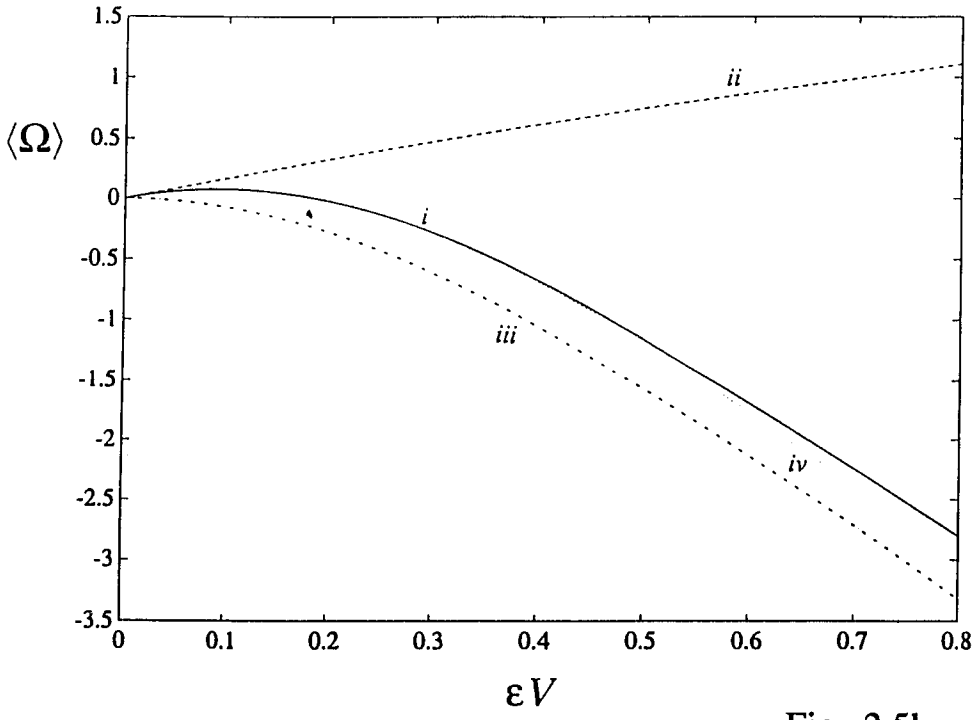

Fig. 2.5b

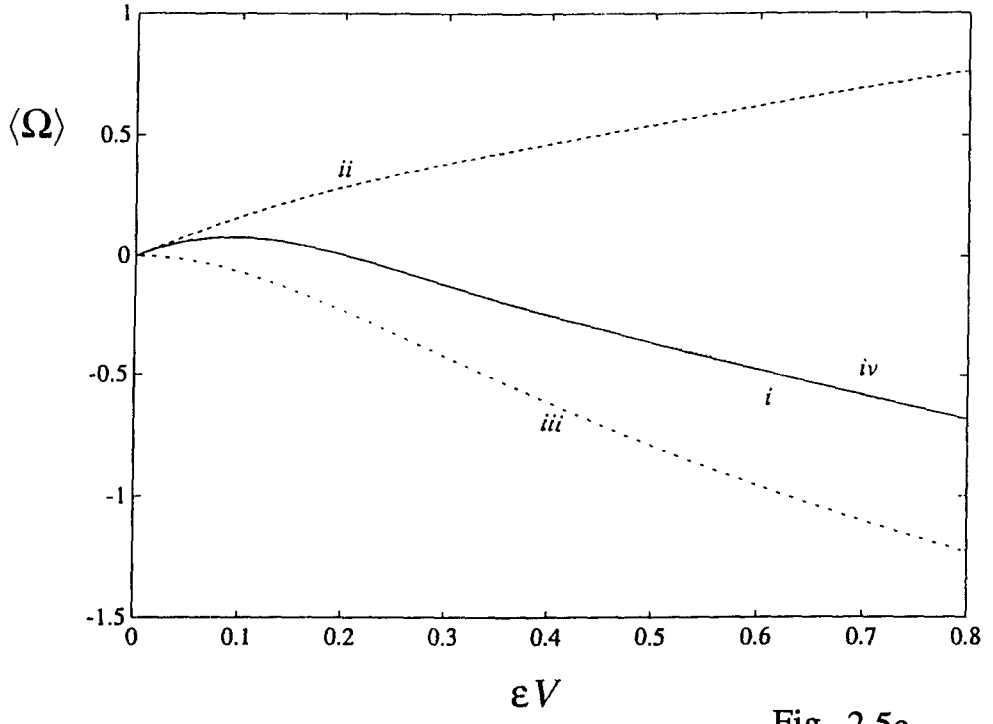

Fig. 2.5c

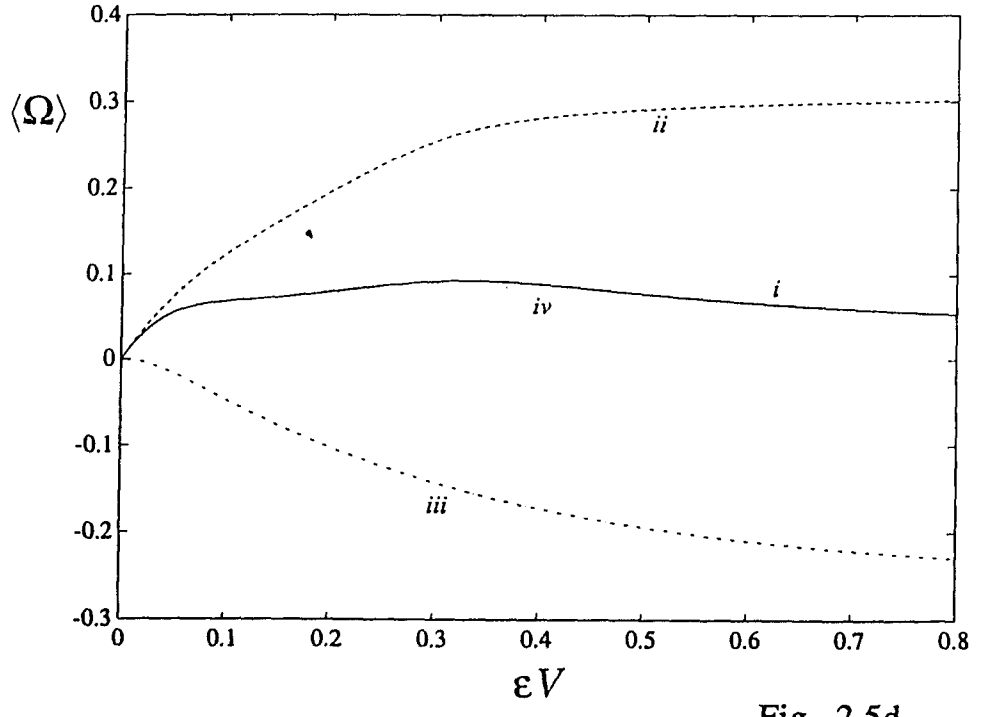

Fig. 2.5d

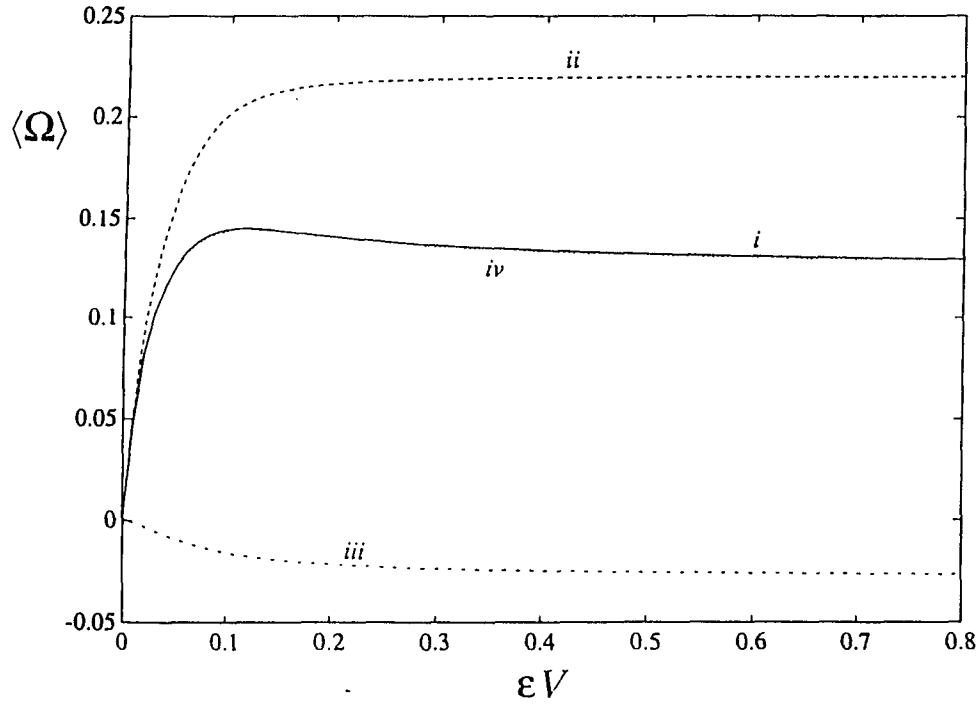

Fig. 2.5e

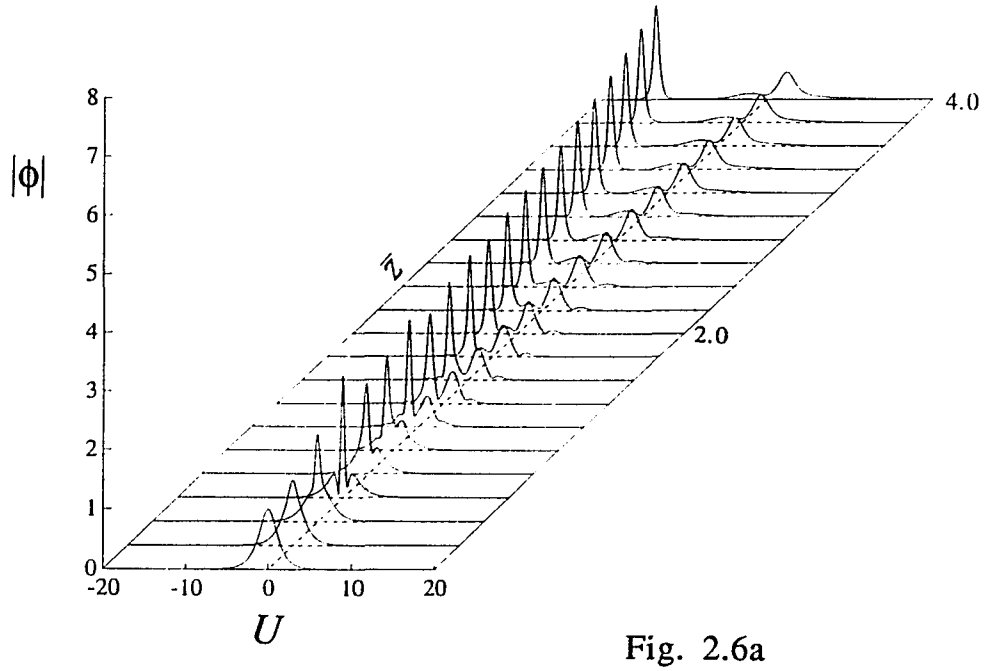

Fig. 2.6a

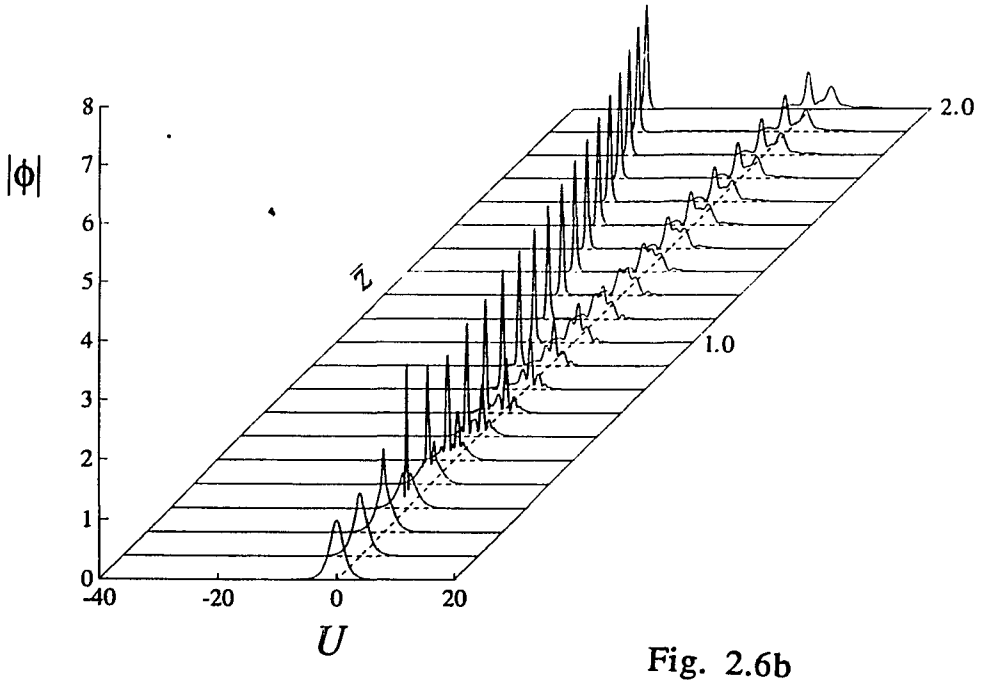

Fig. 2.6b

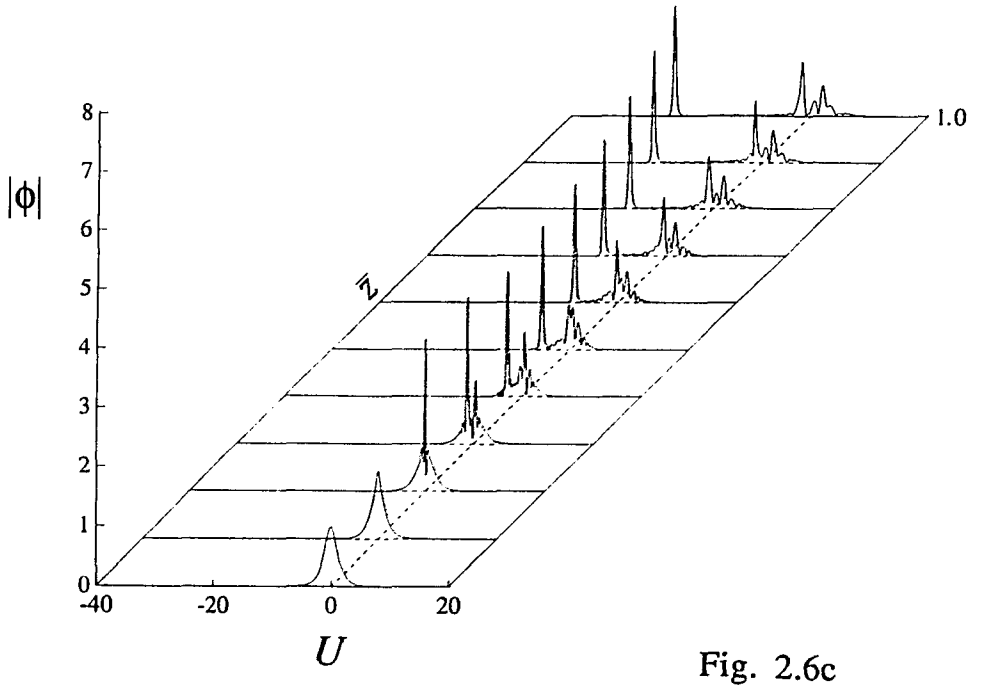

Fig. 2.6c

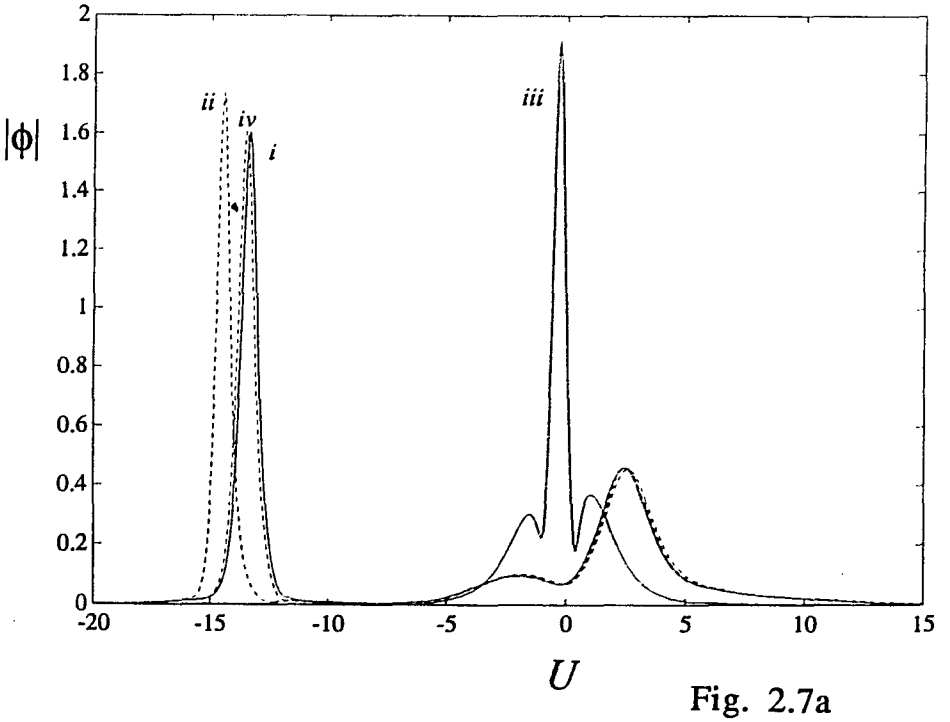

Fig. 2.7a

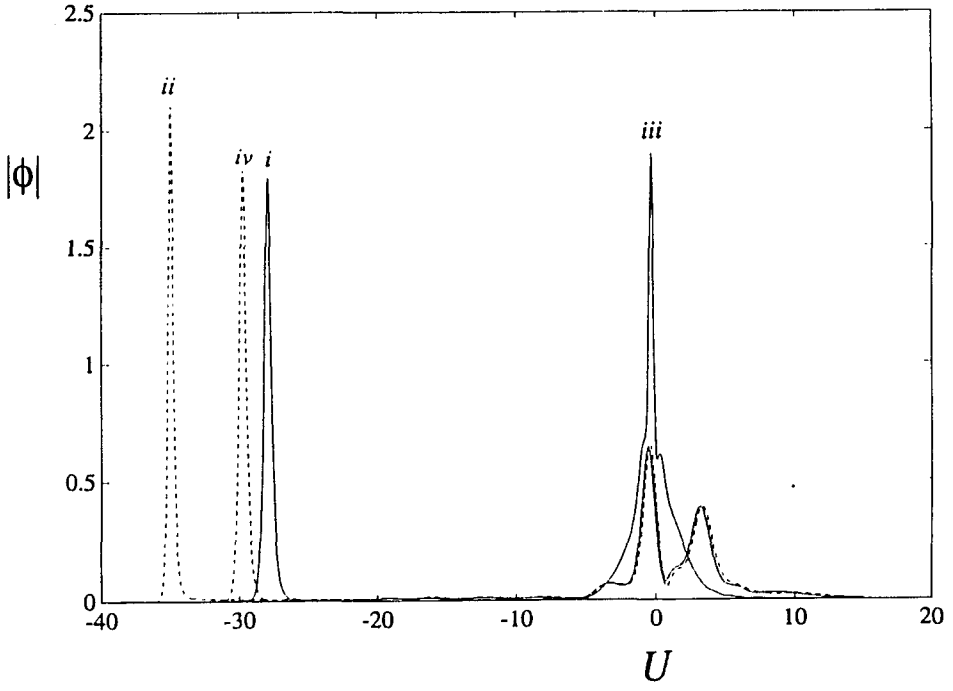

Fig. 2.7b

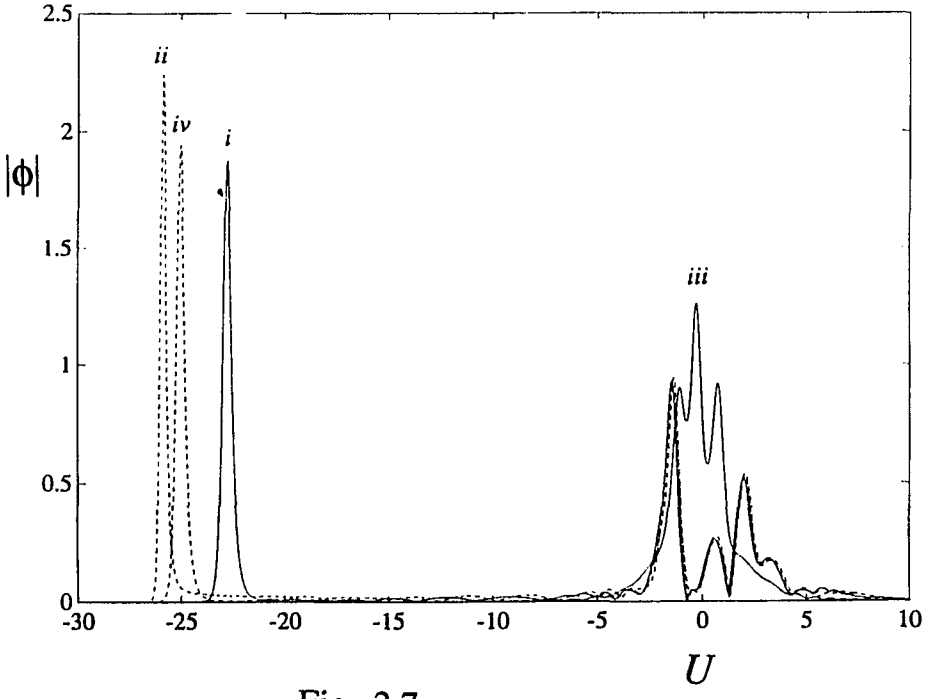

Fig. 2.7c

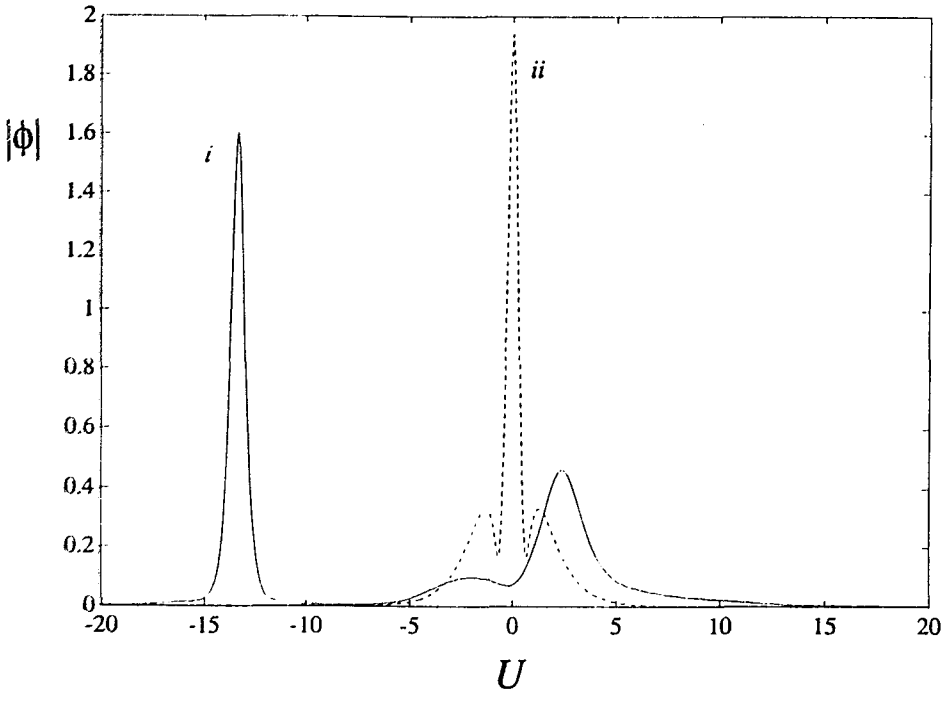

Fig. 2.8a

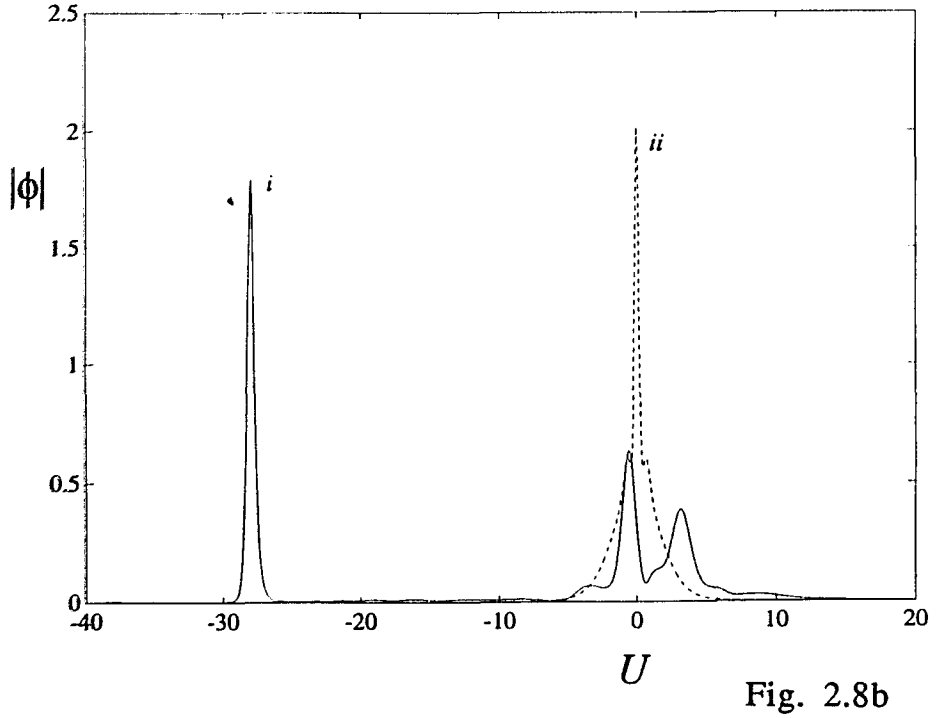

Fig. 2.8b

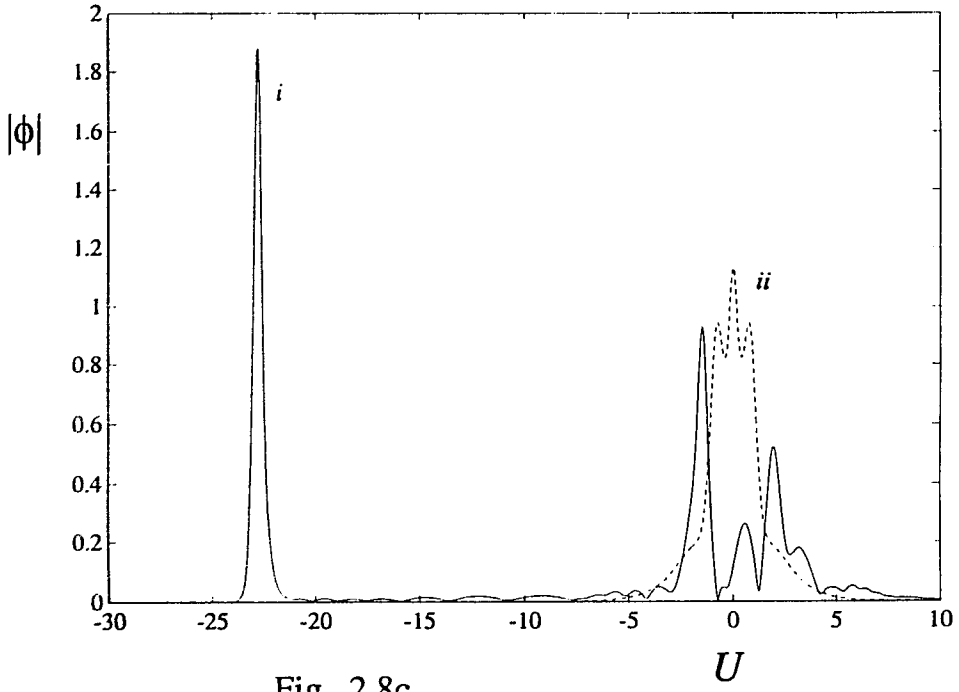

Fig. 2.8c

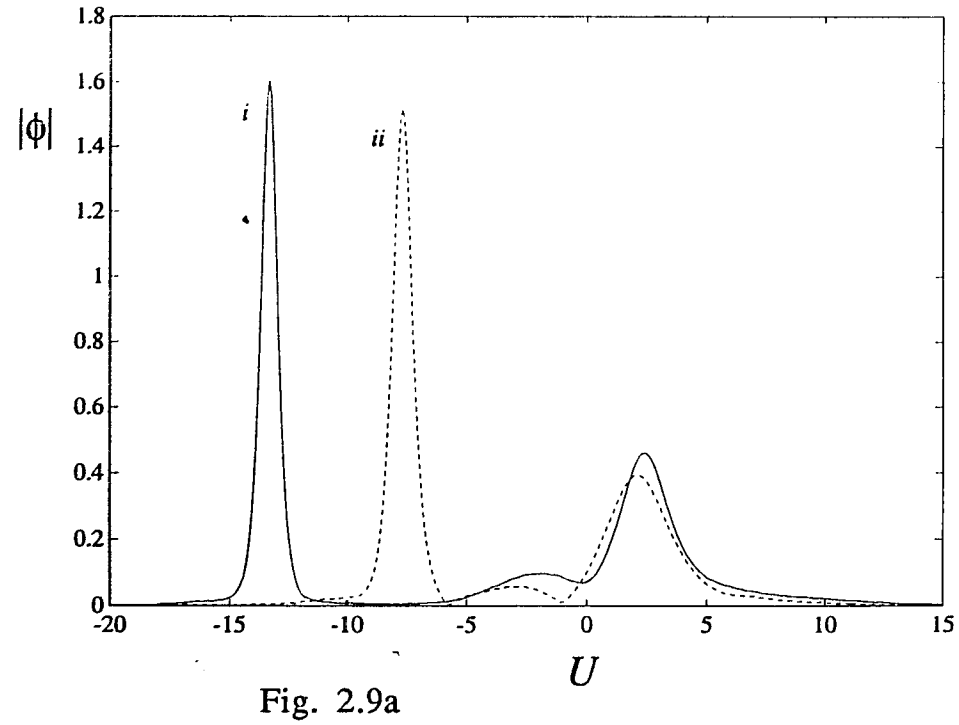

Fig. 2.9a

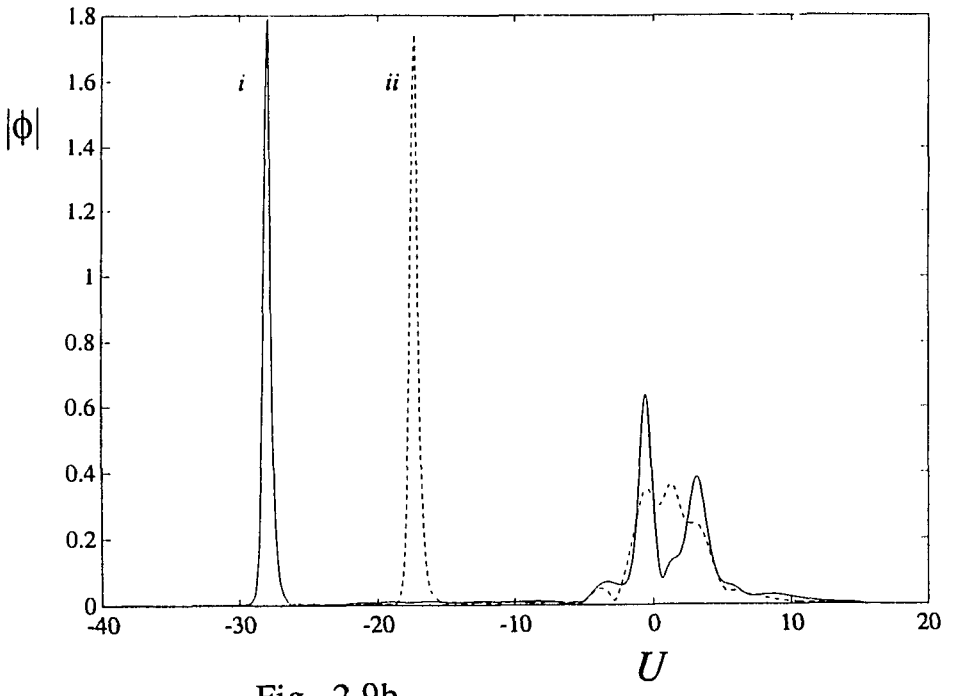

Fig. 2.9b

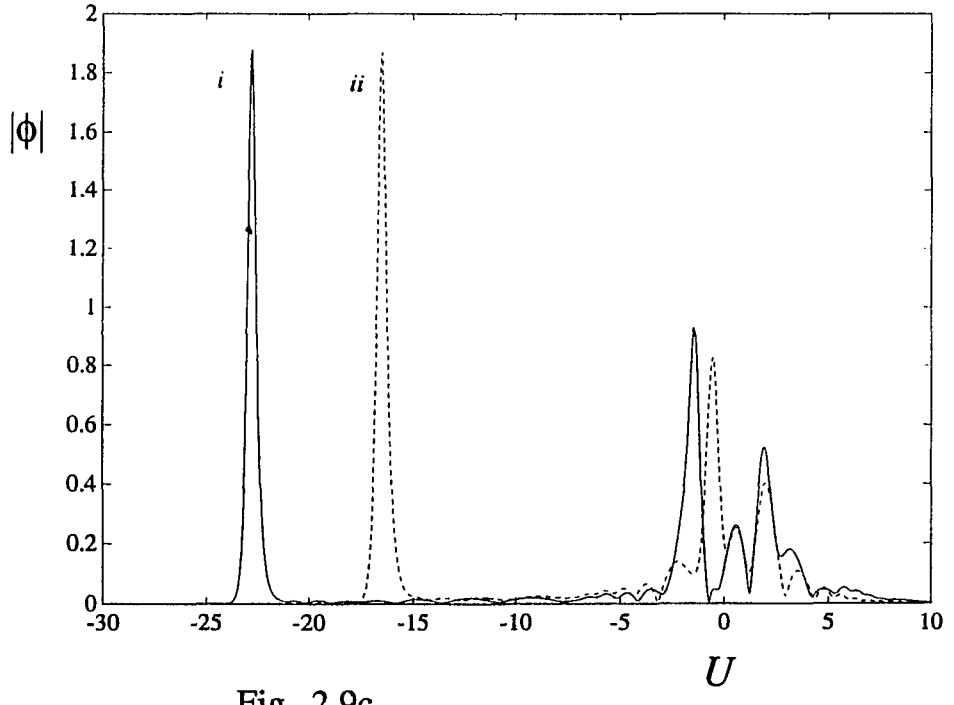

Fig. 2.9c

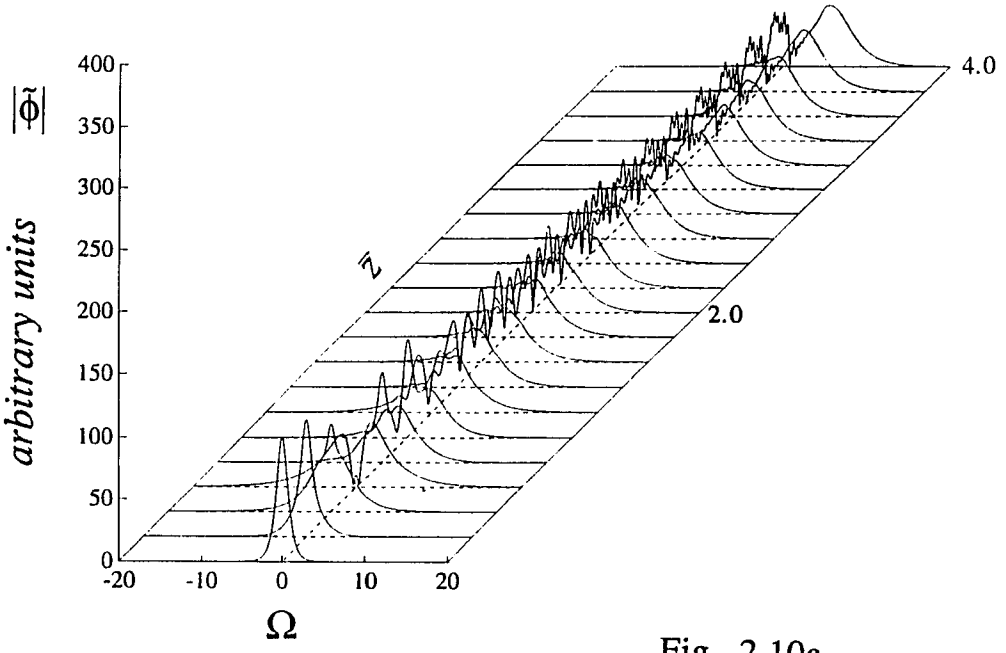

Fig. 2.10a

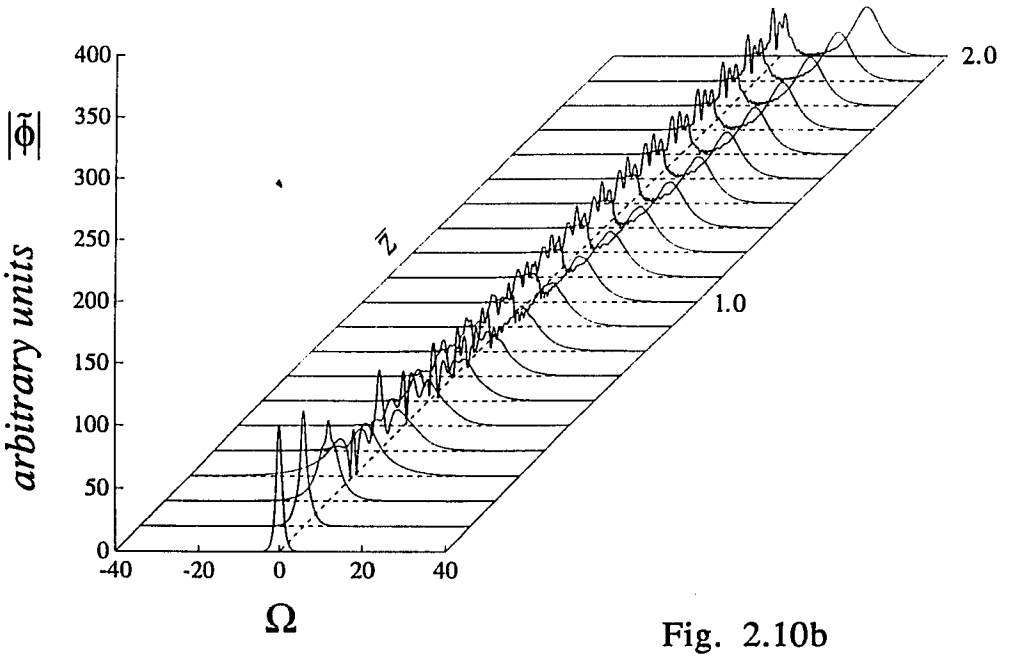

Fig. 2.10b

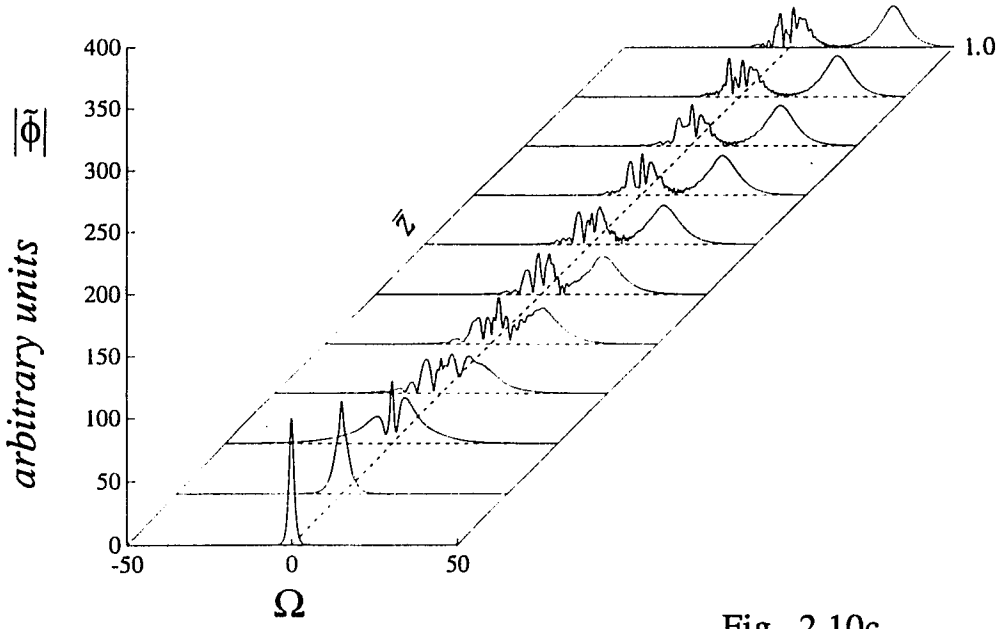

Fig. 2.10c

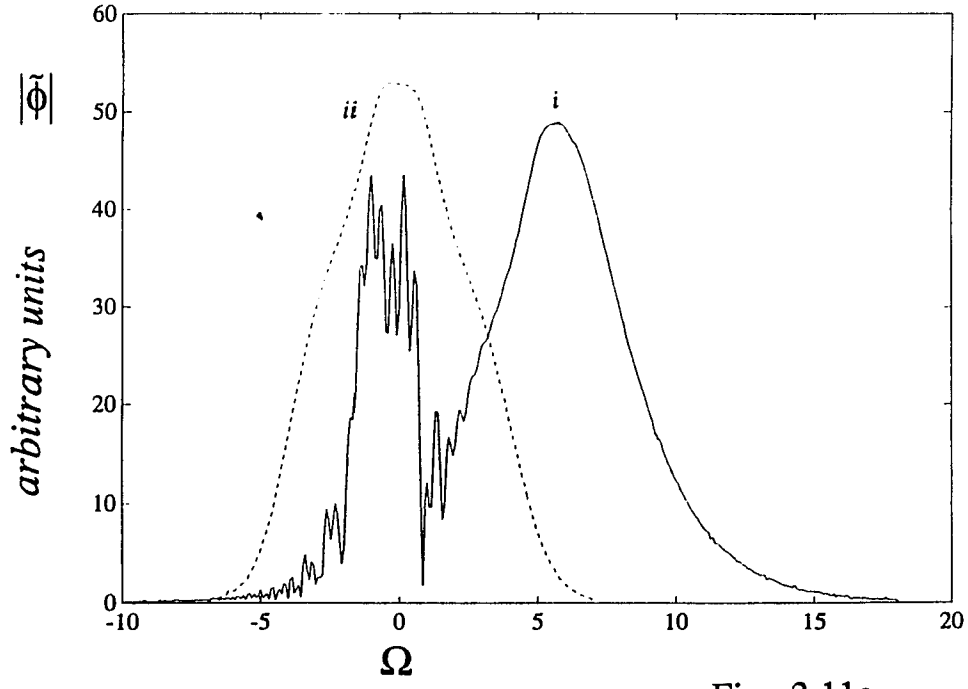

Fig. 2.11a

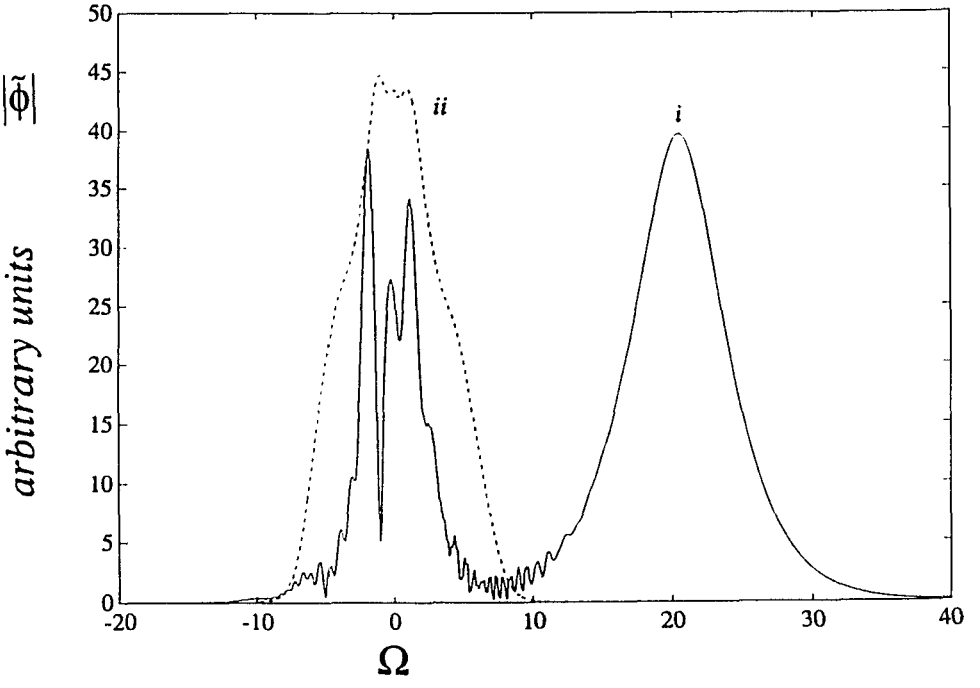

Fig. 2.11b

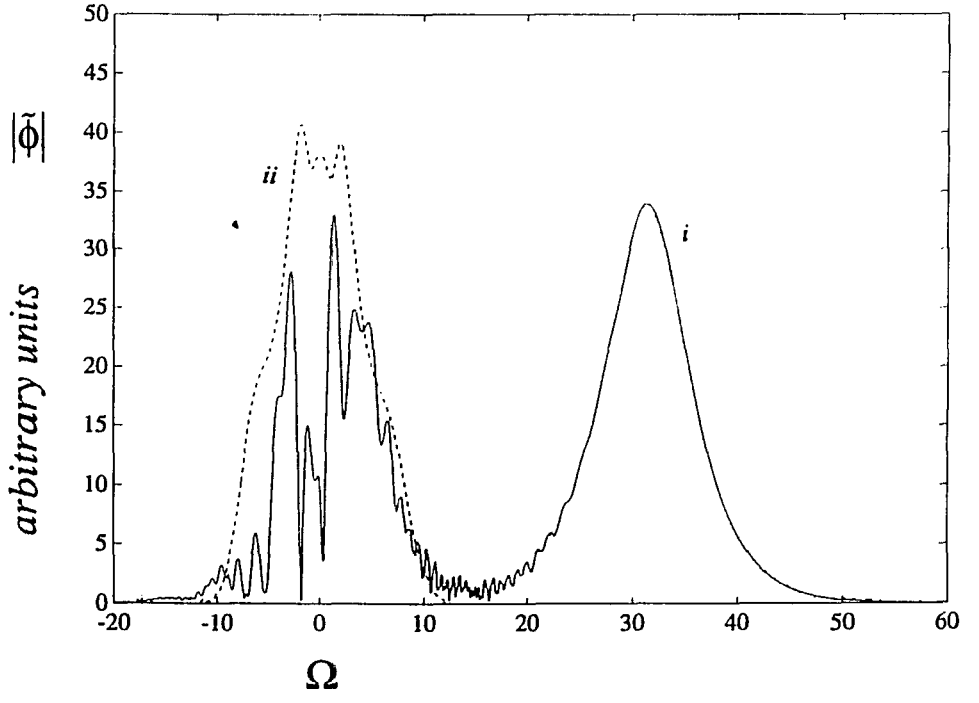

Fig. 2.11c

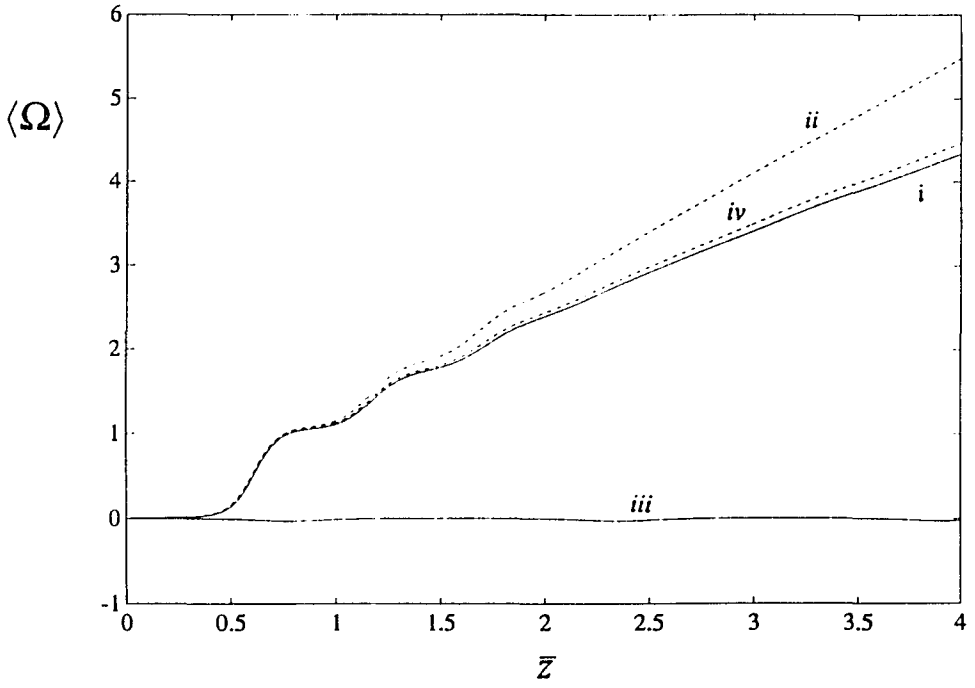

Fig. 2.12a

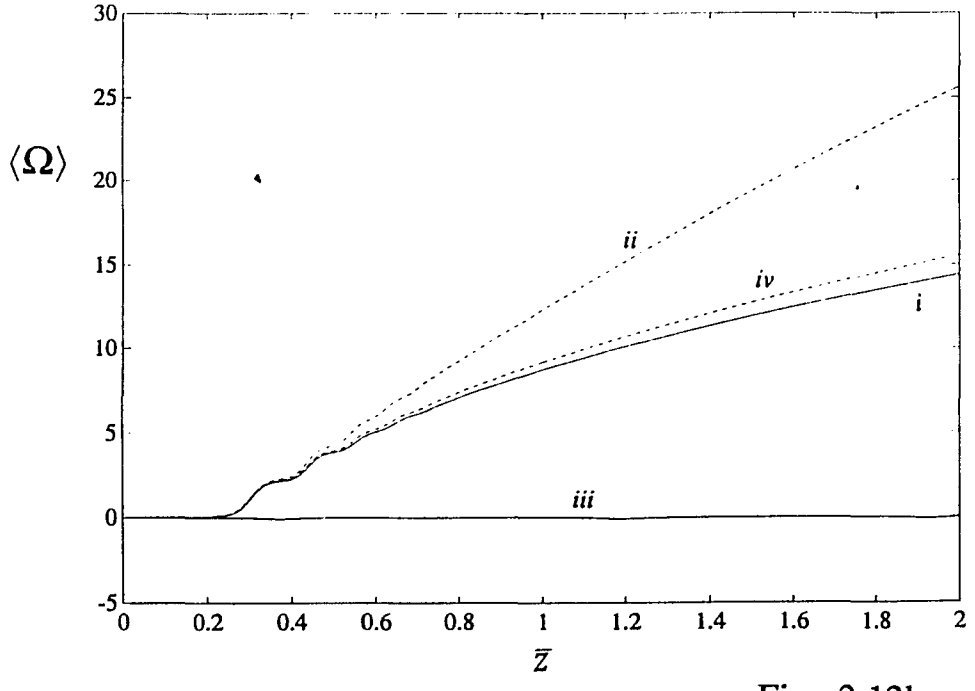

Fig. 2.12b

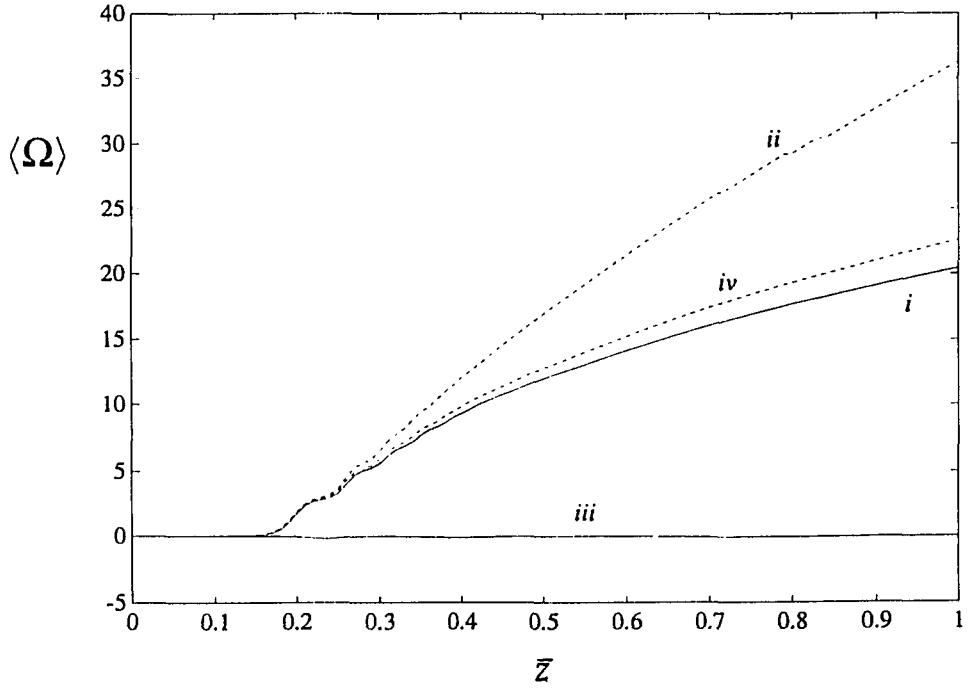

Fig. 2.12c

3.1) Nonlinear Self-Focusing (Axial Symmetry) [g]

The effect of the intensity dependence of the refractive index in the formation of supercontinuum generation has been investigated in Chapter 2. The effects of the intensity dependence on spatial beams constitute another interesting aspect in nonlinear optics. Experiments [35] and theoretical work using aberrationless approximations [36-37] form our basic qualitative understanding of the self-focusing effect for axially symmetric beams. For focusing medium ($n_2 > 0$), there exists a threshold power where the diffractive effects are overcome by the Kerr term. Above this threshold power, the beam undergoes a catastrophic collapse.

The theoretical analysis [37] relies on the use of a paraxial ray approximation which assumes the beam radius is small compared to the relevant nonlinear optic effective radius. This approximation has found wide application in subsequent work [38,39]. More recent analysis of the Nonlinear Shrodinger Equation (N.L.S) using a variational approach [40-42] has led to quantitatively different results from the paraxial approximation. For example, the variational method predicts a self-focusing power four times the paraxial prediction. Numerical models [37] show that the variational prediction is more accurate. On the other hand, the variational method incorrectly predicts self-phase modulation result in the plane wave limit (infinite radius) while the paraxial method gives the proper S.P.M. result. This is explained by the variational techniques use of averaging over the beam radius, a procedure undefined in the plane wave limit [41]. The value of these approximation methods in studying self-focusing, induced self-focusing and super-spiking and

induced super-spike [43,44] phenomenon therefore demands a better understanding of the domains of applicability of these approximations.

Our model of self-focusing in material medium is valid only up to the appearance of the self-focus. Past this point, the beam becomes singular due to the paraxiality of the wave equation. However, if the beam is intense enough, saturation [45] and absorption [46] of the nonlinear index exist. This eliminates the singularity of the field as will be seen later. In another approach, Feit and Fleck [47], using a non-paraxial model propagates the beam past the self-focus. This is done by cutting of all plane waves whose angle > 90 degrees. This makes the model energy non-conservative and thus limits the usefulness of the method. It is to be expected that both approaches give qualitatively similar behavior as both give rise to absorption effects. Therefore, to make sense of our predictions, we propagate up to the focus which in our model is marked by an impulsive change in the beam energy as the spectral grid cannot support the wide angle modes. Further propagation in the Kerr model is meaningless.

If we write the field envelope $E = E_0 \psi$, where E_0 is the field amplitude at $z = 0$ and $r = 0$, the partial differential equation for ψ is then:

$$\frac{1}{\bar{r}} \frac{\partial}{\partial \bar{r}} \left(\bar{r} \frac{\partial \psi}{\partial \bar{r}} \right) - 2i \frac{\partial \psi}{\partial \bar{z}} + p |\psi|^2 \psi = 0 \qquad (3\text{-}1.1)$$

where the radial distance is normalized to the beam radius, $\bar{r} = r / a_0$, the longitudinal distance is normalized to the Rayleigh's length, $\bar{z} = z / k a_0^2$, the nonlinear coupling coefficient,

$$p = \frac{2 n_2 E_0^2 k^2 a_0^2}{n_0} \tag{3-1.2}$$

a_0 is the initial beam size, n_2 is the Kerr coefficient, k is the wave-number, and n_0 is the medium linear index of refraction. In the paraxial approximation scheme, ψ is assumed aberrationless, i.e. does not change shape, and is parametrized as

$$\psi(\bar{r}, \bar{z}) = \frac{1}{\varpi(\bar{z})} \exp\left\{ -\frac{1}{2} \frac{\bar{r}^2}{\varpi^2(\bar{z})} + i \frac{\rho(\bar{z})\, r^2}{2} + i \phi(\bar{z}) \right\} \tag{3-1.3}$$

where $\varpi(\bar{z})$ is the beam normalized size, $\rho(\bar{z})$ is the beam normalized inverse radius of curvature, and $\phi(\bar{z})$ is the longitudinal phase.

Applying the ansatz to the Maxwell equation and using the paraxial approximation to reduce the nonlinear Kerr term by approximating

$$\exp\left(-\frac{\bar{r}^2}{\varpi^2(\bar{z})}\right) \approx \left(1 - \frac{\bar{r}^2}{\varpi^2(\bar{z})}\right) \tag{3-1.4}$$

results in the following equations for the beam parameters

$$\frac{d^2\varpi}{d\bar{z}^2} = \frac{1-p}{\varpi^3} \tag{3-1.5a}$$

$$\rho(\bar{z}) = -\frac{\varpi'(\bar{z})}{\varpi(\bar{z})} \tag{3-1.5b}$$

$$\frac{d\phi}{d\bar{z}} = \frac{(1-p/2)}{\varpi(\bar{z})^2} \tag{3-1.5c}$$

These differential equations may be easily integrated yielding [38]:

$$\varpi(\bar{z}) = \left[1+(1-p)\bar{z}^2\right]^{1/2} \tag{3-1.6a}$$

$$\rho(\bar{z}) = -\frac{\bar{z}(1-p)}{\left[1+(1-p)\bar{z}^2\right]} \tag{3-1.6b}$$

$$\phi(\bar{z}) = \left(1-\frac{p}{2}\right)\left[\frac{1}{\sqrt{1-p}}\arctan\left(\bar{z}\sqrt{1-p}\right)\right] \qquad \text{for } 0<p<1$$

$$= \left(1-\frac{p}{2}\right)\left[\frac{1}{2\sqrt{p-1}}\ln\left(\frac{1+\bar{z}\sqrt{p-1}}{1-\bar{z}\sqrt{p-1}}\right)\right] \qquad \text{for } p>1 \tag{3-1.6c}$$

From this we see that the regularized phase (longitudinal phase - diffractive phase) is given by

$$\phi(\bar{z}) = -p\bar{z}/2 \tag{3-1.7}$$

which agrees with the S.P.M. result and the beam radius will collapse at

$$\bar{z}_f = \sqrt{p-1} \tag{3-1.8}$$

for a power p>1. Thus p=1 defines the wave guiding power in the paraxial approximation scheme.

In the variational formulation of the problem, a Lagrangian functional is found in which the first variation set to zero returns the N.L.S equation. Then by optimizing (taking the variation of) the integrated lagrangian with respect to the beam parameters give the equations of motion. The ansatz is again

$$\psi(\bar{r},\bar{z}) = \frac{1}{\varpi(\bar{z})}\exp\left\{-\frac{1}{2}\frac{\bar{r}^2}{\varpi^2(\bar{z})} + i\frac{\rho(\bar{z})\,r^2}{2} + i\,\phi(\bar{z})\right\} \tag{3-1.9}$$

and the required Lagrangian Functional is

$$\mathrm{L} = \bar{r}\left|\frac{\partial\psi}{\partial\bar{r}}\right| - i\bar{r}\left(\psi\frac{\partial\psi^*}{\partial\bar{z}} - \psi^*\frac{\partial\psi}{\partial\bar{z}}\right) - \frac{p}{4}\bar{r}|\psi|^4 \tag{3-1.10}$$

and the equations of motion are

$$\frac{\delta \mathbf{L}}{\delta\omega} = \frac{\delta \mathbf{L}}{\delta\rho} = \frac{\delta \mathbf{L}}{\delta\phi} = 0 \tag{3-1.11}$$

where $$\frac{\delta \mathbf{L}}{\delta\omega} = \frac{\partial}{\partial\bar{z}}\left(\frac{\partial \mathbf{L}}{\partial\left(\frac{\partial\omega}{\partial\bar{z}}\right)}\right) - \frac{\partial \mathbf{L}}{\partial\omega}\ \text{etc.} \tag{3-1.12}$$

and the integrated (over the cross-section) lagrangian is defined as

$$\mathbf{L} = \int \mathrm{L} ds = \int \mathrm{L} \bar{r} d\bar{r} \tag{3-1.13}$$

Going through tedious but straightforward algebra gives the following equations for the beam parameters:

$$\frac{d^2 \varpi}{d\bar{z}^2} = \frac{1 - \frac{p}{4}}{\varpi^3} \tag{3-1.14a}$$

$$\rho(\bar{z}) = -\frac{\varpi'(\bar{z})}{\varpi(\bar{z})} \tag{3-1.14b}$$

$$\frac{d\phi}{d\bar{z}} = \frac{(1 - \frac{3p}{8})}{\varpi(\bar{z})^2} \tag{3-1.14c}$$

These equations are integrated to give [41]:

$$\varpi(\bar{z}) = \left[1 + (1 - \tilde{p})\bar{z}^2\right]^{1/2} \tag{3-1.15a}$$

$$\rho(\bar{z}) = -\frac{\bar{z}(1 - \tilde{p})}{\left[1 + (1 - \tilde{p})\bar{z}^2\right]} \tag{3-1.15b}$$

$$\phi(\bar{z}) = \left(1 - \frac{3\tilde{p}}{2}\right)\left[\frac{1}{\sqrt{1 - \tilde{p}}} \arctan\left(\bar{z}\sqrt{1 - \tilde{p}}\right)\right] \qquad \text{for } 0 < \tilde{p} < 1$$

$$= \left(1 - \frac{3\tilde{p}}{2}\right)\left[\frac{1}{2\sqrt{\tilde{p} - 1}} \ln\left(\frac{1 + \bar{z}\sqrt{\tilde{p} - 1}}{1 - \bar{z}\sqrt{\tilde{p} - 1}}\right)\right] \qquad \text{for } \tilde{p} > 1 \tag{3-1.15c}$$

where $\tilde{p} = p / 4$.

From this, we see that the critical power for self-focusing in the variational method is four times larger than the value obtained by the paraxial approximation method. Also, we see that the regularized phase (longitudinal phase - diffractive phase) is given by

$$\phi(\bar{z}) = -3p\bar{z} / 8 \qquad (3\text{-}1.16)$$

which differs from the S.P.M result by 25%.

Numerical Results

An analytic solution to N.L.S equation for the axially symmetric beam for arbitrary initial field distribution is not yet known. By numerically integrating the equation over a wide range of input powers, the true evolution of the amplitude and phase are determined. The numerical algorithm used combines 2-D Fast Fourier Transform and Runge-Kutta scheme. The use of Cartesian coordinates fails to utilize the cylindrical symmetry of the beam. However, the flexibility of this formulation allows the study of non cylindrical beams which will be undertaken later. The accuracy of this method was tested by :

1) Monitoring the pulse energy.

2) Reproducing the free diffraction (p=0) result

3) Reproducing the Self-Phase Modulation solution.

4) The spatial soliton solution was recovered in the limit of a 2D beam with sech profile.

In fig. 3-1, the on-axis field as a function of propagation distance is compared to the semi-analytic methods. In fig. 3-2, the regularized

phase is plotted as a function of propagation distance and compared to the semi-analytic methods. The results may be encapsulated as follows:

1) For powers less than the variational self-focusing power, the variational method gives excellent quantitative agreement for the beam parameters .

2) For small distances of propagation, the variational method fails to give quantitative agreement to the on axis beam amplitude and phase. In this regime, the paraxial method gives the correct asymptotic evolution. This is due to the paraxial method giving the correct S.P.M result in the plane wave limit.

3) As the power increases beyond the variational self-focusing power, the variational method breaks down and the paraxial method gives better quantitative agreement. This is due to the short self-focusing distances at these powers and as we have already shown, the paraxial method is better in the short distance regime.

4) In the paraxial approximation, there exists a power domain $0<p<2$ in which the regularized phase changes sign as the beam propagates. In the variational method, the regularized phase is monotonic for any power. If the paraxial prediction is correct, this leads to the possibility of the blue components leading the red in the supercontinuum. This would allow for pulse compression without phase adjusting external gratings [38]. The numerical results show unambiguously that the regularized phase never changes sign confirming the qualitative results obtained in [41].

In fig. 3-3, we plot the beam profile and the total phase minus the longitudinal (on-axis) phase as a function of the normalized

the profile is a Gaussian and the phase difference is a parabola. The true beam parameters differ significantly from either prediction. The dip in the phase difference indicates that the field radius of curvature is not constant along the beam wavefront. This change is possibly measurable by observing its effect on a weak probe beam copropagating with this beam as pump.

3.2) Self-focusing (Elliptic Gaussian Beams) [j]

The characteristic features of an intense c.w. beam propagating in Kerr medium are qualitatively different depending on the spatial dimension. In a 2D space (one longitudinal + one transverse dimensions) and for a well defined beam shape and relation between the beam amplitude and width spatial solitons are possible [48,49]. On the other hand, in a 3D space (one longitudinal + two transverse dimensions) a beam with an intensity larger than a critical value self-focuses [35,36]. The transition from one limit to the other can be studied through the analysis of the propagation of a 3D elliptical beam for different values of the ellipticity. The propagation of a c.w. Gaussian elliptical beam in a nonlinear Kerr material has been considered [50-53] in the aberrationless paraxial approximation. Here, the variational method is extended to the axially nonsymmetric case and the results of both semi-analytic techniques are compared to numerical results using an algorithm that combines the Fast Fourier 2D transform and Runge-Kutta techniques . This numerical algorithm is identical to that of the axial symmetric case and accuracy was ensured by monitoring the energy of the beam. The exact numerical results are shown to differ significantly from either approximations. Furthermore, we show that in the exact treatment we observe qualitative features that are absent in any aberrationless approximation scheme. In particular, we find that for a sufficiently large ellipticity and intensity a hole (beam splitting) in the beam intensity can develop in the center of the beam. This hole manifests

itself through modulation of the spatial Fourier transform of the field.

If we write the field envelope $E = E_0\,\psi$, where E_0 is the field amplitude at $z = 0$ and $(x, y) = (0,0)$, the partial differential equation for ψ is then:

$$\frac{\partial^2 \psi}{\partial \bar{x}^2} + \frac{\partial^2 \psi}{\partial \bar{y}^2} - 2i\frac{\partial \psi}{\partial \bar{z}} + p|\psi|^2 \psi = 0 \qquad (3\text{-}2.1)$$

where the transverse components are normalized to the elliptic beam short dimension, i.e. $(\bar{x}, \bar{y}) = (x / a_0, y / a_0)$, the longitudinal distance is normalized to the short axis Rayleigh's length, $\bar{z} = z / k a_0^2$, the nonlinear coupling coefficient,

$$p = \frac{2 n_2 E_0^2 k^2 a_0^2}{n_0} \qquad (3\text{-}2.2)$$

a_0 is the initial elliptic beam short dimension, n_2 is the Kerr coefficient, k is the wave-number, and n_0 is the medium linear index of refraction. We have normalized the equation so that fixed p means fixed initial beam intensity. In either aberrationless approximation scheme, an initially elliptic Gaussian beam may be parametrized for any z as:

$$\psi(\bar{x}, \bar{y}, \bar{z}) = A(\bar{z}) \exp\left\{ -\frac{1}{2}\frac{\bar{x}^2}{\varpi_x^2(\bar{z})} - \frac{1}{2}\frac{\bar{y}^2}{\varpi_y^2(\bar{z})} + i\frac{\rho_x(\bar{z})\,\bar{x}^2}{2} + i\frac{\rho_y(\bar{z})\,\bar{y}^2}{2} \right\} \qquad (3\text{-}2.3)$$

where $|A(\bar{z})|$ is the on-axis amplitude, $(\varpi_x(\bar{z}), \varpi_y(\bar{z}))$ are the beam normalized sizes respectively in the x and y directions, $(\rho_x(\bar{z}), \rho_y(\bar{z}))$

are the beam normalized inverse radius of curvature respectively in the x and y directions, and $\arg[A(\bar{z})]$ is the longitudinal phase. In the paraxial approximation scheme, the ansatz is plugged directly into the field envelope equation. Using the paraxial approximation explained earlier, the following coupled differential equations are obtained [50-53].

$$\frac{\partial^2 \varpi_x}{\partial \bar{z}^2} - \frac{1}{\varpi_x^3} + \frac{p\varepsilon}{\varpi_x^2 \varpi_y} = 0 \tag{3-2.4a}$$

$$\frac{\partial^2 \varpi_y}{\partial \bar{z}^2} - \frac{1}{\varpi_y^3} + \frac{p\varepsilon}{\varpi_y^2 \varpi_x} = 0 \tag{3-2.4b}$$

$$A(\bar{z}) = \left(\frac{\varepsilon}{\varpi_x(\bar{z})\varpi_y(\bar{z})} \right)^{1/2} \tag{3-2.4c}$$

$$\rho_{x,y} = -\left(\frac{\left(\frac{d\varpi_{x,y}}{d\bar{z}} \right)}{\varpi_{x,y}} \right) \tag{3-2.4d}$$

$$\frac{d[\arg(A)]}{d\bar{z}} = +\left[\frac{1}{2}\left(\frac{1}{\varpi_x^2} + \frac{1}{\varpi_y^2} \right) - \frac{p\varepsilon}{2\varpi_x \varpi_y} \right] \tag{3-2.4e}$$

The initial conditions for the beam parameters are:
$A(\bar{z}=0)=1, \varpi_x(\bar{z}=0)=1, \varpi_y(\bar{z}=0)=\varepsilon, \rho_x(\bar{z}=0)=0, \rho_y(\bar{z}=0)=0.$
These equations can be solved numerically using standard Runge-Kutta techniques.

In analogy with the variational formulation in the cylindrically symmetric case, we formulate the equations of motion for the beam parameters which are derived from the Euler-Lagrange equations of the Lagrangian density:

$$\mathrm{L} = -\frac{i}{2}\left[\psi\frac{\partial\psi^*}{\partial\bar{z}} - \psi^*\frac{\partial\psi}{\partial\bar{z}}\right] + \frac{1}{2}\left[\left|\frac{\partial\psi}{\partial\bar{x}}\right|^2 + \left|\frac{\partial\psi}{\partial\bar{y}}\right|^2\right] - \frac{p}{4}|\psi|^4 \qquad (3\text{-}2.5)$$

and the ordinary differential equations for the different functions appearing in the ansatz are then obtained by a variational optimization over the reduced Lagrangian:

$$\mathbf{L} = \iint d\bar{x}\; d\bar{y}\; \mathrm{L} \qquad (3\text{-}2.6)$$

which give the following coupled equations for the beam parameters:

$$\frac{\partial^2\varpi_x}{\partial\bar{z}^2} - \frac{1}{\varpi_x^3} + \frac{\tilde{p}\varepsilon}{\varpi_x^2\varpi_y} = 0 \qquad (3\text{-}2.7a)$$

$$\frac{\partial^2\varpi_y}{\partial\bar{z}^2} - \frac{1}{\varpi_y^3} + \frac{\tilde{p}\varepsilon}{\varpi_y^2\varpi_x} = 0 \qquad (3\text{-}2.7b)$$

$$A(\bar{z}) = \left(\frac{\varepsilon}{\varpi_x(\bar{z})\varpi_y(\bar{z})}\right)^{1/2} \qquad (3\text{-}2.7c)$$

$$\rho_{x,y} = -\left(\frac{\left(\frac{d\varpi_{x,y}}{d\bar{z}} \right)}{\varpi_{x,y}} \right) \tag{3-2.7d}$$

$$\frac{d[\arg(A)]}{d\bar{z}} = +\left[\frac{1}{2}\left(\frac{1}{\varpi_x^2} + \frac{1}{\varpi_y^2} \right) - \frac{3}{2}\frac{\tilde{p}\varepsilon}{\varpi_x \varpi_y} \right] \tag{3-2.7e}$$

where $\tilde{p} = p/4$.

The coupled equations for the normalized beam radii form an Ermakov system [55]. The form of the coupled equations is such that the system can be derived from a Hamiltonian function given by

$$H = \frac{1}{2}\left[\left(\frac{d\varpi_x}{d\bar{z}} \right)^2 + \left(\frac{d\varpi_y}{d\bar{z}} \right)^2 \right] + \frac{1}{2}\left[\left(\frac{1}{\varpi_x} \right)^2 + \left(\frac{1}{\varpi_y} \right)^2 \right] - \frac{\tilde{p}\varepsilon}{\varpi_x \varpi_y} \tag{3-2.8}$$

which is an integral of the motion. Combining H with the equations of motion, the expression for the sum of the squares of the width can be obtained for any normalized longitudinal distance

$$\varpi_x^2 + \varpi_y^2 = \left[1 + \frac{1}{\varepsilon^2} - 2\tilde{p} \right] \bar{z}^2 + \left(1 + \varepsilon^2 \right) \tag{3-2.9}$$

From this, variational approximation self-focusing is possible for $\tilde{p} > 0.5\left(1 + \varepsilon^{-2}\right)$ and the focusing distance is

$$\bar{z}_f^2 = \frac{\left(1+\varepsilon^2\right)}{\left(2\tilde{p}-1-\varepsilon^{-2}\right)} \qquad (3\text{-}2.10)$$

The results for the elliptic beam reproduce, in the limit of unit ellipticity, the axially symmetric case. Note also that as the ellipticity tends to infinity, the wave guiding intensity corresponds to the 2D spatial soliton.

Numerical Results

The semi-analytic approximations are compared to an exact numerical treatment using the same algorithm as was used in the cylindrical beam. In fig. 3-4, the self-focusing distance is plotted as a function of the ellipticity for various input intensities. We note:

1) For $1<p<4$, the propagation as a function of ellipticity will go from a regime of diffractive propagation (i.e. the diffractive effect overcomes the Kerr effect) to a self-focusing regime. The self-focusing distance reaches a minimum at some ellipticity and increases monotonically towards infinity as the ellipticity goes to infinity. Detailed results for p=2 are representative of this region.

2) For p=4, the propagation is always self-focusing and the self-focusing distance decreases until it reaches some representative ellipticity. Then the self-focusing distance increases monotonically as the ellipticity increases. For small ellipticities, the self-focusing distance lies between the variational and paraxial approximations. For sufficiently high ellipticity, the self-focusing distance is less than either theory although the paraxial predictions are quantitatively superior. This is in analogy to the cylindrical beam in which the paraxial method is better for higher powers. Since the incident power increases if the ellipticity of the beam increases, one may expect better agreement in the paraxial approximation.

3) For sufficiently high ellipticity and beam intensity, a new phenomenon is observed. The beam will undergo pulse splitting in a quasi-periodic manner. This is expected as the beam undergoes the transition towards a higher order spatial soliton state. In fig. 3-5, the pulse splitting is clearly seen as we plot the evolution of the x and y transverse profiles. In this regime, application of an aberrationless approximation method is doomed to failure as is seen by fig. 3-6

where the transverse profiles in the pulse splitting regime are compared to the approximate methods. A more complex ansatz which inherently allows for pulse splitting seems necessary.

4) In fig 3-7, we plot the spatial Fourier transform of the x and y cross-sections. The spatial spectrum is modulated with increasing intensity and ellipticity. This is also explained in the transition to a higher order soliton state.

5) In fig 3-8, the x and y cross-sections are given just before the focus for various intensities and ellipticities. In all cases, the geometry of the beam in the region near the self-focusing point becomes cylindrical except for pedestal effects. In this case, the wide axes collapses to the width of the narrow axis. This result is contrary to the predictions of the approximate methods.

Figures Captions

Fig. 3-1 The field amplitude for $\bar{r}=0$ is plotted as a function of the normalized longitudinal distance of propagation. (a) p=1. (b) p=2. (c) p=3. (d) p=4. (e) p=8. (f) p=16

(i) numerical results (ii) paraxial approximation. (iii) variational method.

The focusing distance in the paraxial approximation $\bar{z}_f$ is $\left(\infty, 1, \sqrt{2}/2, \sqrt{3}/3, \sqrt{7}/7, \sqrt{15}/15\right)$

for respectively p=(1,2,3,4,8,16).

Fig. 3-2 The regularized longitudinal phase is plotted as a function of the normalized distance of propagation.(a) p=1. (b) p=2. (c) p=3. (d) p=4. (e) p=8. (f) p=16.

(i) numerical results (ii) paraxial approximation. (iii) variational method.

The focusing distance in the paraxial approximation $\bar{z}_f$ is $\left(\infty, 1, \sqrt{2}/2, \sqrt{3}/3, \sqrt{7}/7, \sqrt{15}/15\right)$

for respectively p = (1,2,3,4,8,16).

Fig. 3-3a The beam transverse profile is plotted as a function of $\bar{r}$ at $\bar{z}$=2.5 for p=4.

Fig. 3-3b The off-axis total phase minus the on-axis total phase is plotted as a function of $\bar{r}$ at $\bar{z}$=2.5 for p=4.

Fig. 3-4 The focusing distance $\bar{z}_f$ is plotted as a function of the ellipticity for different values of $\tilde{p}$. a) $\tilde{p}$=1/2. b) $\tilde{p}$=1 c) $\tilde{p}$=2 d) $\tilde{p}$=4

(i) numerical results (ii) paraxial approximation. (iii) variational method.

Fig. 3-5a The beam transverse x-profile is plotted as a function of $\bar{x}$ at different $\bar{z}$ for $\tilde{p}$=4 and $\varepsilon = 10$.

Fig. 3-5b The beam transverse y-profile is plotted as a function of $\bar{y}$ at different $\bar{z}$ for $\tilde{p}$=4 and $\varepsilon = 10$.

Fig. 3-6a The beam transverse x-profile is plotted as a function of $\bar{x}$ at $\bar{z}$=0.7 for $\tilde{p}$=4 and $\varepsilon = 10$.

Fig. 3-6b The beam transverse y-profile is plotted as a function of $\bar{y}$ at $\bar{z}$=0.7 for $\tilde{p}$=4 and $\varepsilon = 10$.

(i) numerical results (ii) paraxial approximation. (iii) variational method.

Fig. 3-7a The exact spatial Fourier transform of the beam envelope for the case described in fig.3-5.a.

Fig. 3-7b The exact spatial Fourier transform of the beam envelope for the case described in fig.3-5.b.

Fig. 3-8 The x (solid line) and y (broken line) cross-sections of the field amplitude are plotted for the following parameters right before the onset of self-focusing.

a) $\tilde{p} = 0.5 \quad \varepsilon = 3$
b) $\tilde{p} = 0.5 \quad \varepsilon = 6$
c) $\tilde{p} = 0.5 \quad \varepsilon = 8$
d) $\tilde{p} = 1.0 \quad \varepsilon = 2$
e) $\tilde{p} = 1.0 \quad \varepsilon = 3$
f) $\tilde{p} = 4.0 \quad \varepsilon = 2$
g) $\tilde{p} = 4.0 \quad \varepsilon = 3$

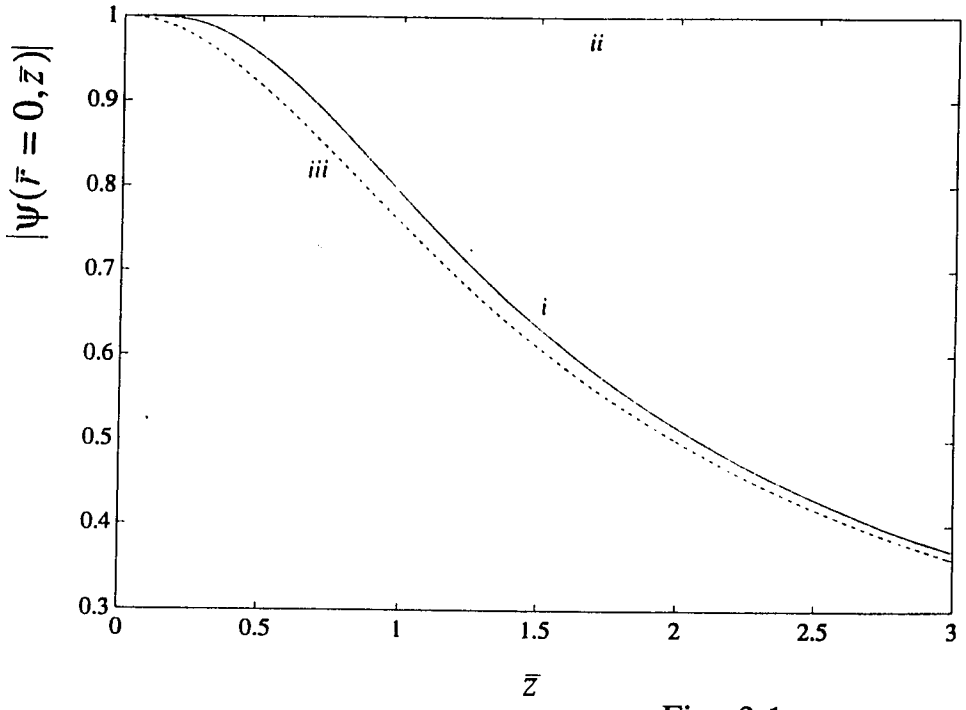

Fig. 3.1a

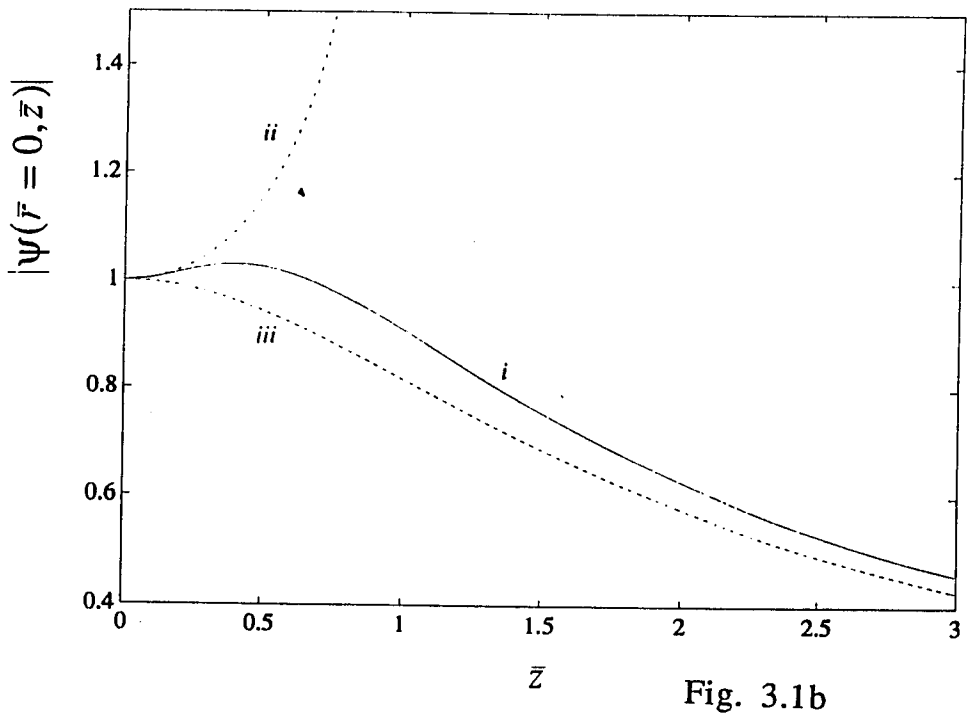

Fig. 3.1b

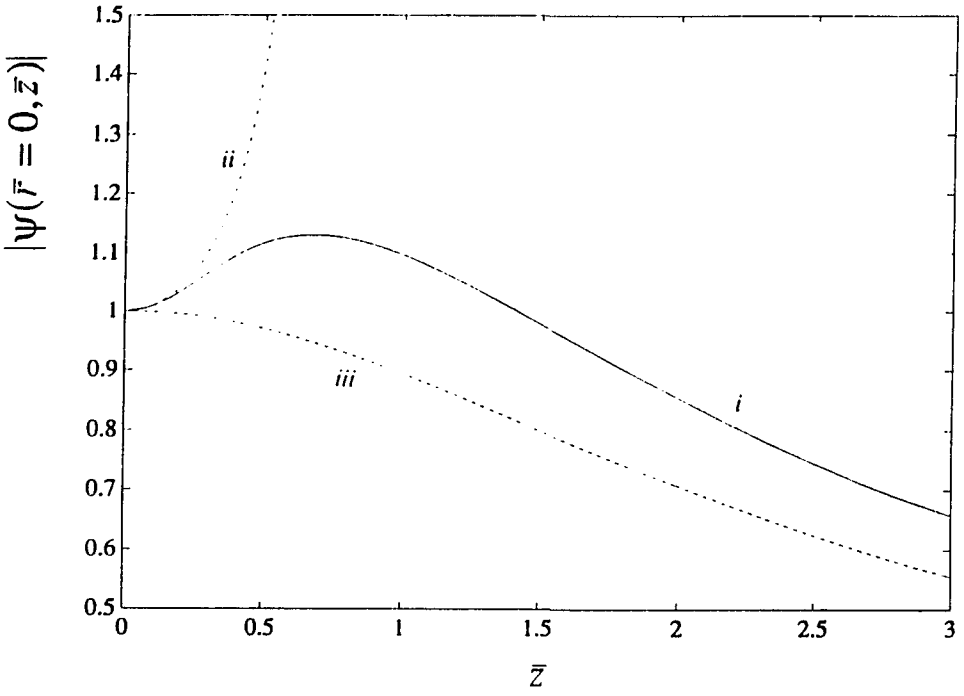

Fig. 3.1c

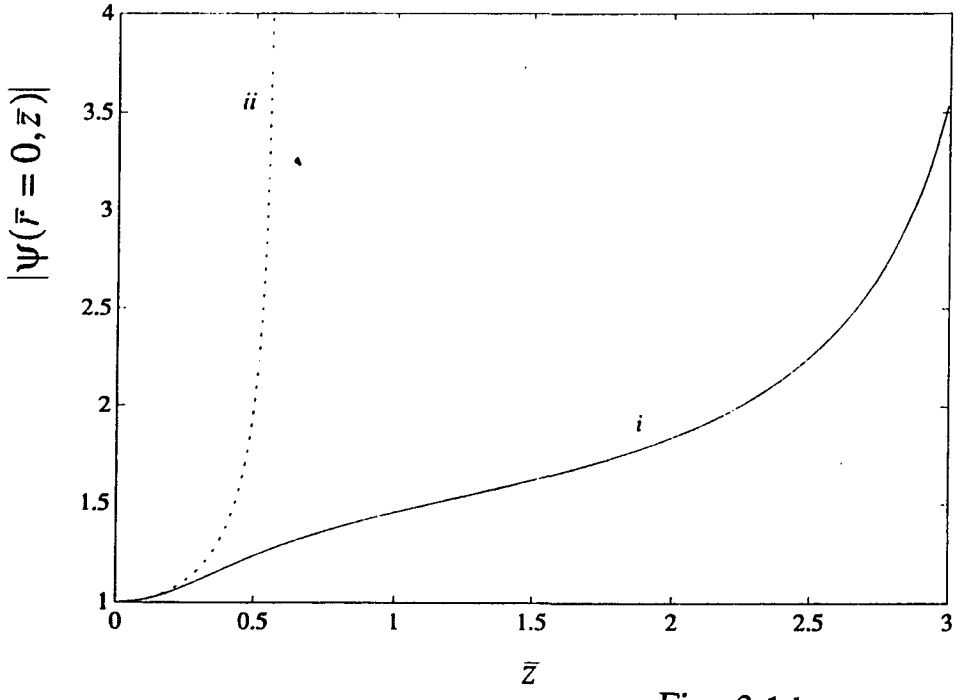

Fig. 3.1d

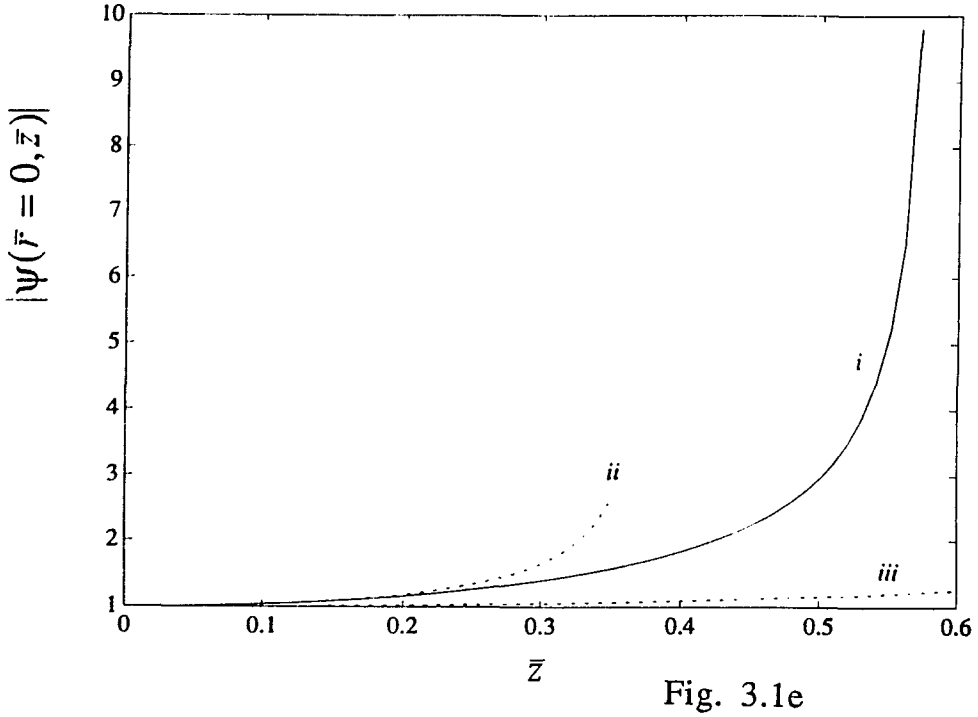

Fig. 3.1e

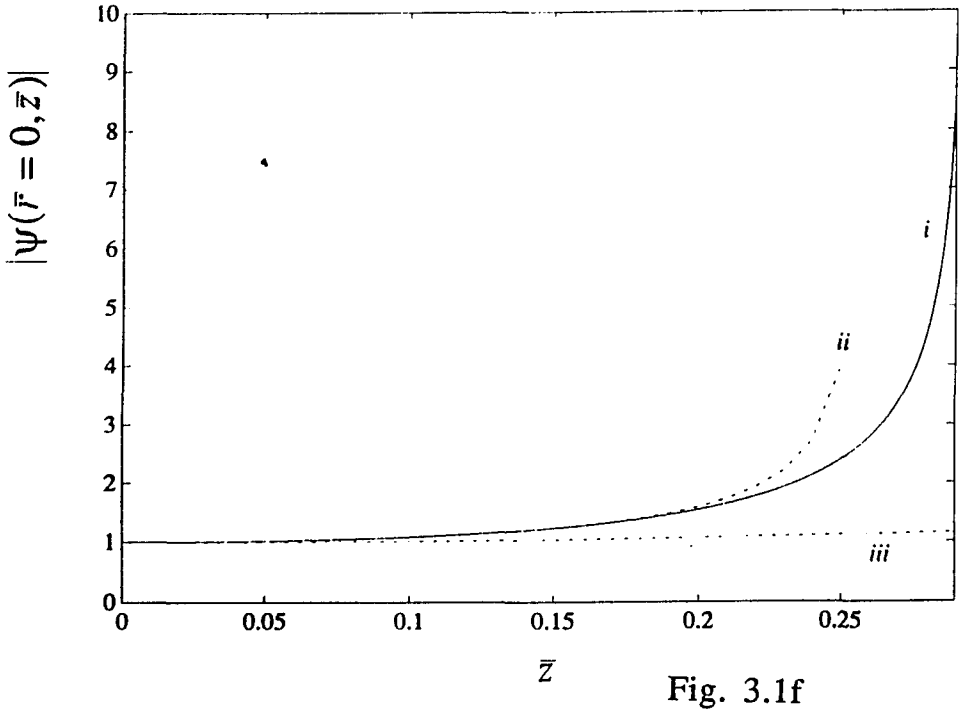

Fig. 3.1f

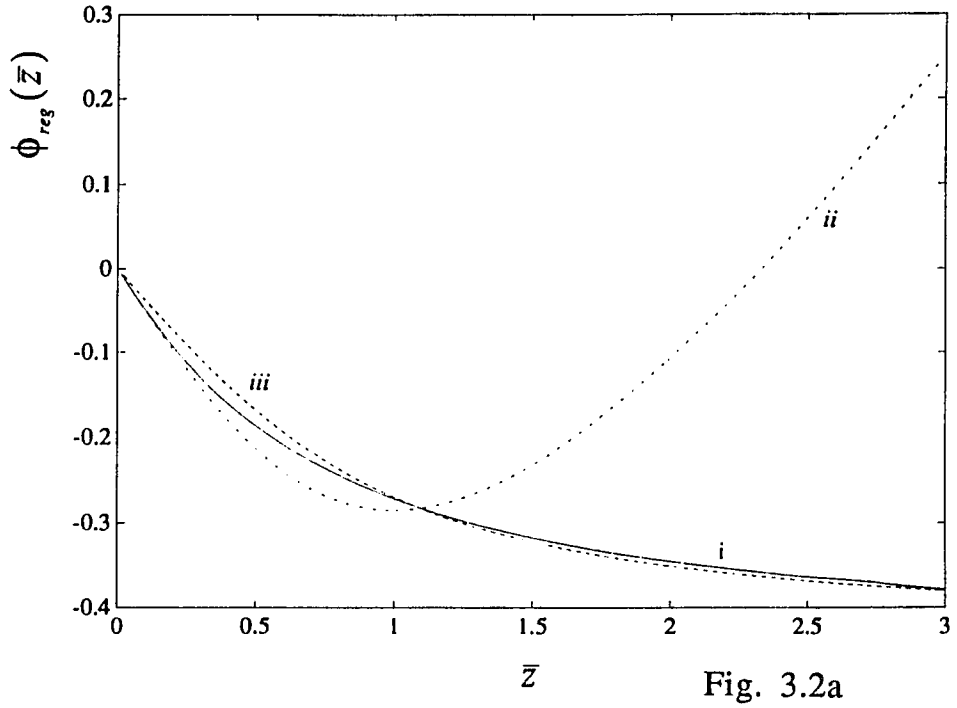

Fig. 3.2a

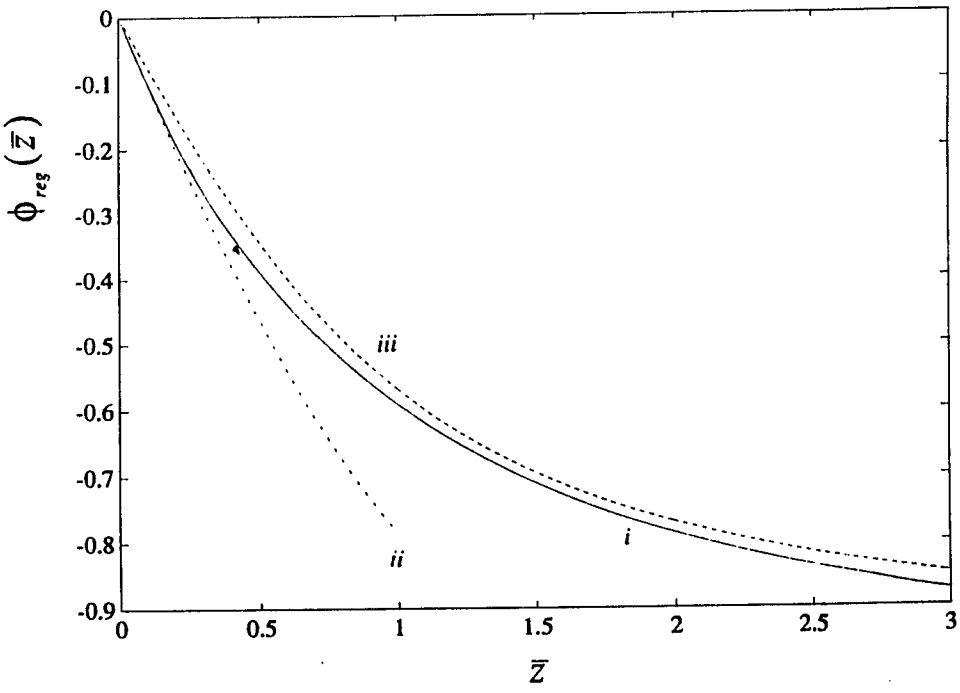

Fig. 3.2b

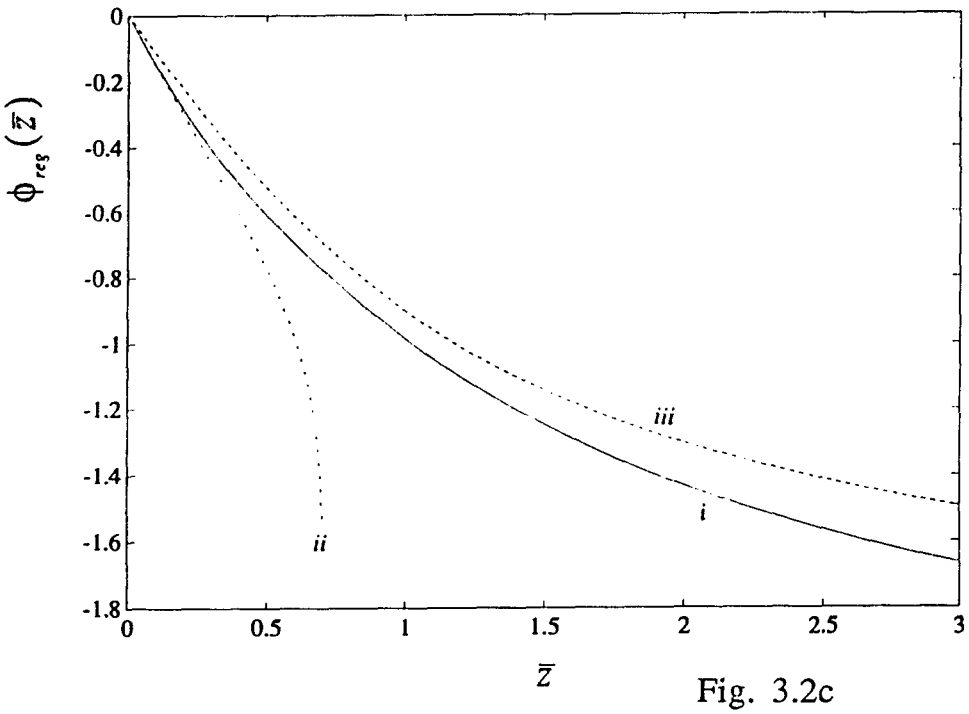

Fig. 3.2c

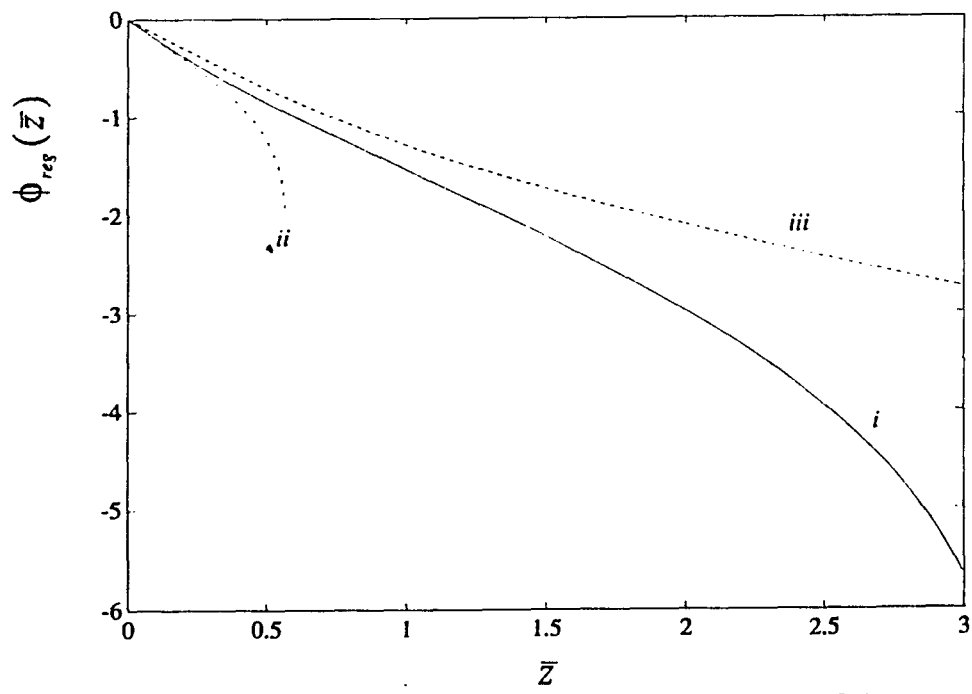

Fig. 3.2d

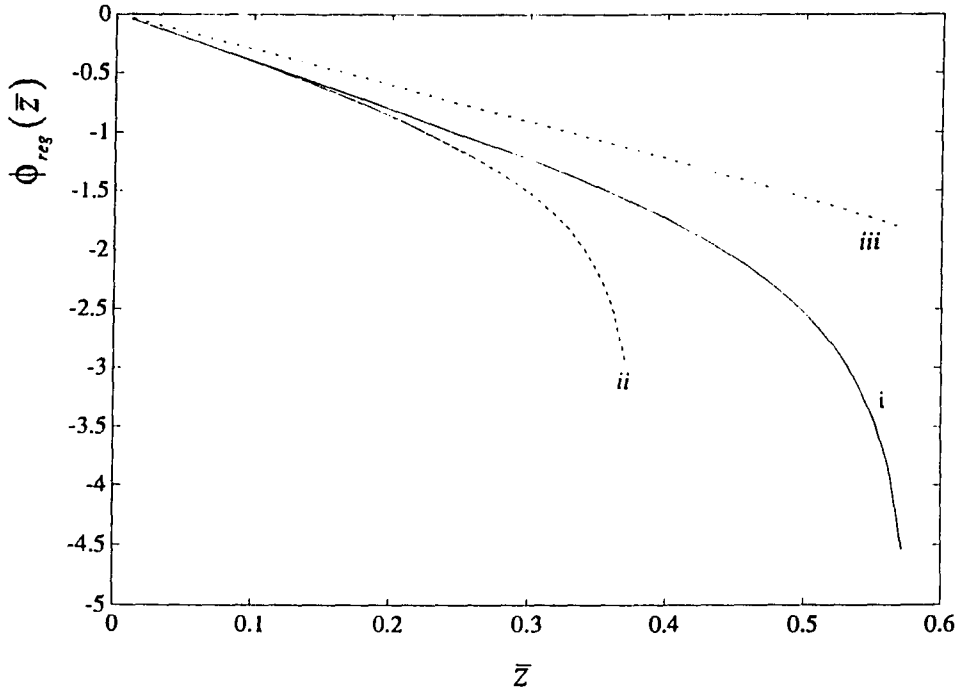

Fig. 3.2e

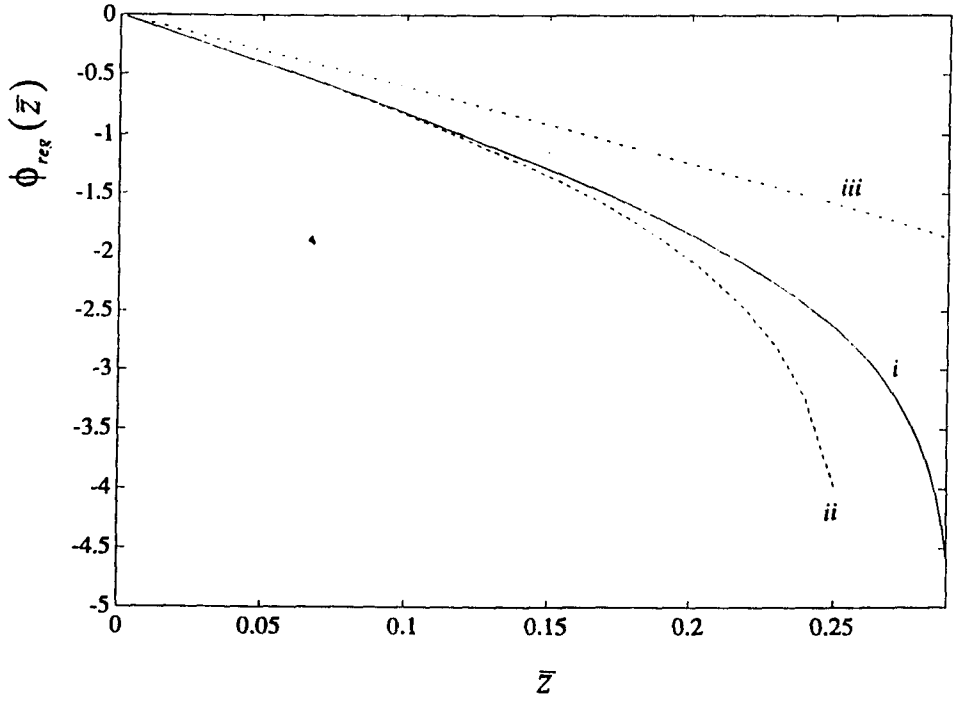

Fig. 3.2f

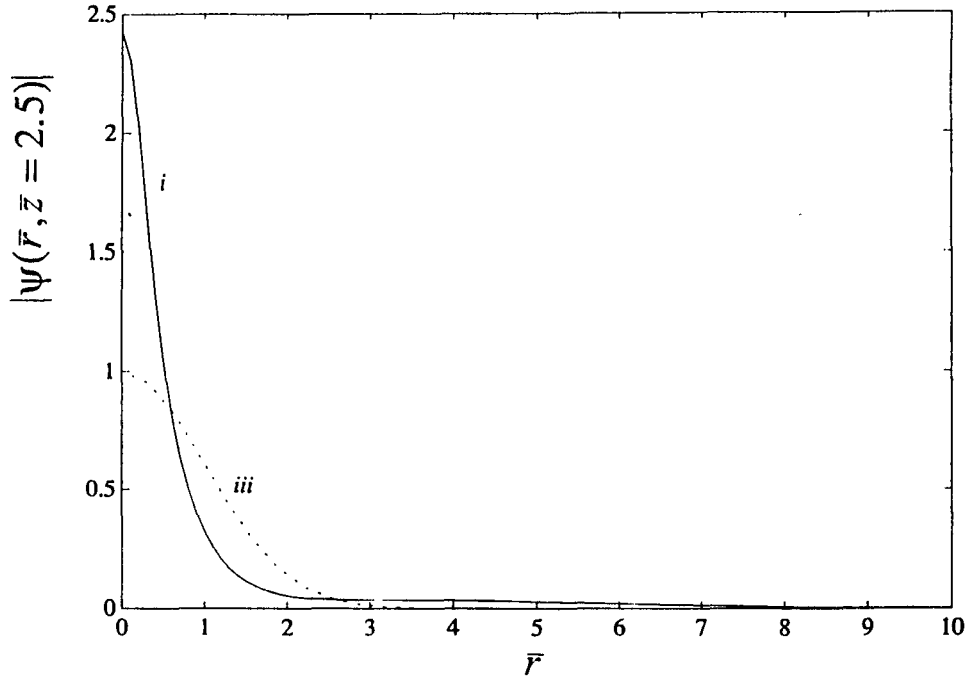

Fig. 3.3a

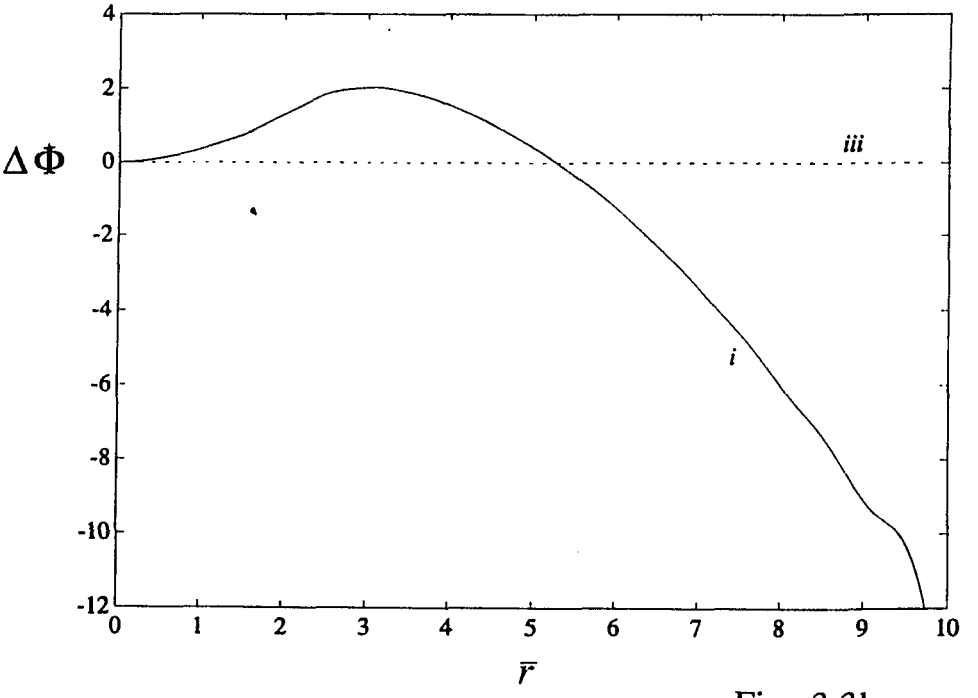

Fig. 3.3b

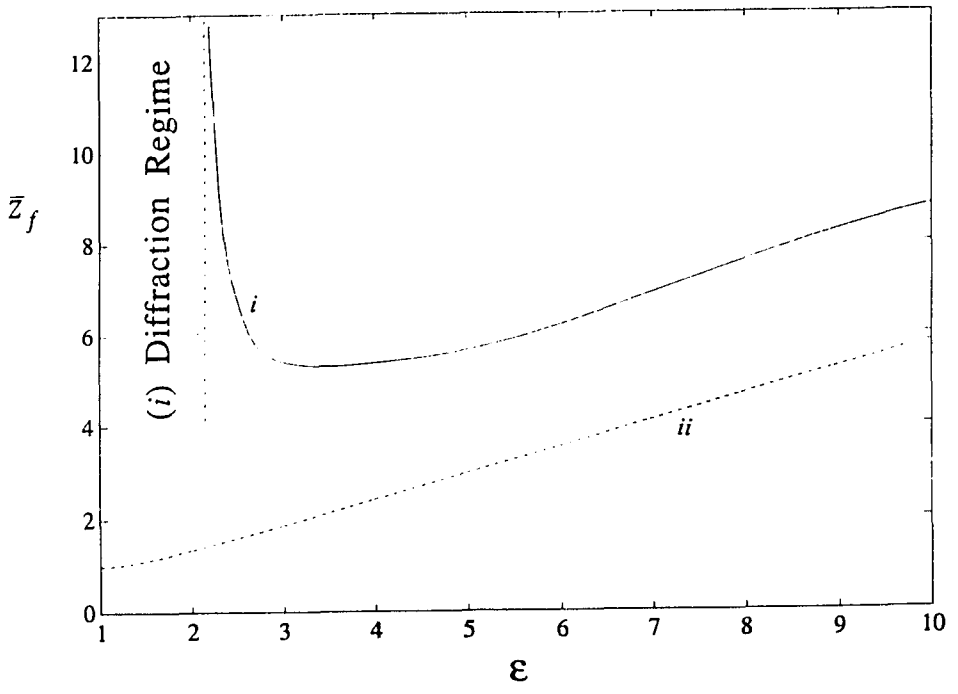

Fig. 3.4a

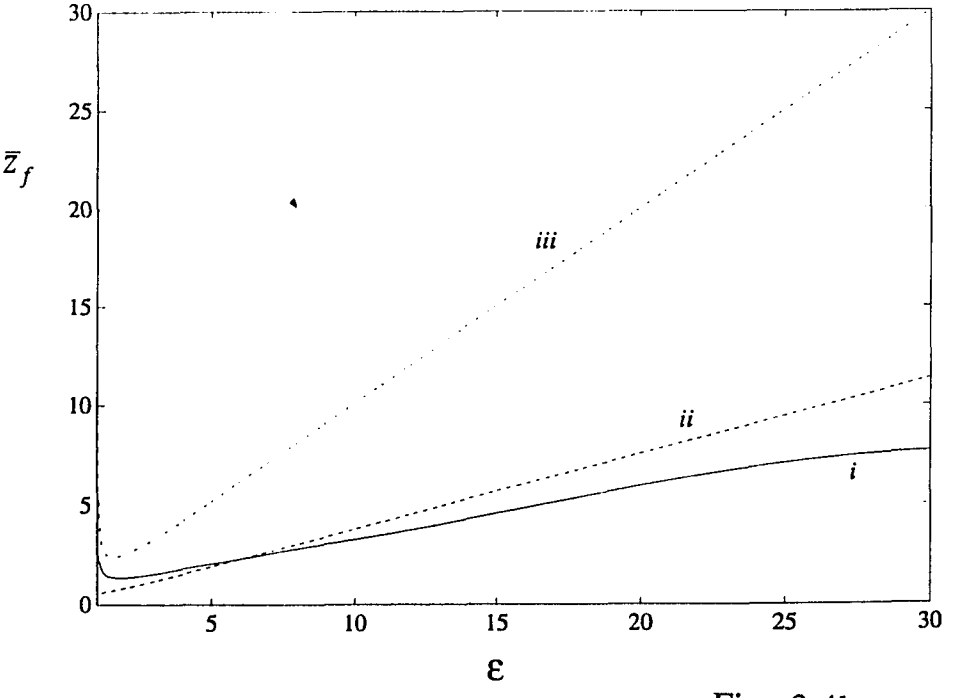

Fig. 3.4b

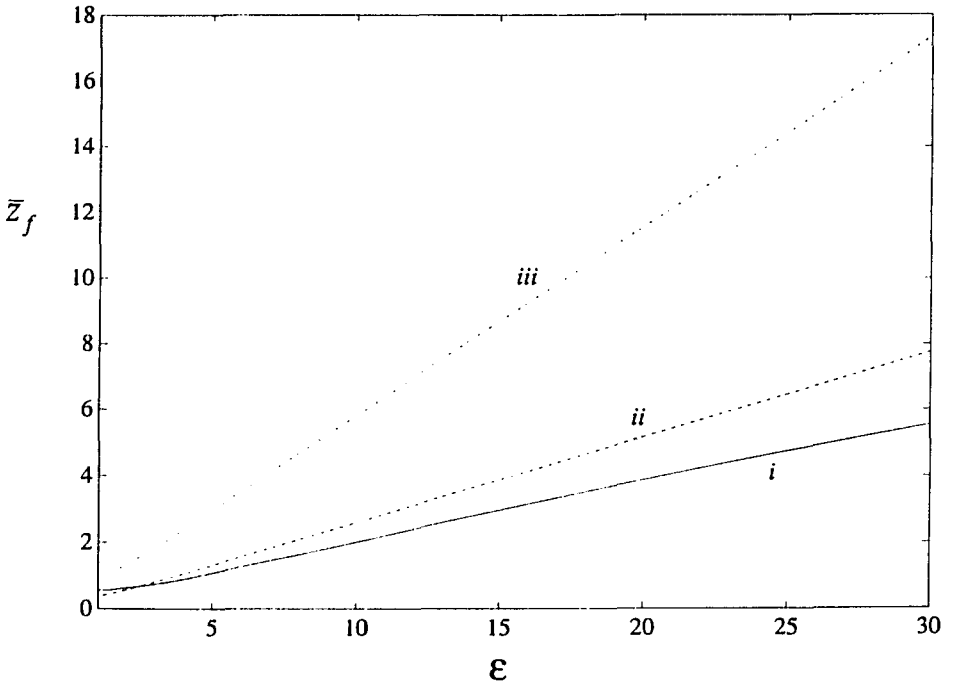

Fig. 3.4c

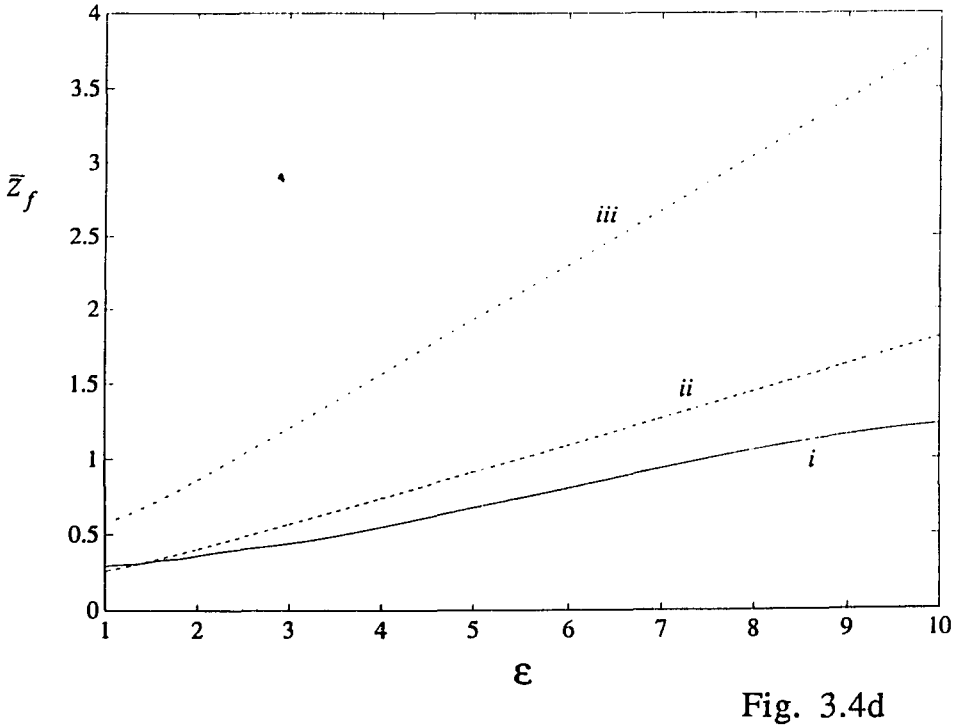

Fig. 3.4d

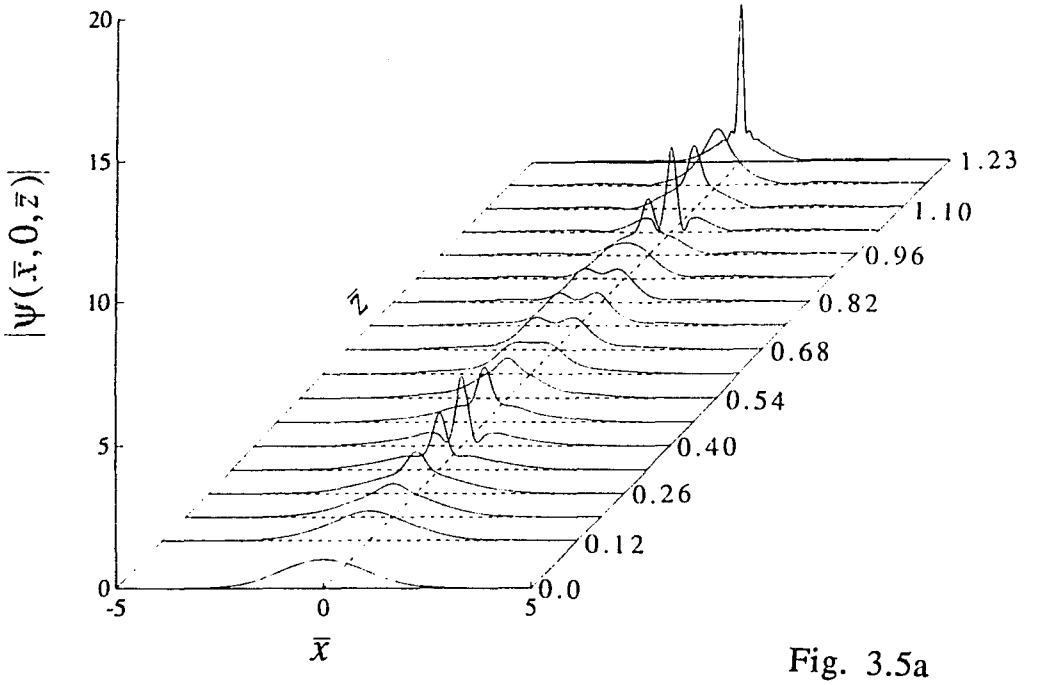

Fig. 3.5a

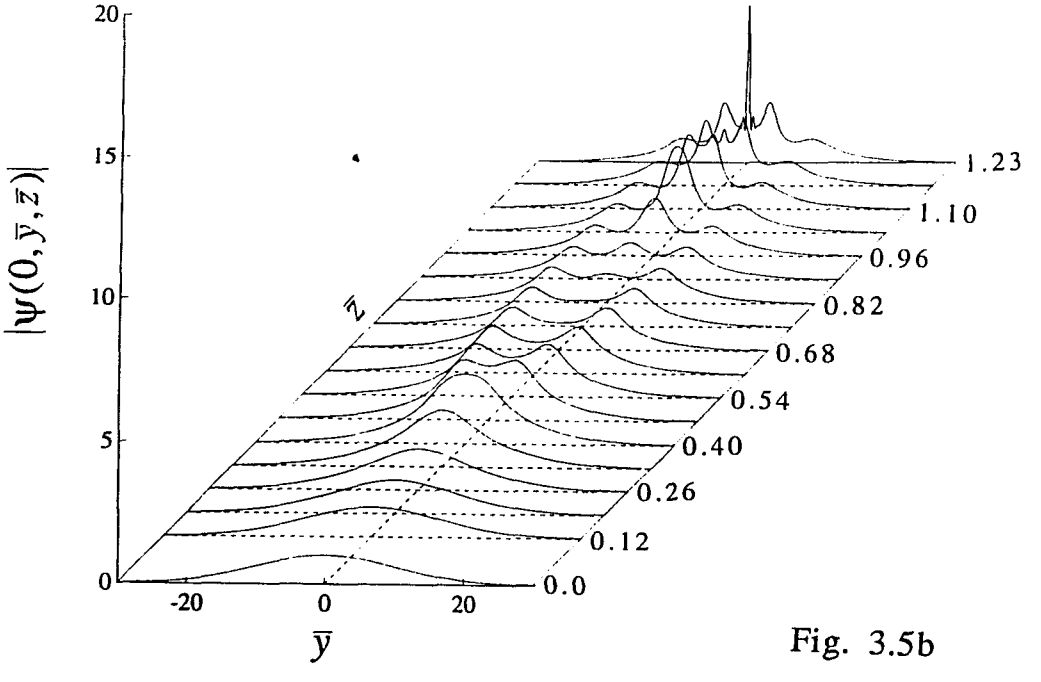

Fig. 3.5b

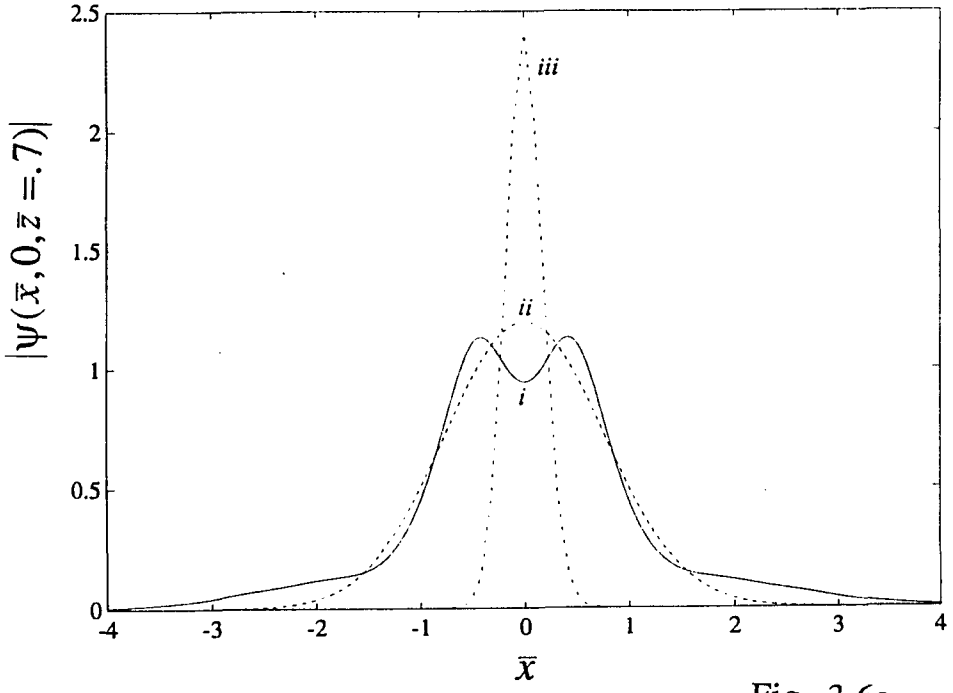

Fig. 3.6a

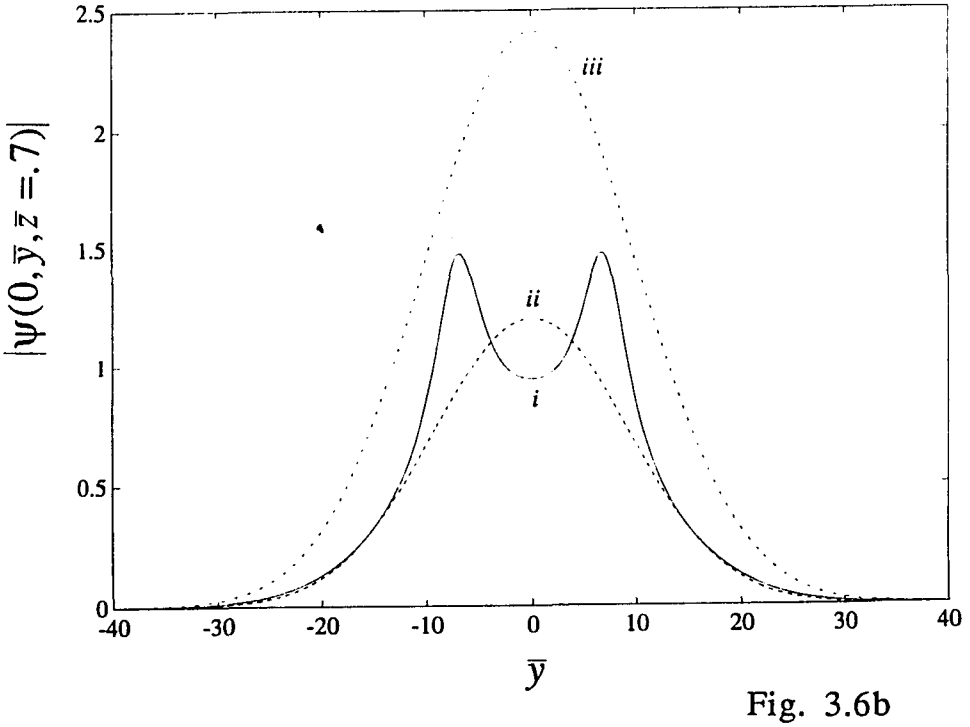

Fig. 3.6b

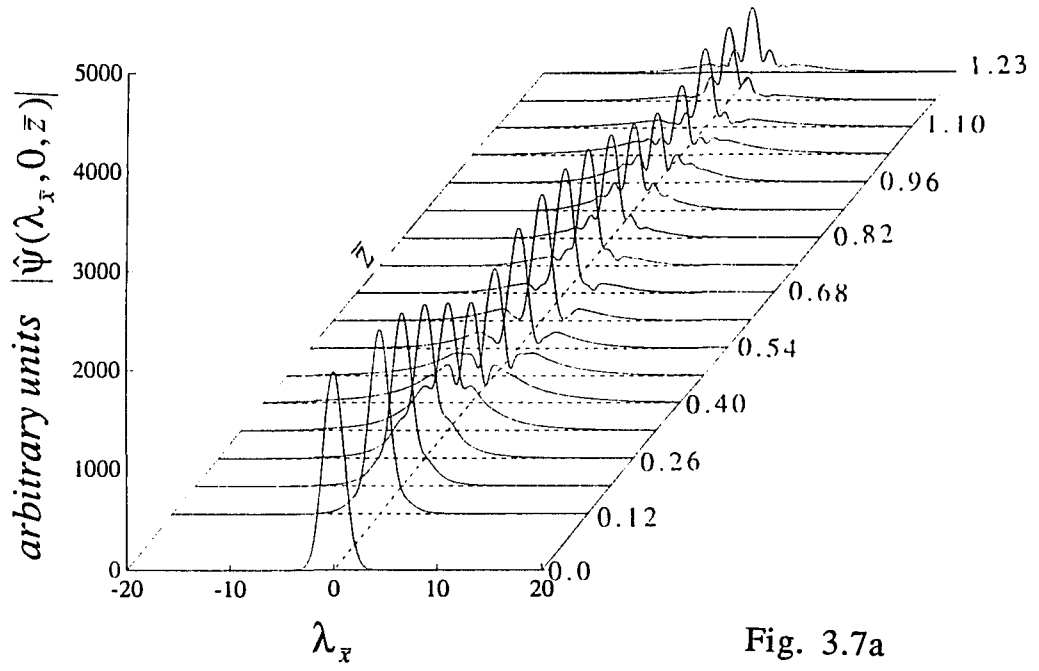

Fig. 3.7a

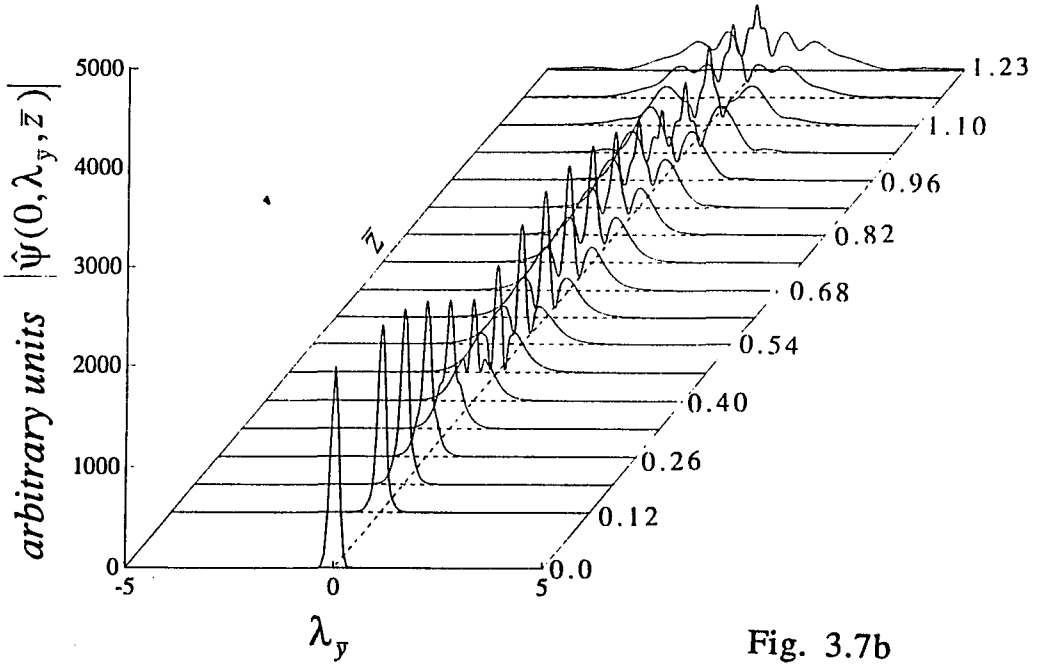

Fig. 3.7b

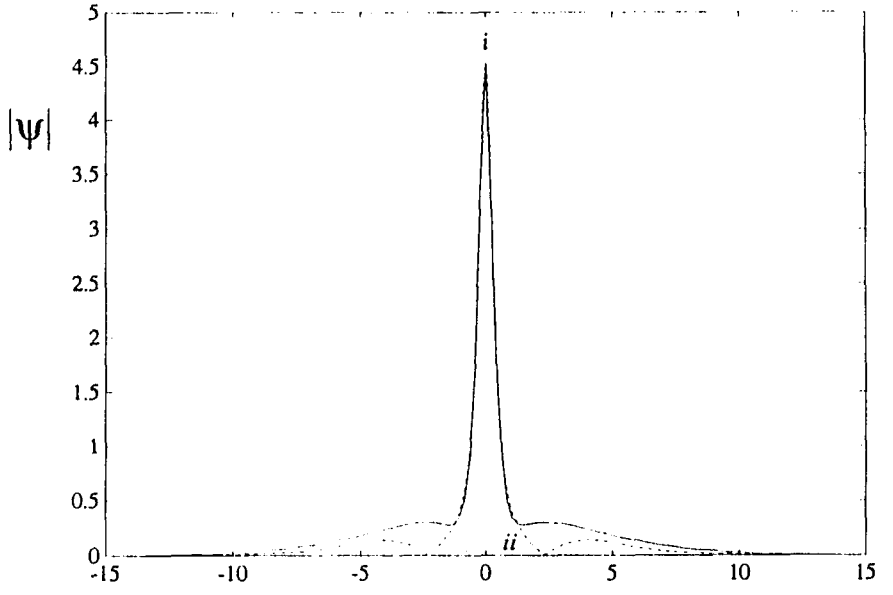

Fig. 3.8a

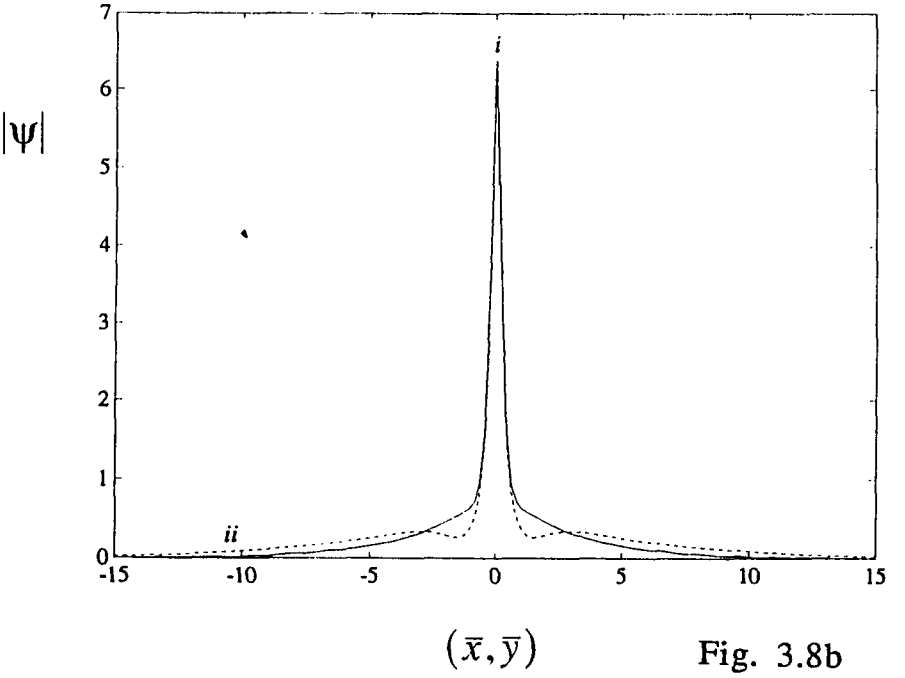

Fig. 3.8b

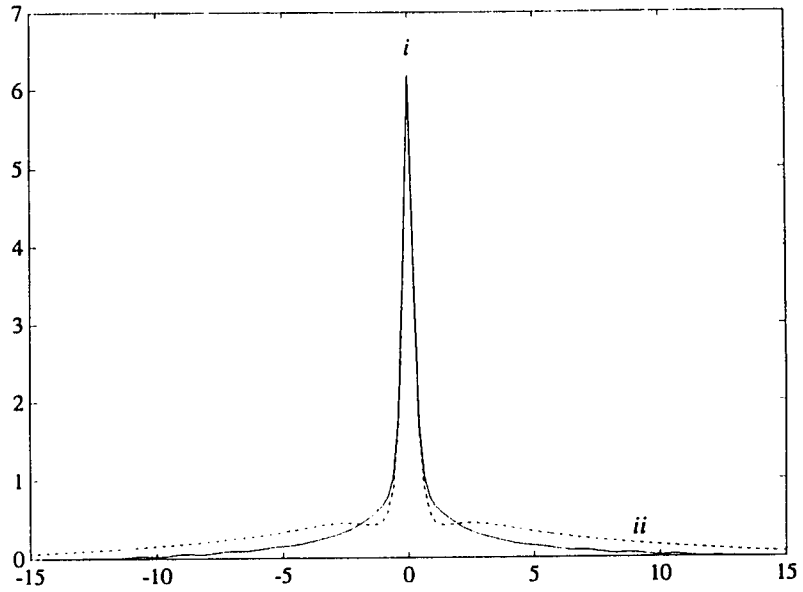

$(\bar{x}, \bar{y})$

Fig. 3.8c

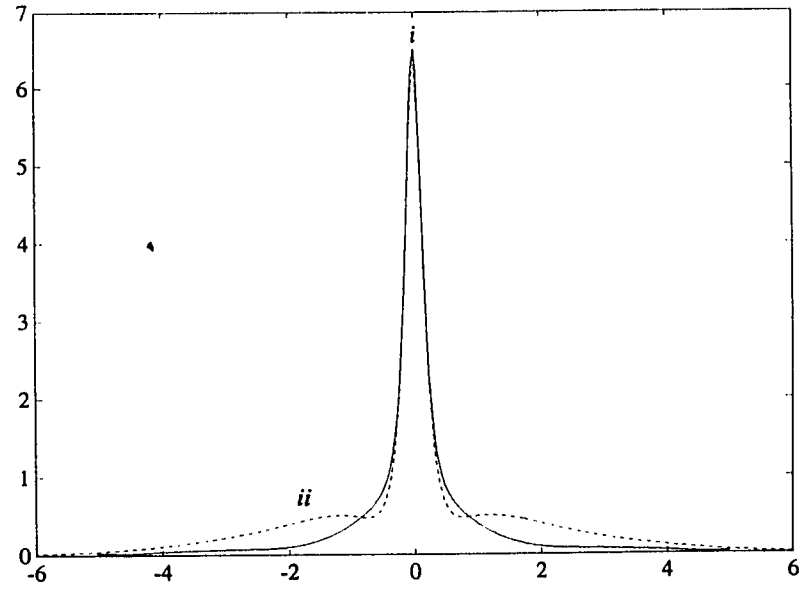

$(\bar{x}, \bar{y})$

Fig. 3.8d

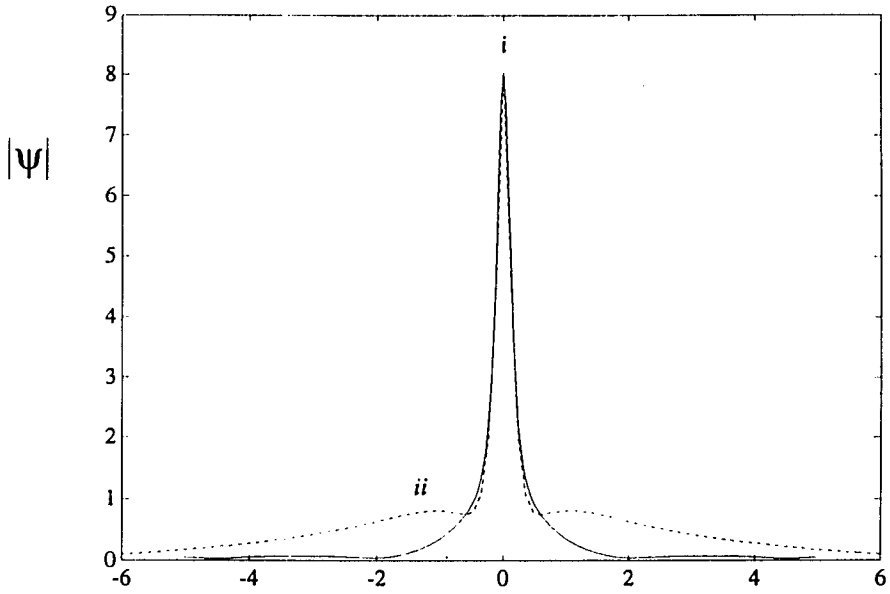

Fig. 3.8e

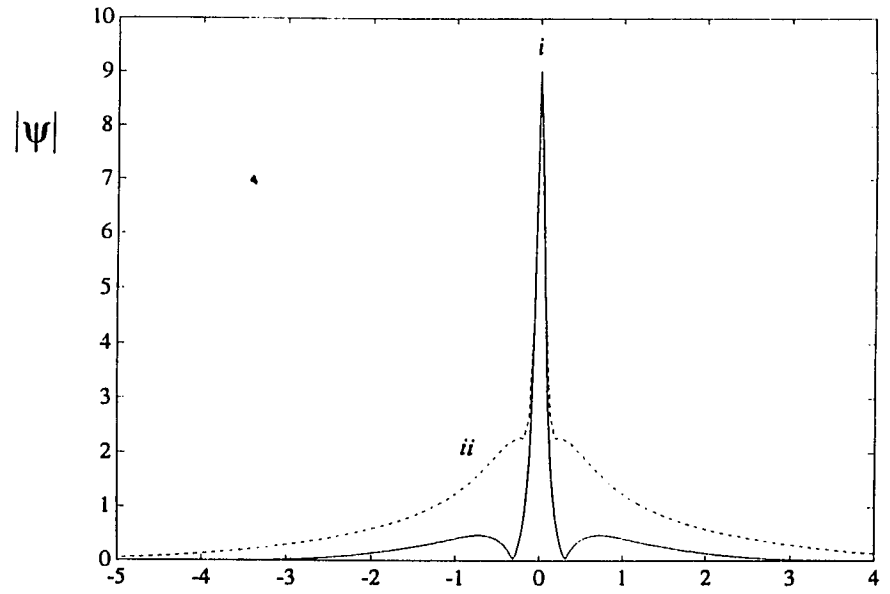

Fig. 3.8f

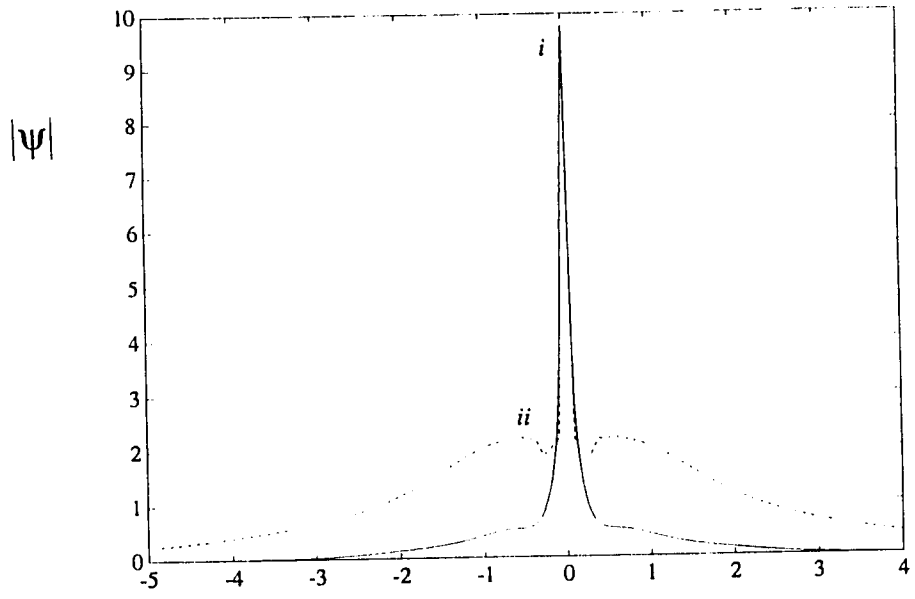

Fig. 3.8g

4.1) Pulse Propagation in Resonant Medium: Historical Perspectives

The propagation of intense pulses in nonlinear media has been treated to this point by a phenemological model which includes the Kerr and higher order nonlinearities. This model is useful when the pulse spectrum is far from any natural resonances of the medium. When the medium resonance is near the spectrum of the pulse, resonant effects must be included. In this case, the proper model consists of simultaneously solving the optical Bloch equations which describe the evolution of the density matrix which describes an assembly of two level systems and the Maxwell equation. The macroscopic polarization can then be calculated from the Bloch equations and is used as the driving term in the Maxwell equation describing the evolution of the pulse.

The concept of Bloch equations was used to describe the evolution of spin 1/2 systems [56]. Pulse propagation in a resonant two level medium was shown to be equivalent to the spin 1/2 system in the rotating wave approximation. The equation of motion for the density matrix follows the Louisville equation [57]

$$i\hbar\frac{\partial\rho}{\partial t}=[H,\rho] \qquad \text{where} \qquad H=H_0+H_{\text{int}} \tag{4-1.1}$$

In the dipole approximation

$$H_{\text{int}}=-\vec{p}\cdot\vec{E} \tag{4-1.2}$$

If the two atomic levels are labeled

$|1\rangle$ and $|2\rangle$

then the matrices describing the two-level system and its interaction are

$$H_0 = \hbar \begin{bmatrix} \omega_1 & 0 \\ 0 & \omega_2 \end{bmatrix} \tag{4-1.3a}$$

$$H_{\text{int}} = E(t) \begin{bmatrix} 0 & d \\ d & 0 \end{bmatrix} \tag{4-1.3b}$$

where $d = \langle 1 | \vec{p} | 2 \rangle$

Using the Bloch vector symbolism [58], the coupled nonlinear ordinary differential equations for the density matrix elements are

$$i\dot{p} = \omega_0 p - n \frac{\gamma_e^2 \hbar}{2} E - i\gamma_2 p \tag{4-1.4a}$$

$$i\dot{n} = \frac{1}{\hbar}\left(p^* E - p E^*\right) + i\gamma_1 (n_i - n) \tag{4-1.4b}$$

where $\omega_0 = \omega_2 - \omega_1$

Here, ω_0 is the atom resonance frequency , n is the difference in population between the ground and excited states , n_i is the initial condition for n , γ_e is the gyroelectric ratio for the two-level atoms system , where $p = p_1 + i p_2$, the Bloch vector is $\left(p_1, p_2, n(\gamma_e \hbar / 2)\right)$ and γ_1 and γ_2 are respectively the longitudinal and transverse decay rates (i.e. the decay rates associated with the diagonal and off-diagonal elements of the density matrix). We write for E and p

$$E = E_0 \phi \exp[-i\omega_c t + i k_c z] \tag{4-1.5a}$$

$$p = d\chi \exp[-i\omega_c t + i k_c z] \tag{4-1.5b}$$

where ω_c is the center frequency of the pulse .In the comoving system

$$U = \frac{z}{v_g \tau} - \frac{t}{\tau}, \quad V = \frac{z}{v_g \tau} \tag{4-1.6}$$

where τ is the initial pulse width, and v_g is the group velocity, the Bloch equations can be written as

$$-i \frac{\partial \chi}{\partial U} = \left[\Delta - i \Gamma_2 \right] \chi - \frac{\theta}{2} (n \phi) \tag{4-1.7a}$$

$$-i \frac{\partial n}{\partial U} = \theta \left(\chi^* \phi - \phi^* \chi \right) + i \Gamma_1 \left(n_i - n \right) \tag{4-1.7b}$$

where the dimensionless parameters θ, Δ, Γ_1 ,and Γ_2 are defined as $\theta = d E_0 \tau / \hbar, \Delta = \left(\omega_0 - \omega_c \right) \tau, \Gamma_1 = \gamma_1 \tau$,and $\Gamma_2 = \gamma_2 \tau$. The macroscopic polarization density due to the active atoms is given by ρp, where ρ is the number density of the two-level atoms. If the medium is considered optically thin, then the transient response of the polarization is calculated as if the excitation pulse is not effected by the transient response of the system. In this way, a number of resonant transient phenomenon such as transient nutation, free induction decay, photon echoes and transient 4-wave mixing are studied [59].

If the sample medium is not optically thin, the excitation field is continuously changed owing to the medium response and the propagation effect can not be ignored. It is this propagation phenomenon which adds richness to the study of optical systems as

opposed to the magnetic spin systems studied earlier. The propagation effect must be included in studying phenomenon such as Self-Induced Transparency [60] and Super Florescence [61].

4.2) Pulse Propagation in Resonant Media (Fiber Amplifier) [e]

Recent experimental and theoretical work on the amplification of ultrashort pulses in fiber amplifiers shows the necessity of including the active medium nonlinear gain, saturation, and dispersion [62-65] Our model differs from [66] in that we include the effects of $\beta^{(3)}$, ISRS and SS, from [67] in that we make no adiabatic or perturbative approximations, and from [68-70] in that no stationary solution is assumed and that we include the $\beta^{(3)}$, ISRS and SS terms. In order to efficiently amplify ultrashort pulses requires a large gain bandwidth which is governed by the transverse relaxation rate in the Bloch formalism. An attractive dopant for such purposes is erbium ion. The advantages [71,72] of erbium as a dopant agent is the large gain near the 1.5μm wavelength which corresponds to the minimum loss wavelength in fused silica fiber, low noise, wide bandwidth (30 n.m.), polarization sensitivity and high saturation output power.

We show in detail the contribution of each of the above effects to the obtained solutions. Our main conclusion is that a detailed quantitative analysis of the problem requires the use of the full Maxwell-Bloch model.We show the need of this model by contrasting the complete model to a frequently used approximation model of the gain medium [73]. In this phenemological model, the gain bandwidth and saturation are described

$$g(\Omega) = g_p(U) \cdot \left(1 - \frac{\Omega^2}{\gamma_2{}^2}\right) \qquad (4\text{-}2.1)$$

and the gain peak saturation is described by

$$g_p(U) = g_p \exp\left(s \int_{\infty}^{U} |\phi(u)|^2 \, du \right) \qquad \text{with } s = \frac{P_0 \tau}{E_S} \tag{4-2.2}$$

where

P_0 = pulse peak power

E_S = medium saturation energy

g_p = peak gain without saturation

The full coupled model which is used to model the active fiber in the spectral domain is accomplished as follows:

If we define the Fourier transform of the field envelope as:

$$\tilde{\phi}(\Omega, V) = \mathbf{F}[\phi(U,V)] = \frac{1}{\sqrt{2\pi}} \int_{-\infty}^{\infty} \exp(i\Omega U)\, \phi(U,V)\, dU \tag{4-2.3}$$

then the differential equation for $\tilde{\phi}$ is the differential equation for the passive fiber to which is added a function representing the polarization response of the active medium, specifically

$$\begin{aligned} \frac{\partial \tilde{\phi}(\Omega,V)}{\partial V} = & -\alpha_l\, \tilde{\phi}(\Omega,V) + \frac{i\varepsilon K}{2}\left(1 - \frac{\Omega}{K}\right)\mathbf{F}\left[|\phi(U,V)|^2\, \phi(U,V)\right] \\ & + \frac{i\varepsilon K}{2}\mathbf{F}\left\{\phi(U,V)\mathbf{F}^{-1}\left[\chi_R(\Omega)\mathbf{F}\left[|\phi(U,V)|^2\right]\right]\right\} \\ & + i\left(v_g \tau\right) \sum_{k=2}^{\infty} (-1)^k \frac{\beta^{(k)} \Omega^k}{k!\, \tau^k}\, \tilde{\phi}(\Omega,V) \\ & - i\, \hat{\psi}\left[-K + 2\Omega - \frac{\Omega^2}{K}\right]\tilde{\chi}(\Omega,V) \end{aligned} \tag{4-2.4}$$

where α_l is the coefficient of nonresonant linear absorption in the fiber, $\varepsilon = \frac{n_2 |E_0|^2}{n_0}$, n_0 is the linear index of refraction of the fiber, n_2 is the fiber Kerr nonlinear index of refraction including geometric factors resulting from the transverse averaging of the mode over the fibre cross-section, $K = \omega_c \tau$, ω_c is the pulse center frequency, χ_R is the generalized Raman Scattering susceptibility (described more fully in the modelling of the passive fiber in the supercontinuum generation) for the passive fiber, $\beta^{(k)}$ is the k^{th} derivative of the propagation constant with respect to the angular frequency evaluated at the pulse center frequency , $\hat{\psi} = \frac{\rho d E_0}{2 \varepsilon_r E_0^2}$, and ε_r is the permittivity of the passive fiber. The first term on the r.h.s of the evolution equation represents the linear absorption in the fiber, the second term represents the Self-Phase-Modulation contribution, the third term (the term proportional to Ω/K) represents self-steepening, the fourth term represents Raman scattering which is responsible for the soliton self-frequency shift, the fifth terms (the summation) represent the chromatic dispersion terms and the last parenthesis represents the second time-derivative of the active atoms polarizability.

This equation is integrated, keeping only the $\beta^{(2)}$ and $\beta^{(3)}$ terms of the chromatic dispersion series.If the distance is measured in units of the dispersion length and the nonlinear coupling is measured in the soliton units:

$$\bar{z} = \frac{z}{z_0} = \frac{z\left|\beta^{(2)}\right|}{\tau^2} \ , \ \delta = \frac{\beta^{(3)}}{\left|\beta^{(2)}\right|\tau} \ , \quad \text{and} \quad \mathbf{N}^2 = \frac{\pi\tau^2}{\lambda\left|\beta^{(2)}\right|} n_2 E_0^2$$

Then the small c.w. signal amplitude gain coefficient per dispersion length, due to the presence of the active medium, is given by:

$$g = -\frac{n_i \theta K}{2\Gamma_2} \frac{\rho d \tau}{2\varepsilon_r v_g \left|\beta^{(2)}\right| E_0} \qquad (4\text{-}2.5)$$

For the fiber amplifier, the initial conditions used were: $n(U=\infty,\bar{z}) = -1, \chi(U=\infty,\bar{z}) = 0$ and $\phi(U,0) = \mathrm{sech}(U)$ which describes the amplification of a fundamental soliton in a completely inverted collection of two level atoms. The polarization is zero before the excitation pulse enters the system. To integrate this system requires a combination of transverse integration using a Runge-Kutta scheme , Fast Fourier Transform methods to convert into the spectral domain and longitudinal propagation of the field using a Runge-Kutta scheme. The numerical procedure was tested in the following ways.

1) The fiber gain was shut off and the passive fiber results were obtained.

2) The fiber processes were shut off and the solution of the following analytically integrable system (T_1 very large) for homogeneously broadened systems were recovered. This integrable system are the so called solutions of Self-Induced Transparency [74].

$$\frac{\partial \phi}{\partial V} = i\hat{\psi} K \chi \tag{4-2.6a}$$

$$\frac{\partial \chi}{\partial U} = i\gamma_2 \bar{\Delta} \chi - \frac{i\theta n \phi}{2} \tag{4-2.6b}$$

$$\frac{\partial n}{\partial U} = -2\theta \,\mathrm{Im}\left(\chi^* \phi\right) \tag{4-2.6c}$$

$$If \qquad \phi(U,0) = \frac{2}{\theta}\,\mathrm{sech}(U) \tag{4-2.7a}$$

$$\phi(U,V) = \frac{2}{\theta}\,\mathrm{sech}\left(U - U_{sh}(V)\right)\exp\left(i\varphi(V)\right) \tag{4-2.7b}$$

$$U_{sh}(V) = \frac{-\gamma_2 \tau g V}{\left(1 + \left(\gamma_2 \tau \bar{\Delta}\right)^2\right)} \tag{4-2.7c}$$

$$\varphi(V) = \frac{\left(\gamma_2 \tau\right)^2 g \bar{\Delta} V}{\left(1 + \left(\gamma_2 \tau \bar{\Delta}\right)^2\right)} \tag{4-2.7d}$$

$$n(U,V) = 1 - \frac{2\,\mathrm{sech}^2\left(U - U_{sh}(V)\right)}{\left(1 + \left(\gamma_2 \tau \bar{\Delta}\right)^2\right)} \tag{4-2.7e}$$

$$\mathrm{Re}\left(\chi \exp(-i\varphi)\right) = \frac{\gamma_2 \tau \bar{\Delta}\,\mathrm{sech}\left(U - U_{sh}(V)\right)}{\left(1 + \left(\gamma_2 \tau \bar{\Delta}\right)^2\right)} \tag{4-2.7f}$$

$$\mathrm{Im}\left(\chi \exp(-i\varphi)\right) = \frac{\tanh\left(U - U_{sh}(V)\right)\mathrm{sech}\left(U - U_{sh}(V)\right)}{\left(1 + \left(\gamma_2 \tau \bar{\Delta}\right)^2\right)} \tag{4-2.7g}$$

In these variables, the gain is

$$g = -\frac{n_i \theta K}{2\Gamma_2} \frac{\rho d}{2\varepsilon_r E_0} \quad \text{and} \quad \bar{\Delta} = (\omega_o - \omega_c) T_2$$

Since we have seen that the Raman Scattering plays a significant role in the evolution of higher order solitons and that the amplifier adds energy continuously to the pulse, we expect large spectral shifts and the generation of multiple stokes pulses. Therefore the phenemological model of the gain line will become a poor model when the spectrum of the pulse becomes comparable to the gain bandwidth. The phenemological model which uses a parabolic model to model the gain line will attenuate the red shifted stokes spectrum as it becomes shifted from the gain window. The complete model shows that the gain line goes to zero far from the gain center and therefore the stokes pulse will propagate without attenuation.
We note:

1) In fig. 4-1, we plot the evolution of the temporal profile as a function of propagation distance. The initial amplification of the fundamental soliton through the fiber causes a simultaneous amplification and temporal compression consistent with soliton propagation. To this point, the two models agree quite well. At some point, the pulse breaks up into radiation near the carrier frequency and a stokes red-shifted pulse. The dynamics of the stokes pulse due to the passive fiber Raman Scattering is the dominant evolution process. This is clearly seen in fig. 4-2a, where the full model is compared to the full model minus nonlinear terms taken one at a

time at the exit plane. We see that while the Raman scattering is the dominant process, the other effects give non-negligible contribution to the temporal dynamics. In fig. 4-2b, the full model is compared to the parabolic model at the exit plane. In the full model, the stokes pulse will continue to amplify until it is far from the gain line. There it propagates as a higher order soliton in the passive fiber (i.e. it lags behind the center due to the slower velocity of the red components in the anomalous dispersion regime. In the parabolic model, the stokes pulse is filtered out and the temporal pulse undergoes more pulse splitting than the numerical results indicate.

2) In fig. 4-3, the pulse spectra evolution is plotted as a function of propagation distance. We observe the formation of the red-shifted stokes pulse clearly. In fig. 4-4a, the spectrum of the full model is compared to the full model minus higher order terms at the exit plane as in fig. 4-2a. The Raman term is clearly responsible for the stokes pulse and the other effects cause small but non-negligible shifts in the stokes band. In fig. 4-2b, the spectrum calculated from the full model is compared to the parabolic gain dispersion model. The red-shifted spectra is not absorbed in the exact model as in the parabolic model and the resulting spectrum is not band limited. Therefore, self-frequency shift suppression due to gain dispersion is not a correct explanation in itself and is probably due to unavoidable losses in the system (along the fiber and coupling losses).

Figure Captions

Fig. 4-1 Evolution of the fundamental soliton propagating in a fiber amplifier.*Pulse parameters: τ=180 fs.. λ_0=1.55 μm. Δ = 0.

*Passive material parameters:$\Omega_R = 17.136$, $\Gamma_R = 17.46$,$n_2 = 10^{-21}$ (MKS); $\beta^{(2)} = -6 \times 10^{-26}\ s^2/m$; $\beta^{(3)} = 10^{-40}\ s^3/m$.

*Active material parameters: gain= 10 dB per dispersion length ; $T_1 = 10\ ms$; $T_2 = 60\ fs$.

Fig. 4-2 Signal profile at $\bar{z} = 2$ for the same pulse and materials parameters as fig.1. a.Effects of the passive fiber model: (i) full model; (ii) full model minus the $\beta^{(3)}$ term ; (iii) full model minus the Raman term; (iv) full model minus the self-steepening term.b.Effects of the gain model (i) full model; (ii) parabolic approximation model.

Fig. 4-3 The spectral distribution is plotted as a function of the frequency difference multiplied by the pulse duration (i.e., the normalized frequency difference) for the same pulse and materials parameters as fig.4-1.

Fig. 4-4 The spectral distribution is plotted as a function of the normalized frequency difference for $\bar{z} = 2$. a.The same parameters and labeling as those of fig. 4-2a are used. b.The same parameters and labeling as those of fig. 4-2b are used.

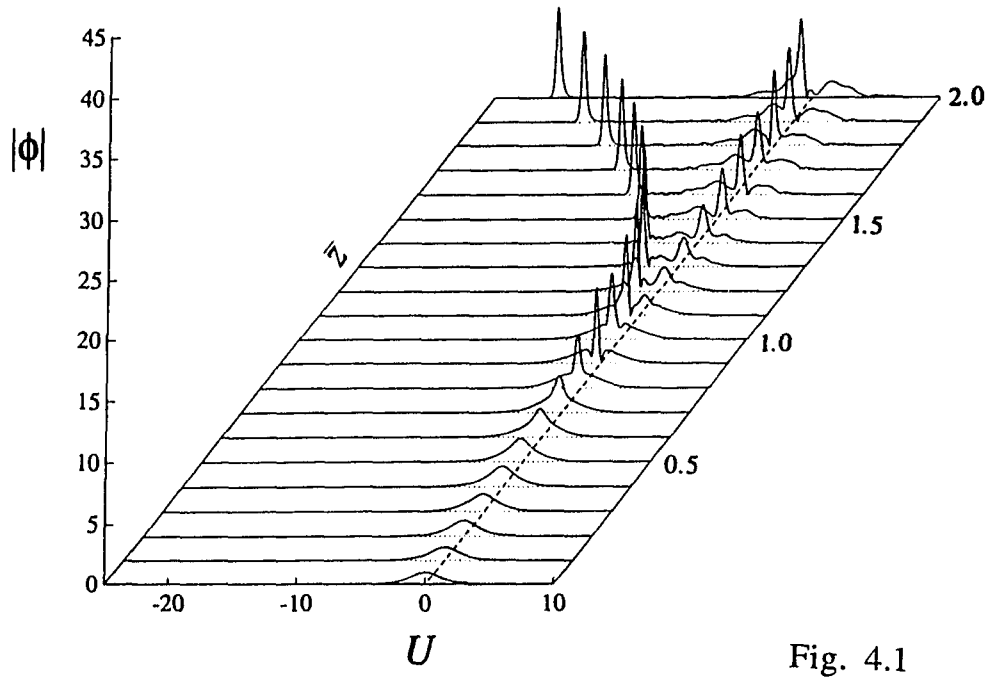

Fig. 4.1

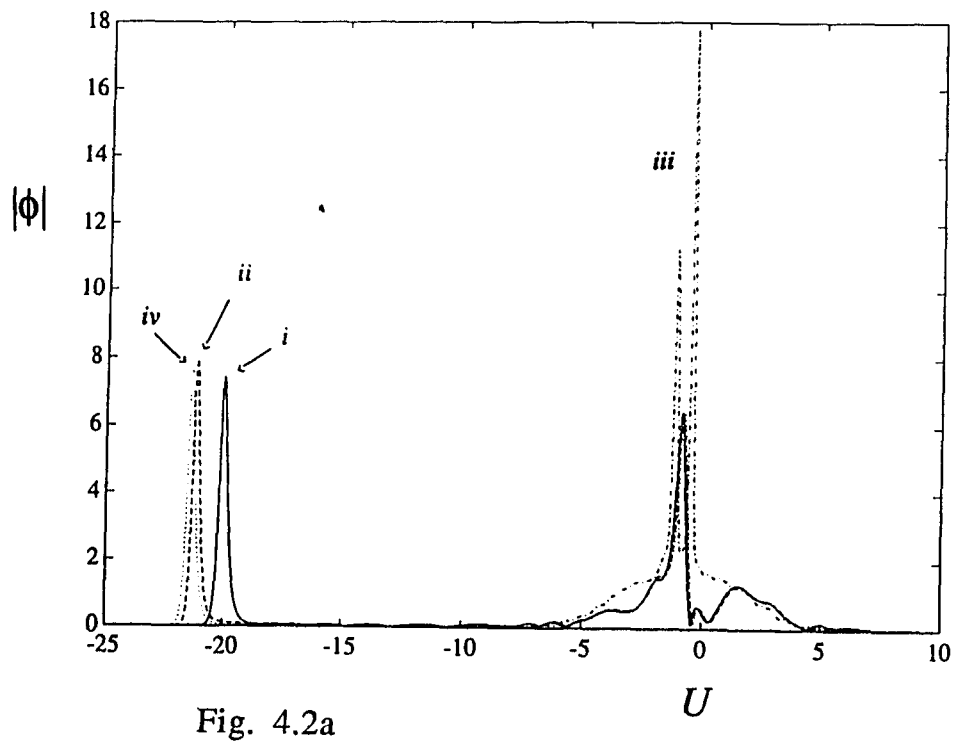

Fig. 4.2a

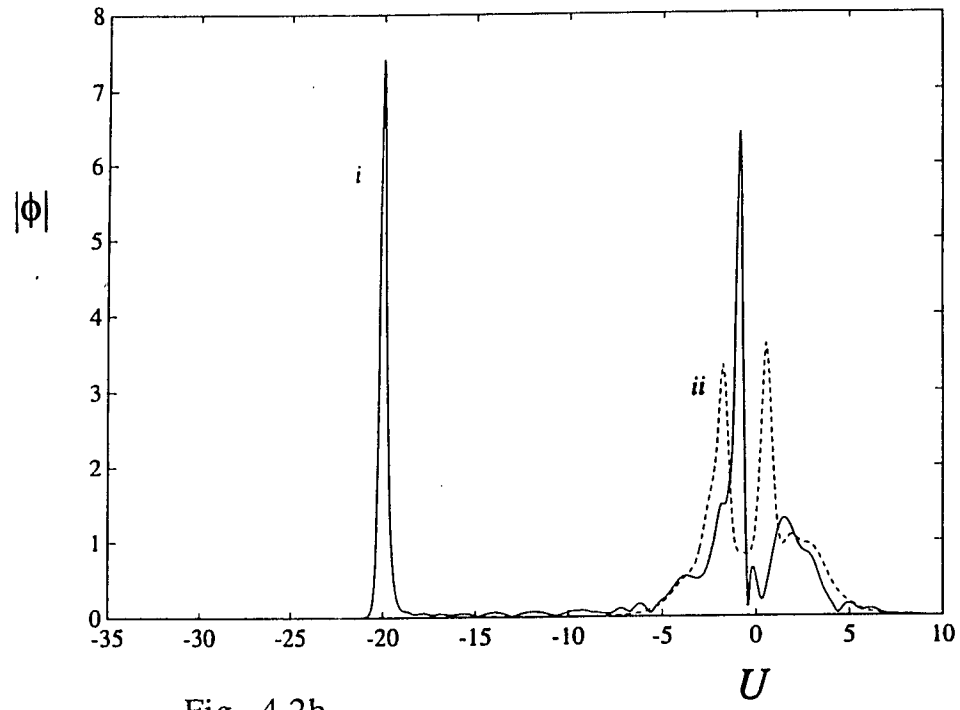

Fig. 4.2b

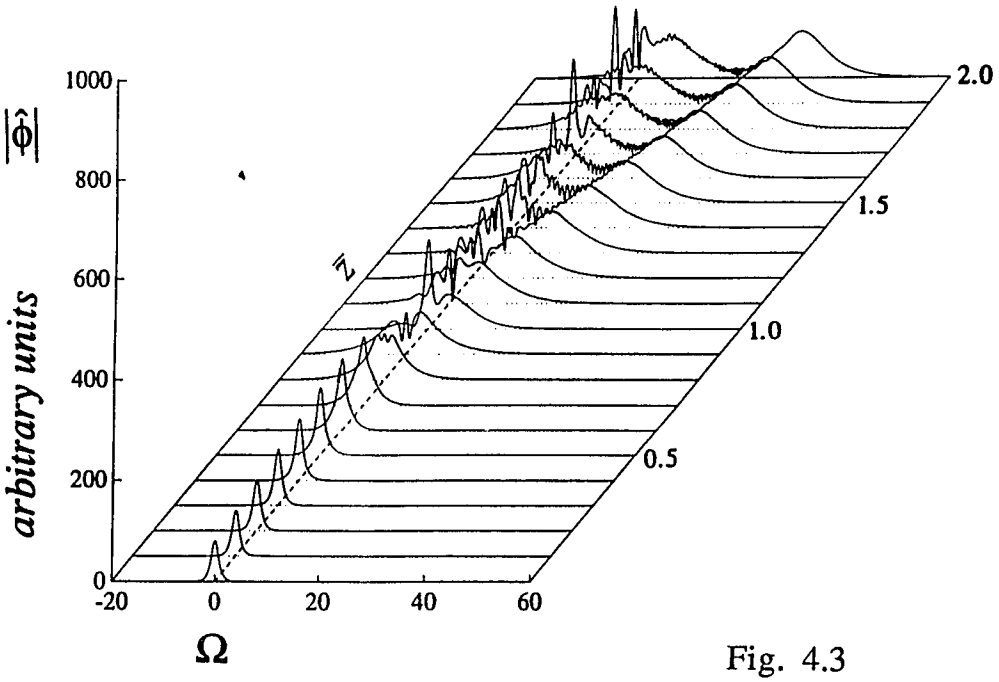

Fig. 4.3

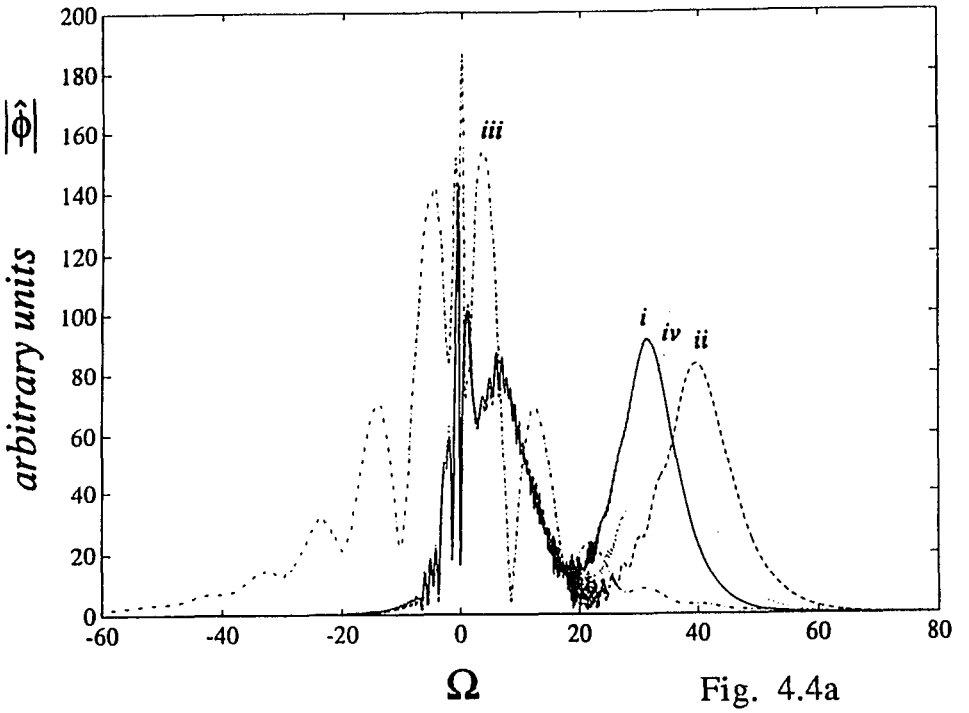

Fig. 4.4a

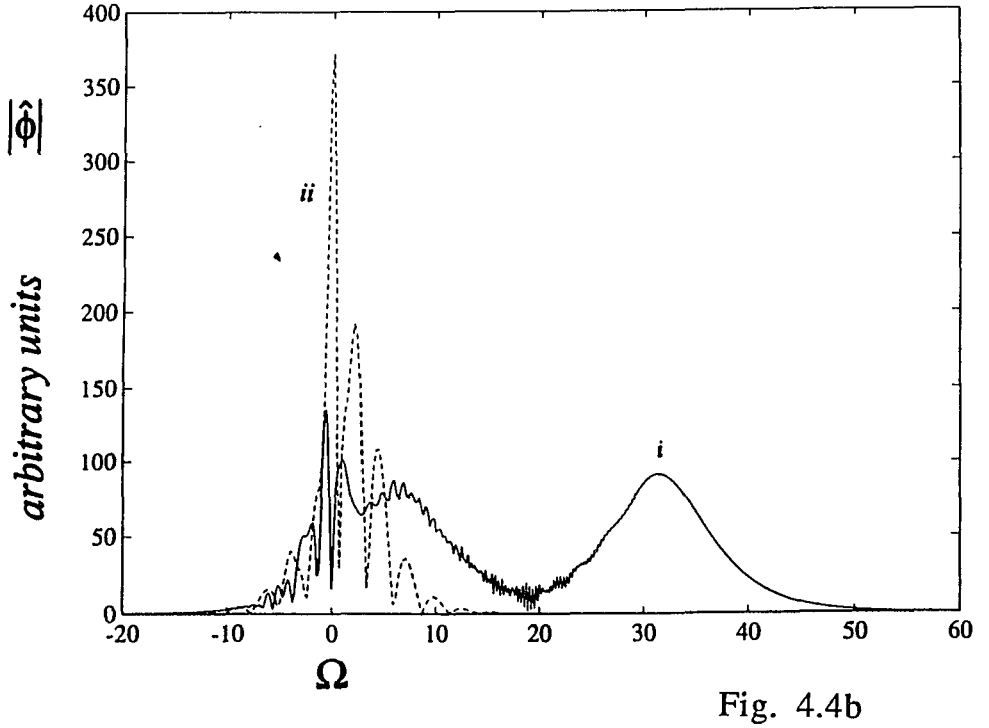

Fig. 4.4b

5.1) 2D C.W. Beam Propagation in Resonant Media (Model) [h]

The effect of an intensity dependant index of refraction on the propagation of a non-uniform monochromatic beam has led to both theoretical and numerical investigations [36-37]. In the simple Kerr medium, it was shown that the beam, for sufficient powers, will self-focus. In the 2-D limit, the existence of spatial solitons has been verified theoretically,numerically and experimentally [48-49]. When modelling the interaction of the light beam with material media, we showed that the proper framework is coupling the Maxwell equation with the Bloch equation. It is easy to see that far from resonance, the resulting equations will approximate the Kerr model. However, the true model gives rise to different phenomena not inherent in the Kerr model such as absorption and saturation in the nonlinear index of refraction. Therefore, the proper framework to study the propagation of intense monochromatic beams in material media is to solve the Bloch equations for the polarization which is a function of the field and use this as the source term in the Maxwell equation. This approach is taken in the study of both 2D and 3D beam propagation.

Maxwell equation for the propagation of a 2D c.w. beam in a resonant two-level medium is given, in the slowly varying envelope approximation by:

$$2ik_c E_0 \frac{\partial \phi}{\partial z} + E_0 \frac{\partial^2 \phi}{\partial x^2} = -\frac{\rho \omega_c^2 d}{\varepsilon v_g^2} \chi \qquad (5\text{-}1.1)$$

where z is the longitudinal coordinate, x is the transverse coordinate, $E = E_0\,\phi$, E_0 is the incoming electric field maximum amplitude, ρ is the two-level number density, $k_c = 2\pi / \lambda_c$, λ_c is the beam wavelength, d is the transition dipole moment, ε is the background permeability of the medium, v_g is the group velocity in the medium, and $\chi = p / d$ where p is the atomic polarization. In the Bloch model for the two-level system, the source polarization for a monochromatic beam can be obtained for given optical frequency by setting the time derivatives of the Bloch equations to zero and solving the resulting algebraic equations. This yields:

$$\chi = \frac{d\,T_2\,E_0\,\phi}{2\hbar}\left[\frac{(\Delta + i)}{\Delta^2 + 1 + s|\phi|^2}\right] n \qquad (5\text{-}1.2)$$

where $s = \left(d^2\,E_0^2\,T_1\,T_2\right)/\hbar^2$, $\Delta = \left(\omega_0 - \omega_c\right)T_2$, T_1 is the longitudinal relaxation time, T_2 is the transverse relaxation time, ω_0 is the angular frequency of the resonant transition, and n is the ratio of the population difference (number of atoms in the ground state - number of atoms in the excited state) divided by the total number of atoms. Since we are modelling the propagation through an initially unexcited system,n=1. In the small signal (Beer's Law) limit, the linear absorption coefficient of the two-level system at resonance is given in this notation by

$$g_0 = \frac{\rho k d^2 T_2 n}{4\hbar\varepsilon} \qquad (5\text{-}1.3)$$

Then the field equation becomes

$$\frac{\partial \phi}{\partial z} = \frac{i}{2k_c}\frac{\partial^2 \phi}{\partial x^2} + i g_0 \frac{(\Delta + i)}{\Delta^2 + 1 + s|\phi|^2}\ \phi \qquad (5\text{-}1.4)$$

To begin, we will concentrate first on the two-level model assuming that the source wavelength is located on the far-wing of the resonance line. For large detuning, the susceptibility can be expanded in the small parameter $\left[s/\left(\Delta^2 + 1\right)\right]$, and the Maxwell equation can be approximated to 3rd order terms in the field by

$$\frac{\partial \phi}{\partial z} = \frac{i}{2k_c}\frac{\partial^2 \phi}{\partial x^2} + i g_0 \frac{(\Delta + i)}{\Delta^2 + 1}\left[1 - \frac{s|\phi|^2}{\Delta^2 + 1}\right]\phi \qquad (5\text{-}1.5)$$

Comparing this equation to the standard form of Maxwell equation in a Kerr medium given by

$$\frac{\partial \phi}{\partial z} = \frac{i}{2k_c}\frac{\partial^2 \phi}{\partial x^2} + \frac{\alpha}{2}(i\Delta - 1)\phi + i\frac{n_2(1 + i/\Delta)\,|E_0|^2 k_c}{n_0}\,|\phi|^2\,\phi \qquad (5\text{-}1.6)$$

the values of α, the linear absorption coefficient, and n_2, the nonlinear Kerr coefficient, are respectively given by

$$\alpha = \frac{2g_0}{\Delta^2 + 1} \qquad (5\text{-}1.7a)$$

$$n_2 = -\frac{g_0\, n_0\, \Delta\, d^2\, T_1\, T_2}{\hbar^2\, k_c \left(\Delta^2 + 1\right)^2} \qquad (5\text{-}1.7b)$$

In our choice of parameters for the simulations, we observe that if the sample's length is of the order of the diffraction length $\left(z_d = k_c\, a^2\right)$, then (a) low total absorption translates into $\left[g_0\, z_d / \left(\Delta^2 + 1\right)\right] < 1$; (b) the validity of considering only the leading terms in the susceptibility perturbative expansion requires $\left[s / \left(\Delta^2 + 1\right)\right] << 1$; (c) the existence of a spatial soliton requires that the width and the amplitude be related such that $\left[g_0\, z_d\, |\Delta|\, s / \left(\Delta^2 + 1\right)^2\right] = 1$; and (d) neglecting the nonlinear absorption versus the nonlinear shift requires that $|\Delta| >> 1$.Since we are studying focusing behavior, Δ is negative (self-focusing medium).

5.2) 2D C.W. Beam Propagation in Resonant Media (Variational Approach) [h]

To get a qualitative feeling of the propagation phenomenon, we apply the variational model already applied to the case of the Kerr medium and extend it to a saturating (no loss) medium. This obviously will not give exact results due to aberrationless approximation in the trial functions as well as ignoring absorption effects. In analogy with the variational formulation in the Kerr medium we formulate the equations of motion for the beam parameters which are derived from the Euler-Lagrange equations of the Lagrangian density:

$$\mathrm{L} = \frac{i}{2}\left[\phi\frac{\partial\phi^*}{\partial\bar{z}} - \phi^*\frac{\partial\phi}{\partial\bar{z}}\right] + \frac{1}{2}\left(\frac{\partial\phi}{\partial\bar{x}}\right)^2 - \frac{\bar{g}_0\,\Delta}{s}\ln\left[1 + \frac{s}{\Delta^2+1}|\phi|^2\right]$$

The trial function used is (5-2.1)

$$\phi(\bar{x},\bar{z}) = A(\bar{z})\exp\left\{-\frac{1}{2}\frac{\bar{x}^2}{\varpi^2(\bar{z})} + i\frac{\rho\,(\bar{z})\,\bar{x}^2}{2}\right\} \qquad (5\text{-}2.2)$$

and the integrated lagrangian is

$$\mathbf{L} = \int d\bar{x}\,\mathrm{L} \qquad (5\text{-}2.3)$$

Following the previously outlined method, we obtain four equations for the given beam parameters. After doing the algebraic manipulations, we obtain the differential equation for the normalized beam radius.

$$\frac{d^2\varpi}{dz^2} = \frac{1}{\varpi^3} - \frac{2\bar{g}_0|\Delta|}{s\sqrt{\pi}} f_1\left(\frac{s}{\varpi\left(\Delta^2+1\right)}\right) + \frac{2\bar{g}_0|\Delta|}{\varpi\left(\Delta^2+1\right)\sqrt{\pi}} f_2\left(\frac{s}{\varpi\left(\Delta^2+1\right)}\right) \qquad (5\text{-}2.4)$$

and conservation of energy (in the lossless model) gives

$$|A(\bar{z})| = \frac{1}{\sqrt{\varpi(\bar{z})}} \qquad (5\text{-}2.5)$$

The curvature and longitudinal phase may be calculated along similar lines but is not necessary for our purposes. The auxiliary functions used are

$$f_1(x) = \int_{-\infty}^{\infty} du \log\left(1 + x\exp\left(-u^2\right)\right) \qquad (5\text{-}2.6a)$$

$$f_2(x) = \int_{-\infty}^{\infty} du \frac{\exp\left(-u^2\right)}{1 + x\exp\left(-u^2\right)} \qquad (5\text{-}2.6b)$$

These equations may be integrated using a combination of Runge-Kutta and numerical integration algorithms.

5.3) 2D C.W. Beam Propagation in Resonant Media (Numerical Results) [h]

In our simulations, we choose the beam initial shape to be a sech function, which is the invariant shape for a Kerr medium spatial soliton,

$$\phi(x, z=0) = \sec h\left(\frac{x}{a}\right) \qquad (5\text{-}3.1)$$

The numerical algorithm used combines F.F.T and an Adaptive Runge-Kutta scheme. The algorithm used is a simpler version than that in chapter 4 since the Bloch equations are simply algebraic. Therefore the comprehensive tests used there were sufficient. Also as a check, by choosing the medium parameters properly, we obtain the fundamental soliton with the absorption close to the value predicted by the linear absorption theory (since nonlinear absorption was chosen negligible).

The starting point in the parameter space which yields the fundamental spatial soliton with minimal absorption is

$\bar{g}_0 = 10^5, \Delta = -10^{3.5}, s = 10^{5.5}$ where $\bar{g}_0 = g_0 k_c a^2$

(The two-level atom number density corresponding to this case is $\rho = 2 \times 10^{18}\, m^{-3}$).

By scanning Δ over the parameter space, different propagation regimes are observed.

In fig. 5-1, the spatial profile at the exit plane for $\Delta = -10^4$ and $\Delta = -10^{3.5}$ is compared to the incident profile.

1) For larger values (~3 times) of the soliton detuning, the propagation is purely diffractive, since the Kerr coefficient is approximately 30 times smaller and therefore the effects of the non-linearity in the differential equation can be neglected.

2) For the soliton detuning, the total flux absorption over the length of the sample is less than 3% and the beam power corresponds to that of a fundamental spatial soliton at this value of the Kerr coefficient. The beam profile due to the small absorption is smaller than its value at the entrance plane , otherwise it follows closely the spatial soliton solution.

3) For a detuning value which is $\sqrt{10}$ smaller, the shape of the beam as it propagates in the resonant medium is markedly different. The multiple peaks in the beam profile that appears for small distances of propagation can be well understood by noting that the nonlinear Kerr coefficient is now 30 times larger which implies that the effective soliton number is about 6 times larger and the multipeak structure observed is akin to that of a higher order spatial soliton. To understand the origin of the break-up of the beam, we plot, in fig. 5-2 the spatial profile of the beam propagation if we had neglected the absorption term, and the results of the corresponding approximate nonlinear Schrodinger equation for the equivalent Kerr medium. The spatial variations of the phase (due to the nonlinear

beam and thus lead to the beam break-up. We note that the separation between the two daughter peaks as a function of the longitudinal distance is linearly increasing with z. Physically, the daughter pair pulses, located respectively on the positive and negative portions of the transverse axis acquire equal and opposite transverse velocities i.e. total momentum conservation.

4) In fig. 5-3, we plot the transverse beam profile as a function of propagation distance for smaller detunings (the detuning is now 10 times smaller). The shape of the beam, with the same initial conditions, as it propagates in the resonant medium undergoes periodic compression. In this instance, the parameter $\left[s/\left(1+\Delta^2\right)\right]\approx 3$ and the perturbative expansion used is not valid, i.e., the system can not be described as a Kerr medium. The system's susceptibility exhibits saturation effects for larger values of the field, resulting in larger absorption on the wings (i.e. lower fields) than at the center and thus leading to a narrowing of the beam. The beam main peak narrows at its minima to about 1/20 of its value at the entrance plane. The width of this peak oscillates with a period $\delta\bar{z}=0.052$. Other important features are: (i) the ratio of the secondary peak intensity to the main peak intensity decreases to less than 1%, and (ii) the location of the secondary peaks recede linearly from that of the beam center as the longitudinal distance increases.

5) In fig. 5-5, we plot the transverse beam profile as a function of propagation distance for even smaller detunings. As the detuning decreases, more secondary peaks develop, their relative intensity to the main peak decrease with the distance of propagation and their location recede from the center. In this regime, the beam is quasi-trapped with a breather central peak. The width of the central peak oscillates and is plotted in fig. 5-4 as a function of the longitudinal distance for the different detunings. The oscillations are in qualitative agreement with the variational approximation calculation. Since the fundamental peak behaves qualitatively like a soliton, oscillations in the width cause oscillations in the peak amplitude. The maximum amplitude of the central peak, in the quasi-trapped regime, is plotted in fig. 5-6 as function of the longitudinal distance. This quantity oscillates with the same period as the width but out-of-phase with it. Furthermore, the product of the $(\text{amplitude})^2$ by the width, approximately the flux, is slowly decaying due to the absorption in the medium. Although we are at small detunings, absorption is low as a result of the saturability of the model for high field intensities.

6) In fig. 5-7, the ratio of the amplitude square of the beam integrated over the transverse distance (i.e. total energy flux) over the same quantity evaluated at the entrance plane as a function of the normalized longitudinal distance of propagation for the different values of the detuning is plotted. We note that even for small detunings (which cause the absorption coefficient to increase), a significant percentage of the signal flux remains. We note that for the

smallest detuning considered, the transmission coefficient is about 10%. This should be compared with a value of $\exp\left(-3.6\times10^{4}\right)$ for the linear regime.

5.4) 3D C.W. Beam Propagation in Resonant Media (Model) [i]

The propagation of the 3D, unlike the 2D, spatial beam in a Kerr medium for sufficiently high power leads to self-focusing. In a more realistic model, however, the nonlinear index of refraction will saturate for high fields and absorption is present. Various theoretical models [75-79] have shown how such beams are quasi-trapped. In such a case, an infinite intensity will never exist. We investigate numerically the behavior of an axially symmetric 3D beam propagating through a resonant two level system. New qualitative features not exhibited in the Kerr model are exhibited and qualitative understanding of the numerical calculations are achieved by a semi-quantitative treatment using the variational [40] technique. In this geometry, we explore for large detuning the propagation of the beam as a function of the beam power and explore in particular the waveguiding properties that a resonant medium will exhibit.

The equation for the propagation of a 3D c.w. beam in a resonant two-level medium is given, in the slowly varying envelope approximation (SVEA), by:

$$2ik_c E_0 \frac{\partial \psi}{\partial z} + E_0\left(\frac{\partial^2 \psi}{\partial x^2} + \frac{\partial^2 \psi}{\partial y^2}\right) = -\frac{\rho \omega_c^2 d}{\varepsilon v_g^2}\chi \qquad (5\text{-}4.1)$$

where z is the longitudinal coordinate, x and y are the transverse coordinates, $E = E_0 \psi$, E_0 is the incoming electric field maximum amplitude, ρ is the two-level number density, $k_c = 2\pi / \lambda_c$, λ_c is the field wavelength, d is the transition dipole moment, ε is the

background permeability of the medium, v_g is the group velocity in the medium, and $\chi = p/d$ where p is the atomic polarizability. Using the same method applicable in 2D, χ is given by

$$\chi = \frac{d T_2 E_0 \psi}{2\hbar}\left[\frac{(\Delta + i)}{\Delta^2 + 1 + s|\psi|^2}\right] n \qquad (5\text{-}4.2)$$

where $s = \left(d^2 E_0^2 T_1 T_2\right)/\hbar^2$, $\Delta = (\omega_0 - \omega_c) T_2$, T_1 is the longitudinal relaxation time, T_2 is the transverse relaxation time, ω_0 is the angular frequency of the resonant transition, and n is the ratio of the population difference (number of atoms in the ground state - number of atoms in the excited state) divided by the total number of atoms, n is here assumed equal to one for an absorbing medium. The linear absorption coefficient of the two-level system at resonance is given in this notation by

$$g_0 = \frac{\rho k_c d^2 T_2 n}{4\hbar\varepsilon} \qquad (5\text{-}4.3)$$

and the field equation in this notation is

$$\frac{\partial\phi}{\partial z} = \frac{i}{2k_c}\left(\frac{\partial^2\phi}{\partial x^2} + \frac{\partial^2\phi}{\partial y^2}\right) + i g_0 \frac{(\Delta + i)}{\Delta^2 + 1 + s|\phi|^2}\ \phi \qquad (5\text{-}4.4)$$

The normalized distances:
$\bar{z} = z/k_c a_0^2$ and $(\bar{x}, \bar{y}) = (x/a_0, y/a_0)$ where a_0 is the initial beam size will be hence used.

5.5) 3D C.W. Beam Propagation in Resonant Media (Variational Scheme) [i]

Previous theoretical investigations of a 3D beam in a saturable absorber can treat the problem in an approximate way under various assumptions of detuning,field strength etc. Wagner et al.[75] used the aberrationless paraxial ray approximation, Leberre et al. [76-78] modeled the process in the high absorption regime by an initial encoding of the beam by the medium nonlinearity (i.e. neglecting diffraction) followed by a purely diffractive step (i.e. neglecting the nonlinearity), and McCord et al. [79] in a refinement to the initial encoding obtained approximate expressions for the position and magnitude of the main axis enhancement. In the variational approximation and for a laser frequency in the far-wing of the atomic line, absorption is totally neglected and Maxwell's equation can be derived from the Lagrangian density

$$L = \frac{i}{2}\left[\psi\frac{\partial\psi^*}{\partial\bar{z}} - \psi^*\frac{\partial\psi}{\partial\bar{z}}\right] + \frac{1}{2}\left[\left(\frac{\partial\psi}{\partial\bar{x}}\right)^2 + \left(\frac{\partial\psi}{\partial\bar{y}}\right)^2\right] - \frac{\bar{g}_0\,\Delta}{s}\ln\left[1+\frac{s}{\Delta^2+1}|\psi|^2\right] \qquad (5\text{-}5.1)$$

where $\bar{g}_0 = g_0\,k\,a_0^2$. We shall use for the trial function for the optimization procedure the parametrized aberrationless Gaussian form:

$$\psi(\bar{x},\bar{y},\bar{z}) = A(\bar{z})\ \exp\left\{-\frac{\left[\bar{x}^2+\bar{y}^2\right]}{2\varpi^2(\bar{z})}+\frac{i}{2}\,\rho(\bar{z})\left[\bar{x}^2+\bar{y}^2\right]\right\} \qquad (5\text{-}5.2)$$

the functions $|A|, \arg(A), \varpi, \text{and}\ \rho$ correspond respectively to the amplitude, longitudinal phase, normalized beam size and normalized radius of curvature. The ordinary differential equations of motion for these functions are obtained by a variational optimization over the integrated Lagrangian:

$$\mathbf{L} = \iint d\bar{x}\, d\bar{y}\, \mathrm{L} = \pi\frac{i\varpi^2}{2}\left[A\frac{dA^*}{d\bar{z}} - A^*\frac{dA}{d\bar{z}}\right] + \pi|A|^2\varpi^4\frac{db}{d\bar{z}} +$$

$$\frac{\pi\varpi^4|A|^2}{2}\left(\frac{1}{\varpi^4}+4b^2\right) + \frac{\pi\bar{g}_0\,\Delta}{s}\,\mathrm{Li}_2\left(-\frac{s\,|A|^2}{1+\Delta^2}\right) \qquad (5\text{-}5.3)$$

where Li_2 is the dilogarithm function, also known as Spence's integral. The self-focusing regime corresponds to $\Delta < 0$. The differential equation obeyed by ϖ in this regime is

$$\frac{d^2\varpi}{dz^2} = \frac{1}{\varpi^3} - \frac{2\bar{g}_0|\Delta|\varpi}{s}\left[\mathrm{Li}_1\left(-\frac{s}{\left(\Delta^2+1\right)\varpi^2}\right) - \mathrm{Li}_2\left(-\frac{s}{\left(\Delta^2+1\right)\varpi^2}\right)\right] \qquad (5\text{-}5.4)$$

Here Li_1 is the polylog function of order 1. For small s , this equation reduces to that obtained by the variational method for Kerr material,

$$\frac{d^2\varpi}{dz^2} + \frac{1}{\varpi^3}\left[\frac{\bar{g}_0 |\Delta| s}{2\left(\Delta^2 + 1\right)^2} - 1\right] = 0 \qquad (5\text{-}5.5)$$

Thus, in the variational method, the value for the critical self-focusing power for the Kerr material which approximates the saturable medium is:

$$s_{cr.} = \frac{2\left(\Delta^2 + 1\right)^2}{\bar{g}_0 |\Delta|} \qquad (5\text{-}5.6)$$

5.6) 3D C.W. Beam Propagation in Resonant Media (Numerical Results)

The numerical algorithm employs a combination of 2D F.F.T and Adaptive Runge-Kutta schemes. Since only the dimensionality in the transverse operator is different, the diffraction solution of the 3D beam was recovered. The active medium was checked in the previous problem.

In fig. 5-9, we plot for various input powers, the on axis field strength. We note:

1) For values of the saturation coefficient smaller than a critical value, the on-axis field decreases, albeit at a lower rate than that of a low energy beam, here the diffraction term is being partially compensated by the self-focusing term. We note as well that the waveguiding threshold increases with the addition of the nonlinear saturation.

2) For values of s larger than the critical focusing value, the saturable model contrary to the Kerr model would not lead to a catastrophic collapse of the amplitude, the on-axis field oscillates and the value of the oscillation period decreases with an increase in the beam power. With a further increase in power, the periodic evolution of the pulse becomes chaotic due to pulse splitting.

3) In fig. 5-10, we plot the transverse beam profile for various input powers as a function of propagation distance. As previously

3) In fig. 5-10, we plot the transverse beam profile for various input powers as a function of propagation distance. As previously known and as clearly shown by the figures the initial beam Gaussian shape is in general not preserved. We further note that the beam can periodically develop a hole in its center. In fig. 5-11, we investigate in more detail the hole formation evolution.

4) The waveguiding efficiency of a beam propagating in this medium is studied as a function of input power. In fig. 5-12, we plot as function of the longitudinal normalized distance the value of the capture efficiency of the beam through a circular aperture which captures 99% of the beam energy flux if located at the entrance plane. We note that the value of this efficiency is larger than 60% for all values of the beam power larger than the critical value and for any distance of propagation within the first ten diffraction lengths. Also note that the waveguiding efficiency increases markedly as the beam power increases. For comparison purposes, the capture efficiency of this aperture at 10 diffraction lengths for a weak beam is about 5%. The value of the waveguiding efficiency obtained for energetic beams clearly shows that despite the losses due to the absorption present when a beam is propagating in a resonant medium, the enhancement factor in the nonlinear index of refraction overcompensates and quasi-waveguiding becomes efficient.

5) In fig 5-13, the on-axis field as a function of the normalized propagation distance is compared to the variational approximation solution. As can be noted the approximate solution exhibits the main

qualitative features found in the exact solution, but quantitatively the results can differ by as much as 50% . For higher powers, the variational approach is useless due to the complex transverse profile of the beam exhibited (pulse splitting).

This scheme may prove useful in directed energetic beam propagation and in multi-signals parallel processing in optical computing.

Figures Captions

Fig. 5-1 The spatial profile of the beam is plotted as function of the normalized transverse coordinate.
$a = 300\mu ; T_1 = 10^{-9}\,\mathrm{s}, T_2 = 2\times 10^{-9}\,\mathrm{s}, g_0 = 10^5\, m^{-1}, s = 10^{11/2}, \lambda_c = 0.63\mu$

.

$\left|E_0^2\right| = 1.5\times 10^{11}(V/m)^2.$

i) $z = 2z_d$, $\Delta = -10^{7/2}$, ii) $z = 2z_d$, $\Delta = -10^4$, iii) z=0.

Fig. 5-2a The spatial profile of the beam is plotted as function of the normalized transverse coordinate and the normalized longitudinal coordinate for the same parameters as in fig.5-1(i) except that $\Delta = -10^3$.

Fig. 5-2b Same as 5-2a but neglecting absorption effects.

Fig. 5-2c Same as 5-2a but using the equivalent Kerr medium approximation.

Fig. 5-3 The spatial profile of the beam is plotted as function of the normalized transverse coordinate and the normalized longitudinal coordinate for the same parameters as in fig.5-1 except that $\Delta = -10^{5/2}$.

Fig. 5-4 The width of the central peak in fig. 5-3 is plotted as a function of the normalized longitudinal distance, in curve (i). Curves (ii, iii, iv, v) correspond respectively to $|\Delta| = \left(10^2, 10^{3/2}, 10, 10^{1/2}\right)$.

Fig. 5-5 The spatial profile of the beam is plotted as function of the normalized transverse coordinate and the normalized longitudinal coordinate for the same parameters as in fig.1 except that
a) $\Delta = -10^2$, b) $\Delta = -10^{3/2}$, c) $\Delta = -10$, d) $\Delta = -10^{1/2}$.

Fig. 5-6 The height of the central peak in the quasi-trapped regime is plotted as a function of the normalized longitudinal distance. Curves

(i, ii, iii, iv, v) correspond respectively to

$|\Delta| = \left(10^{5/2}, 10^{2}, 10^{3/2}, 10, 10^{1/2}\right)$.

Fig. 5-7 The ratio of the total flux over its value at the entrance plane as a function of the normalized distance for different values of the detuning.

i) $\Delta = -10^{4}$, ii) $\Delta = -10^{7/2}$, iii) $\Delta = -10^{3}$, iv) $\Delta = -10^{5/2}$, v) $\Delta = -10^{2}$, vi) $\Delta = -10^{3/2}$, vii) $\Delta = -10$, viii) $\Delta = -10^{1/2}$

Fig. 5-8 The height of the central peak in the quasi-trapped regime in the lossless variational approximation is plotted as a function of the normalized longitudinal distance. Curves (i, ii, iii, iv, v) correspond respectively to $|\Delta| = \left(10^{5/2}, 10^{2}, 10^{3/2}, 10, 10^{1/2}\right)$.

Fig.5-9 The field amplitude at $\bar{r} = 0$ is plotted as a function of the normalized longitudinal distance of propagation. The saturation coefficient s is measured in units of $s_{cr.} = \dfrac{2\left(\Delta^2 + 1\right)^2}{\bar{g}_0 |\Delta|}$, i.e. $s = \tilde{p} \times s_{crit.}$.

$T_1 = 10^{-9}$ s, $T_2 = 2 \times 10^{-9}$ s, $g_0 = 10^{5}\, m^{-1}$, $\lambda_c = 0.63\mu$, $\Delta = -10^{7/2}$.

(i) free propagation, (ii) $\tilde{p}$=1, (iii) $\tilde{p}$=2, (iv) $\tilde{p}$=3.

Fig.5-10 The field amplitude is plotted as a function of the normalized longitudinal distance of propagation and of the normalized radius.
$T_1 = 10^{-9}\,\mathrm{s}$, $T_2 = 2\times10^{-9}\,\mathrm{s}$, $g_0 = 10^5\,m^{-1}$, $\lambda_c = 0.63\mu$, $\Delta = -10^{7/2}$
a) $\tilde{p}$=1 , **b)** $\tilde{p}$=2 , **c)** $\tilde{p}$=3 , **d)** $\tilde{p}$=10 , **e)** $\tilde{p}$=100 , **f)** $\tilde{p}$=1000.

Fig.5-11 Zoom view of fig. 5-10f around a region where the beam develops a hole at its center.

Fig.5-12 The flux , through the circular aperture with 99% transmission at the entrance plane, is plotted as a function of the normalized longitudinal distance of propagation.
$T_1 = 10^{-9}\,\mathrm{s}$, $T_2 = 2\times10^{-9}\,\mathrm{s}$, $g_0 = 10^5\,m^{-1}$, $\lambda_c = 0.63\mu$, $\Delta = -10^{7/2}$
(i) free propagation, (ii) $\tilde{p}$=1, (iii) $\tilde{p}$=2, (iv) $\tilde{p}$=100, (v) $\tilde{p}$=1000.

Fig.5-13 Comparison of the exact numerical results with the variational method approximation results for the field amplitude at $\bar{r} = 0$ as a function of the normalized longitudinal distance of propagation.
(i) exact numerical results. (ii) variational method results.
a) $\tilde{p}$=1 , **b)** $\tilde{p}$=2 , **c)** $\tilde{p}$=3 , **d)** $\tilde{p}$=4.

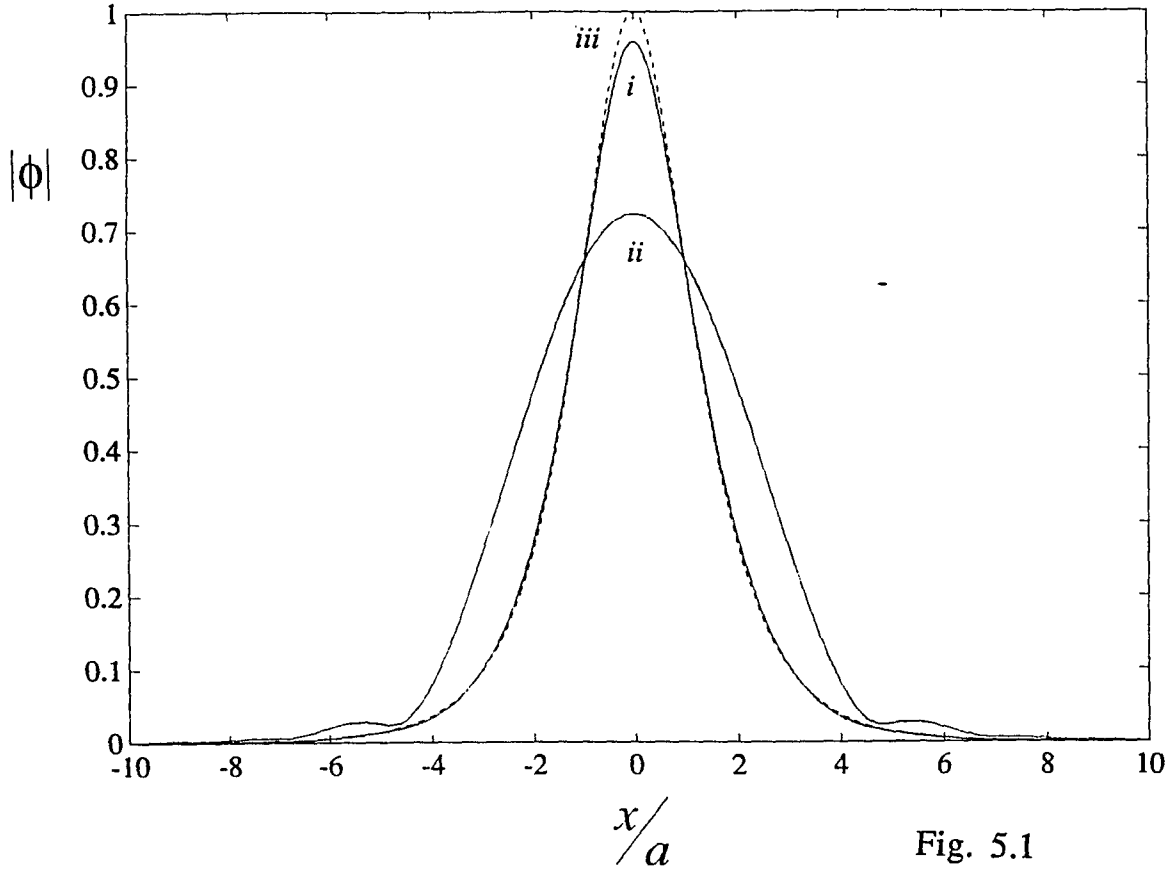

Fig. 5.1

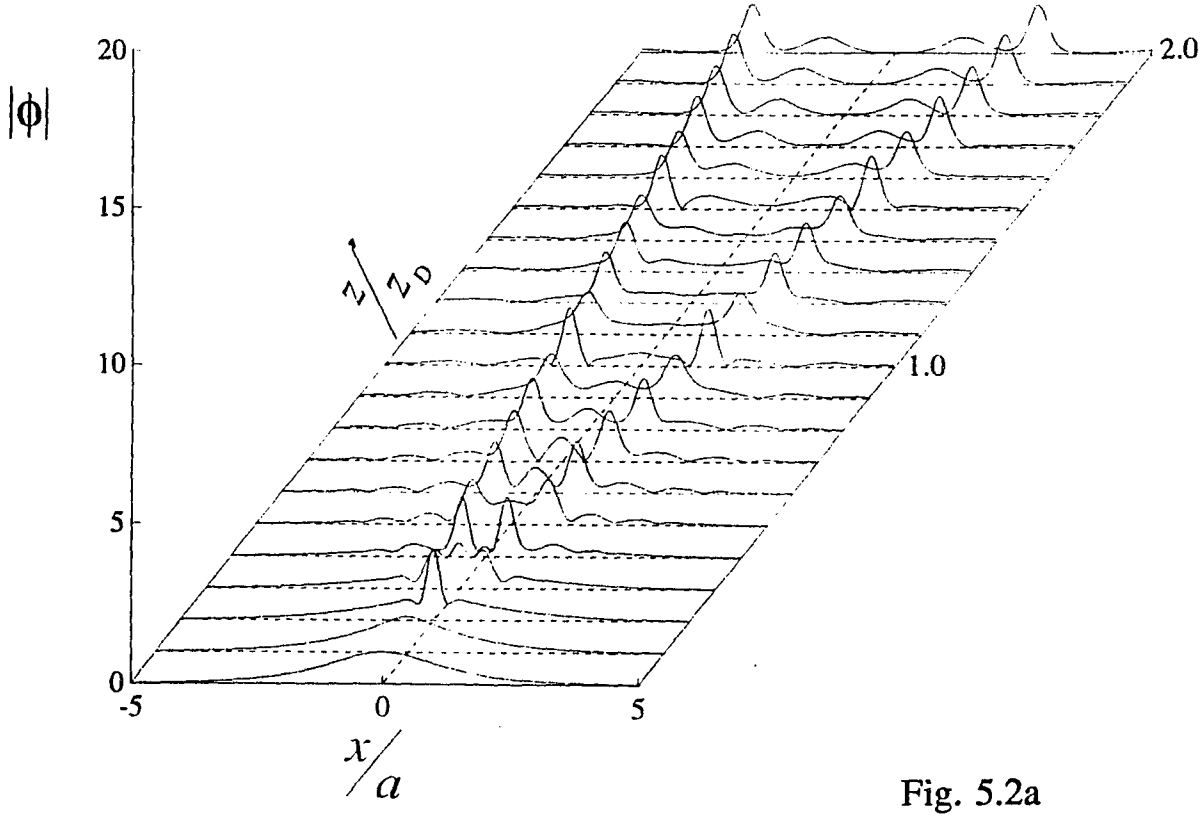

Fig. 5.2a

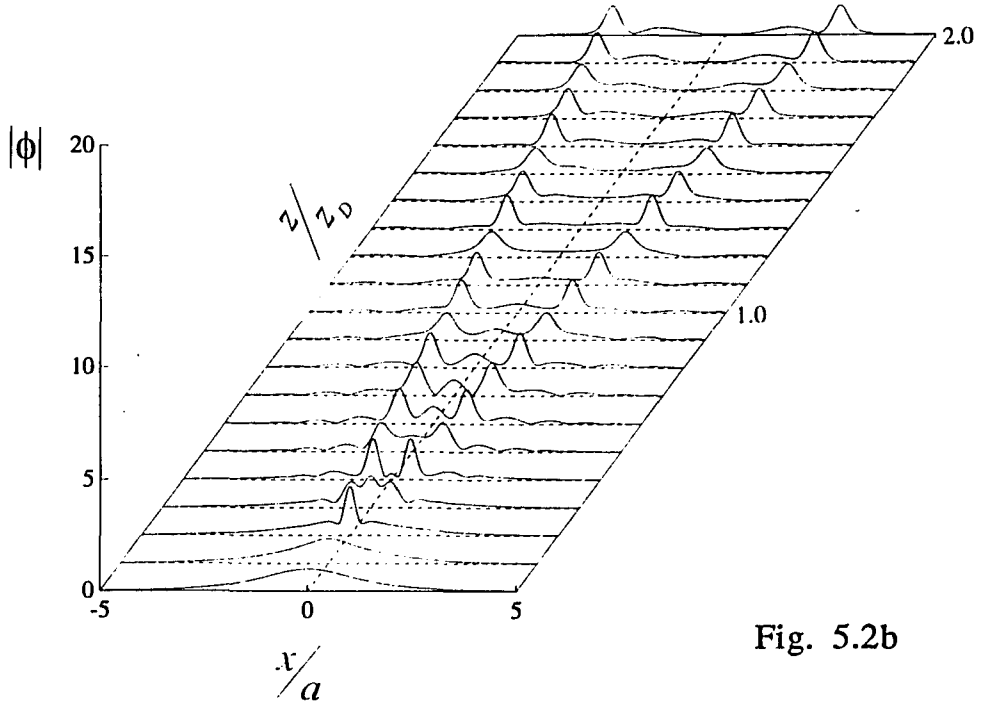

Fig. 5.2b

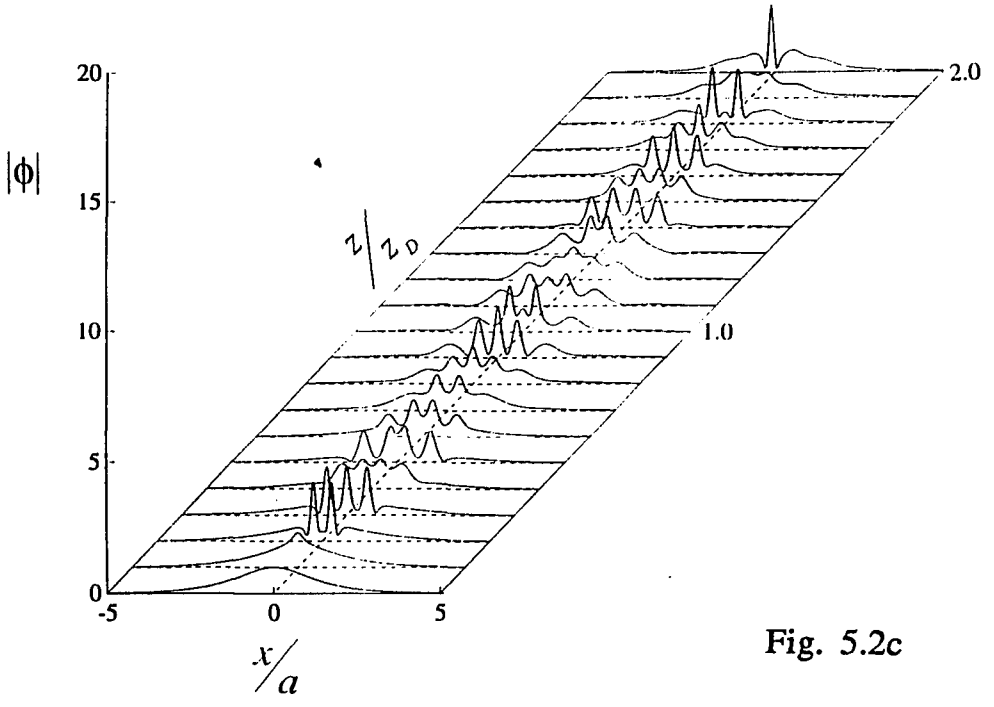

Fig. 5.2c

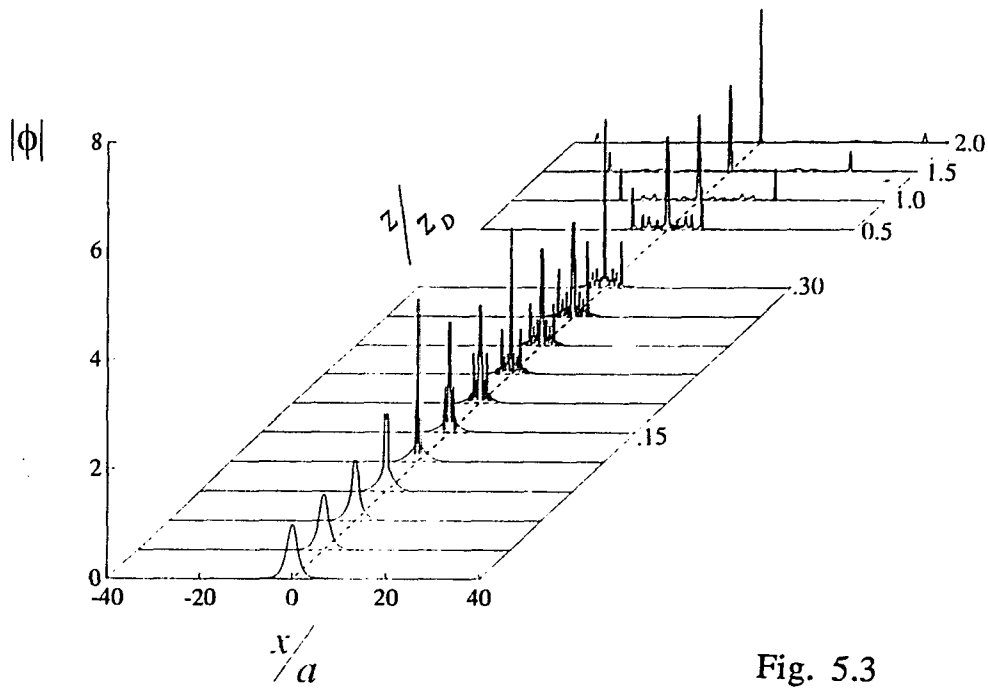
|φ|
8
6
4
2
0
-40
-20
0
20
40
x/a
z/z0
2.0
1.5
1.0
0.5
.30
.15

Fig. 5.3

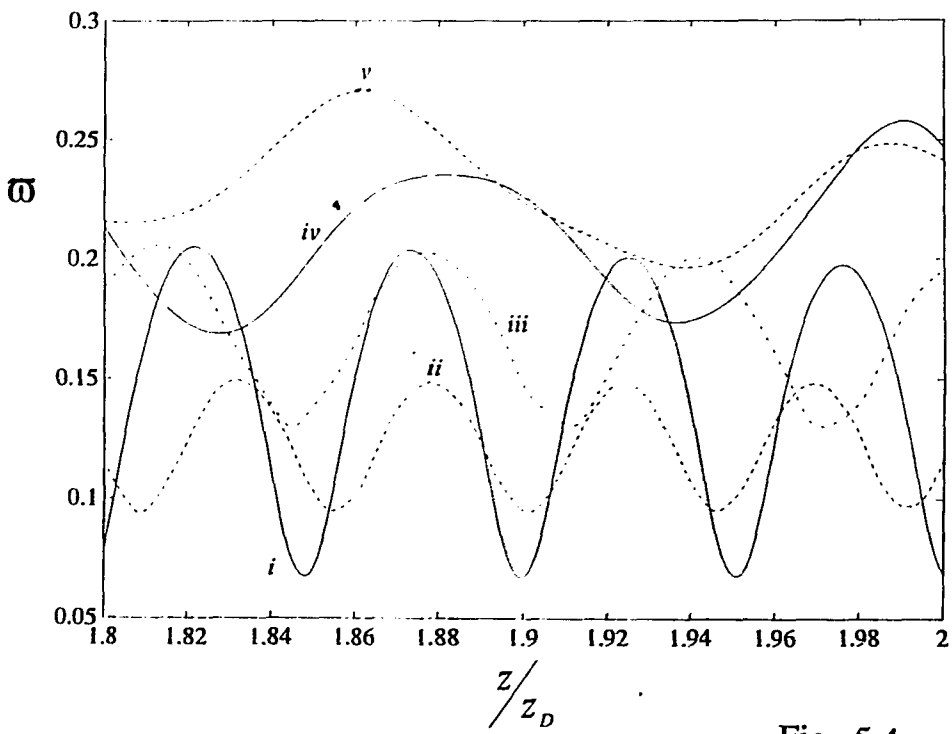
ϖ
0.3
0.25
0.2
0.15
0.1
0.05
1.8
1.82
1.84
1.86
1.88
1.9
1.92
1.94
1.96
1.98
2
z/z_D
v
iv
iii
ii
i

Fig. 5.4

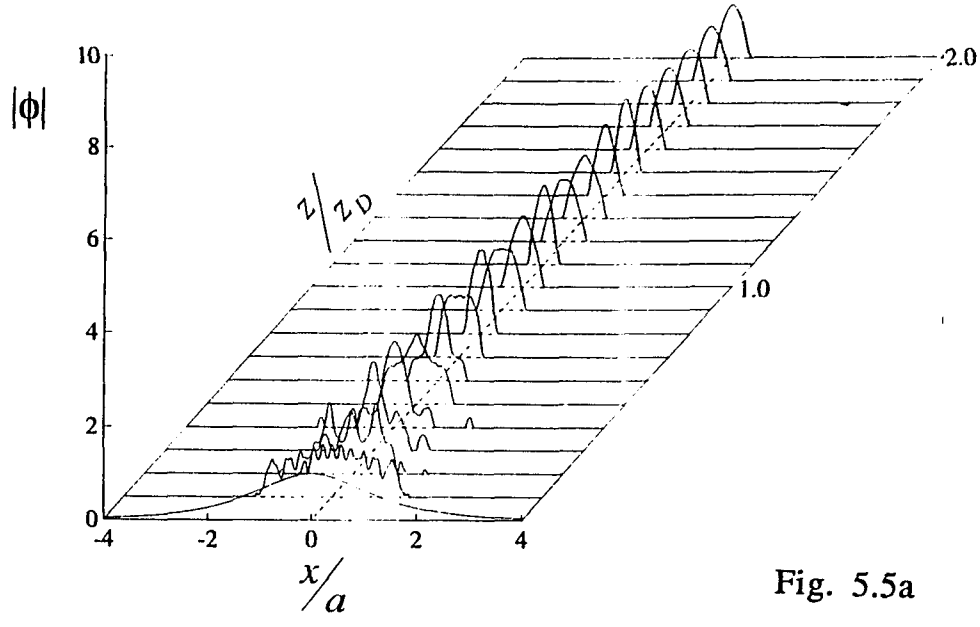

Fig. 5.5a

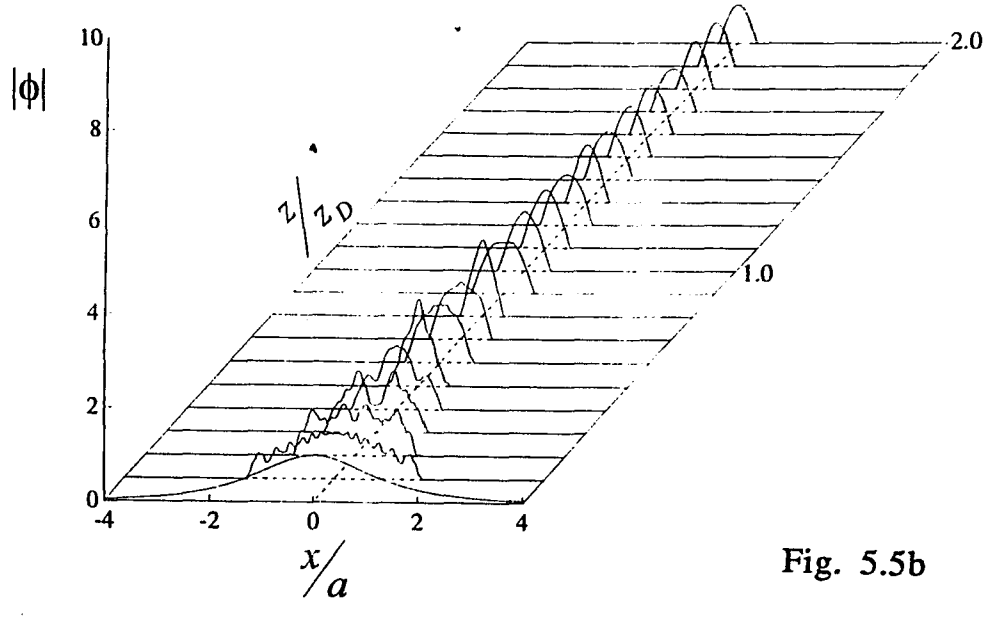

Fig. 5.5b

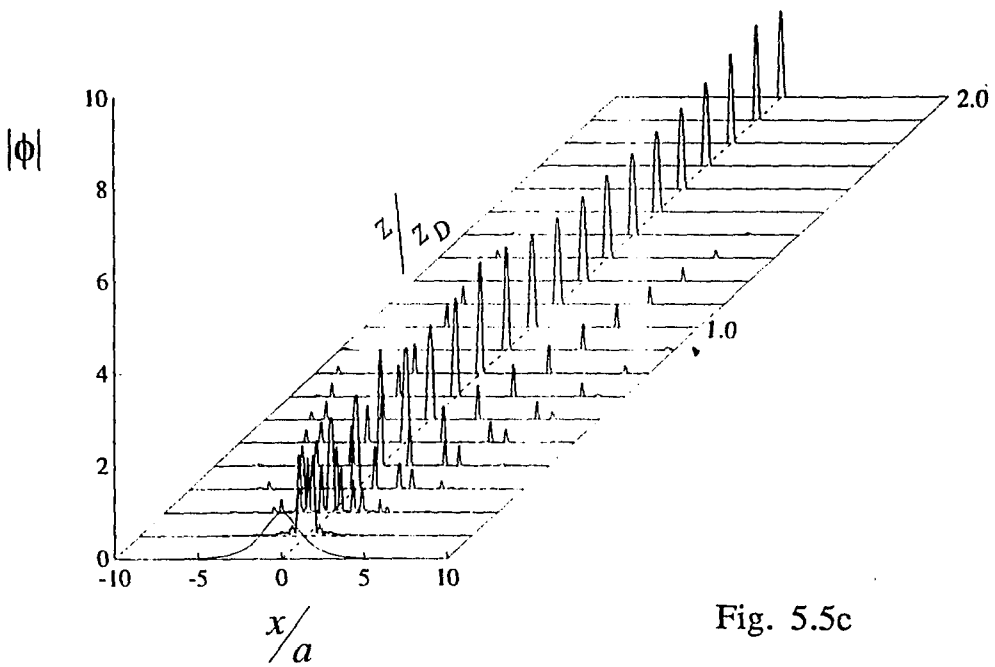

Fig. 5.5c

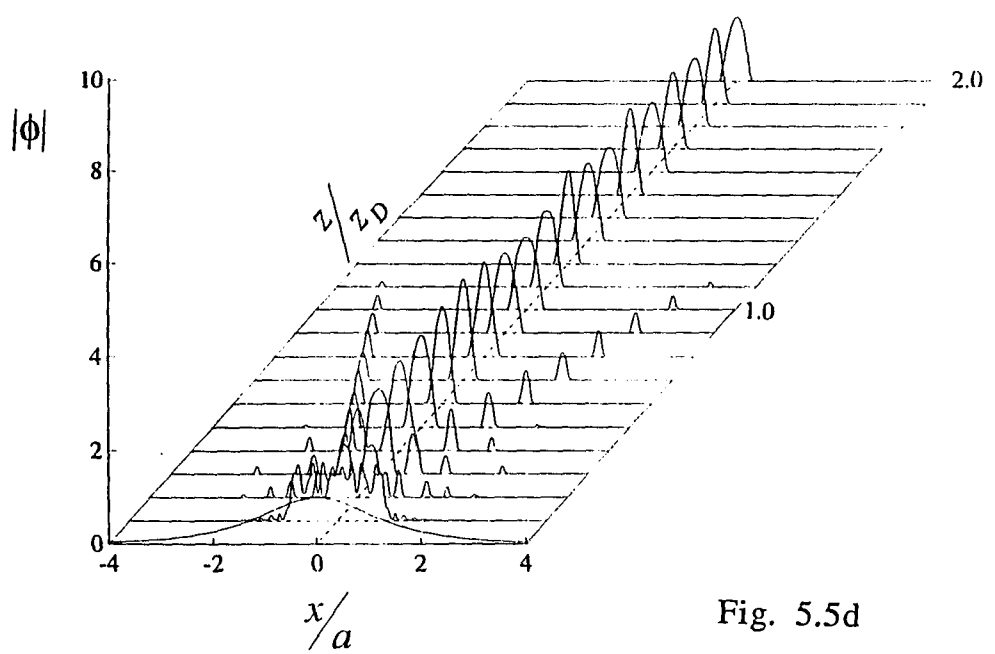

Fig. 5.5d

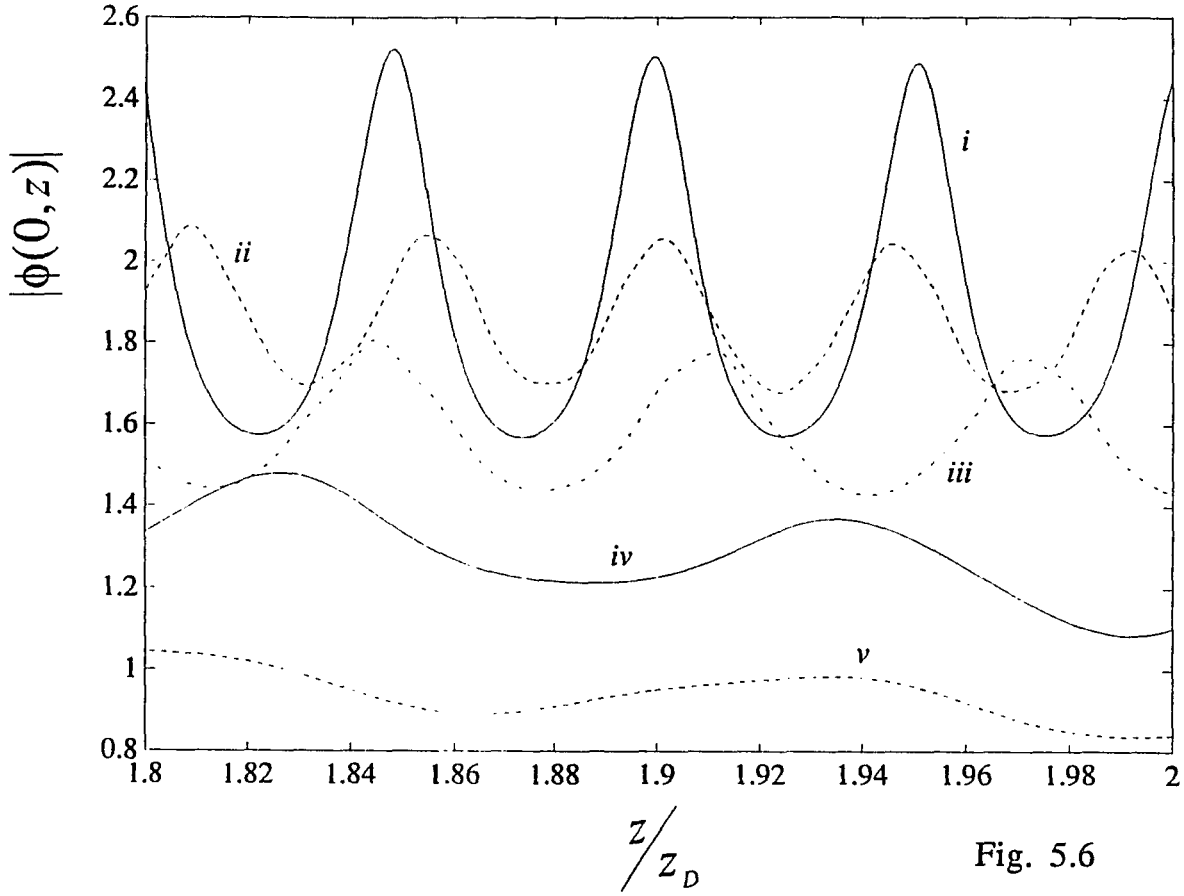
$|\phi(0,z)|$
2.6
2.4
2.2
2
1.8
1.6
1.4
1.2
1
0.8
1.8
1.82
1.84
1.86
1.88
1.9
1.92
1.94
1.96
1.98
2
i
ii
iii
iv
v
z/z_D

Fig. 5.6

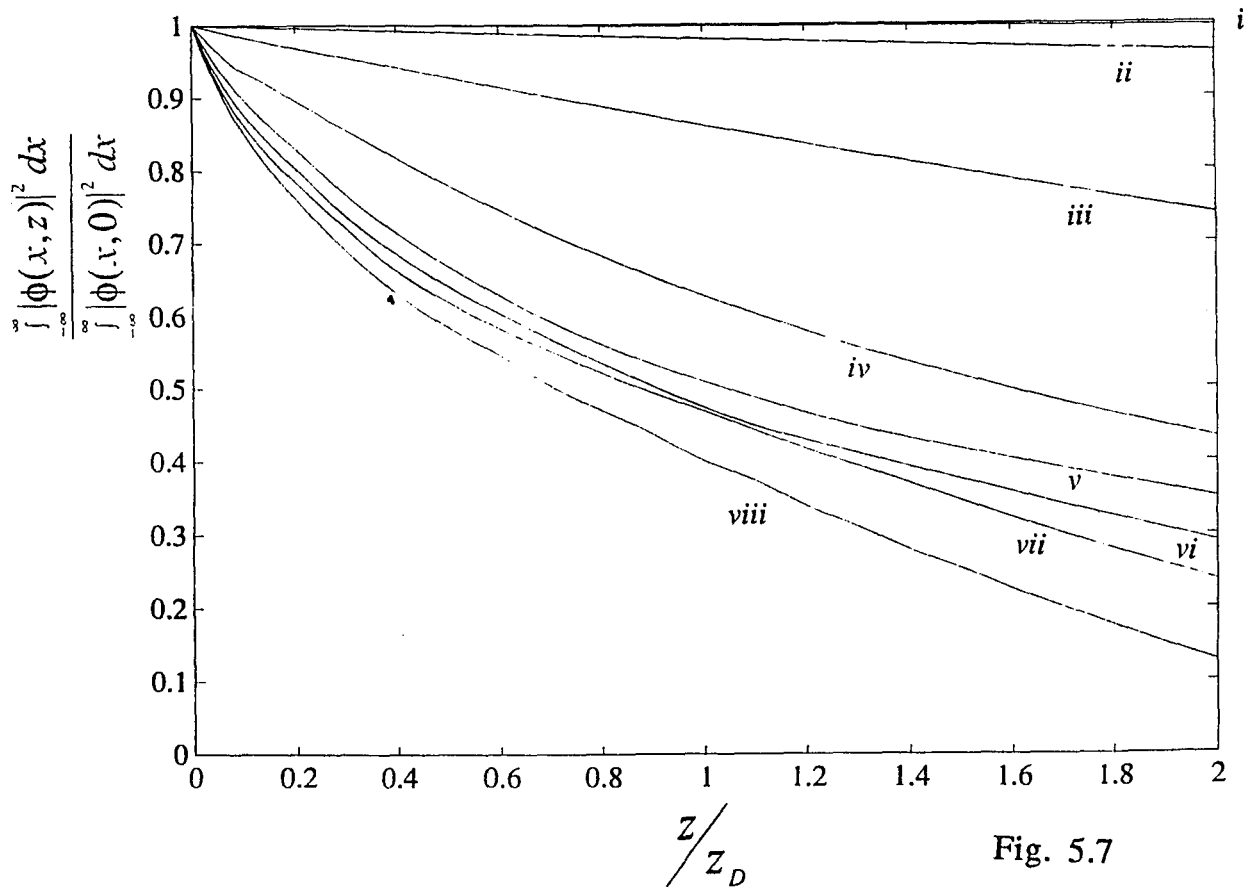
$\frac{\int_{-\infty}^{\infty}|\phi(x,z)|^2\,dx}{\int_{-\infty}^{\infty}|\phi(x,0)|^2\,dx}$
1
0.9
0.8
0.7
0.6
0.5
0.4
0.3
0.2
0.1
0
0
0.2
0.4
0.6
0.8
1
1.2
1.4
1.6
1.8
2
i
ii
iii
iv
v
vi
vii
viii
z/z_D

Fig. 5.7

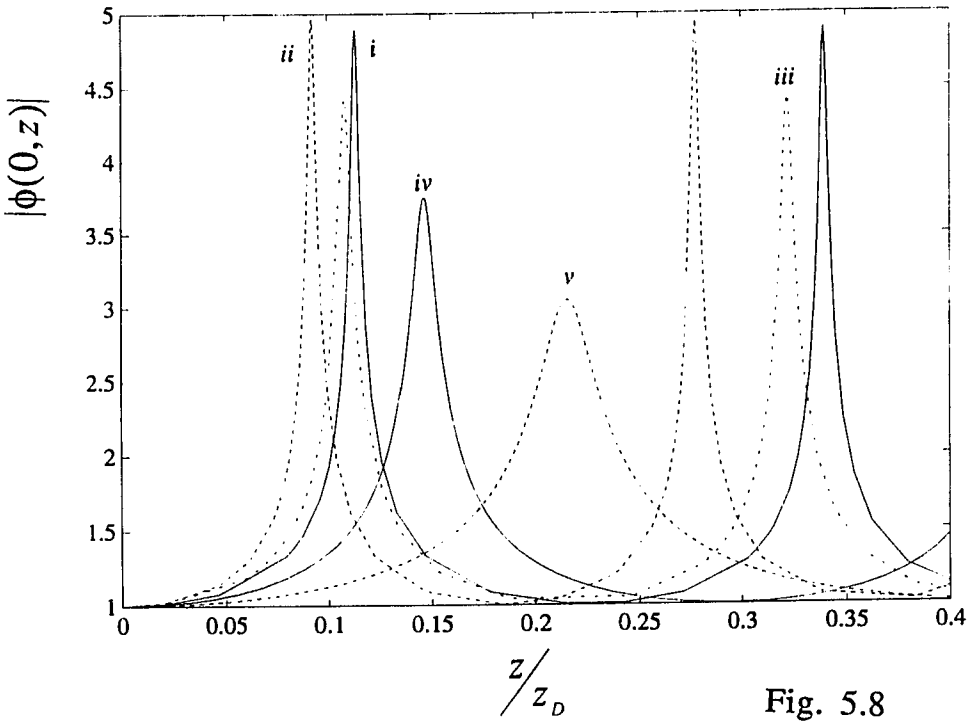
|φ(0,z)|
ii
i
iii
iv
v
5
4.5
4
3.5
3
2.5
2
1.5
1
0
0.05
0.1
0.15
0.2
0.25
0.3
0.35
0.4
z/z_D

Fig. 5.8

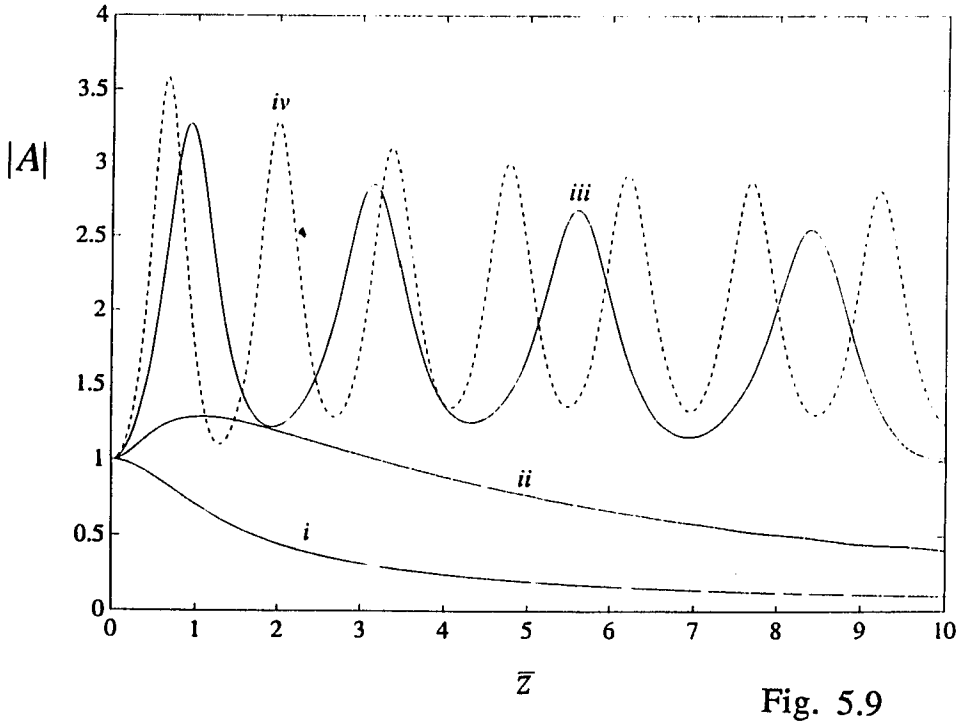
|A|
iv
iii
ii
i
4
3.5
3
2.5
2
1.5
1
0.5
0
0
1
2
3
4
5
6
7
8
9
10
z̄

Fig. 5.9

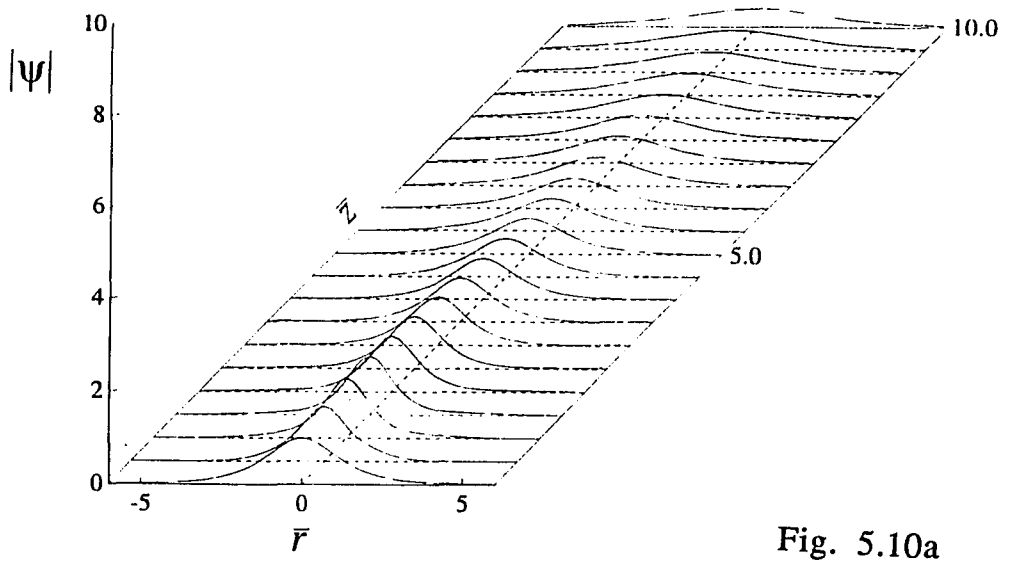

Fig. 5.10a

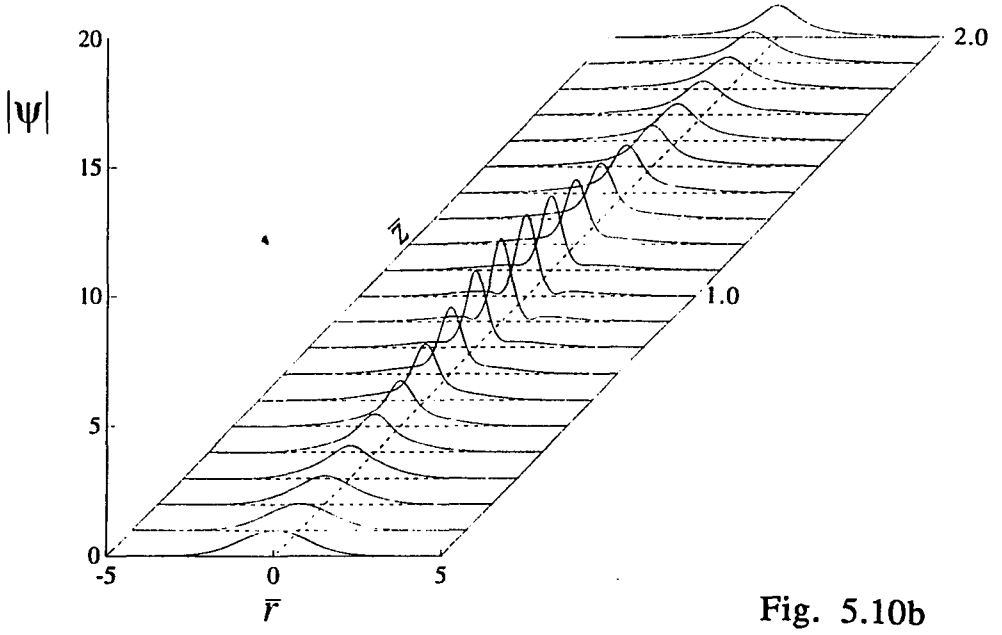

Fig. 5.10b

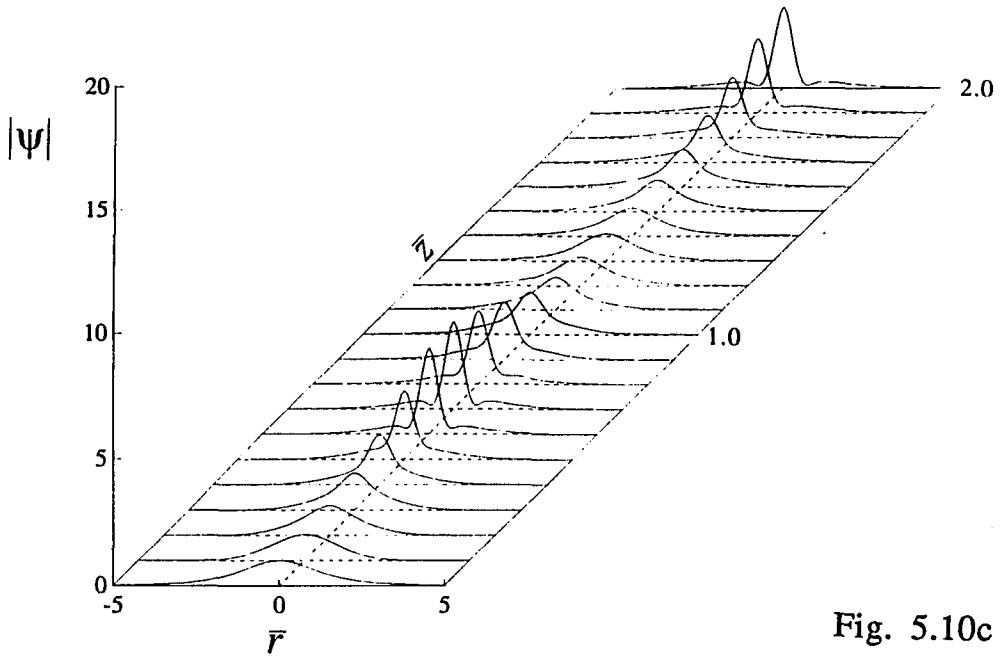

Fig. 5.10c

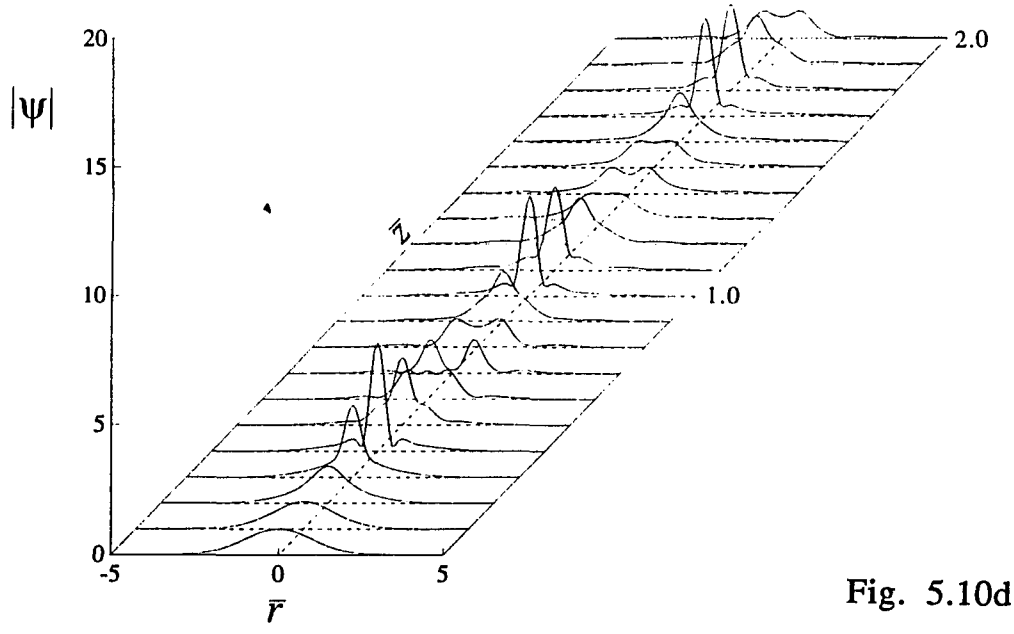

Fig. 5.10d

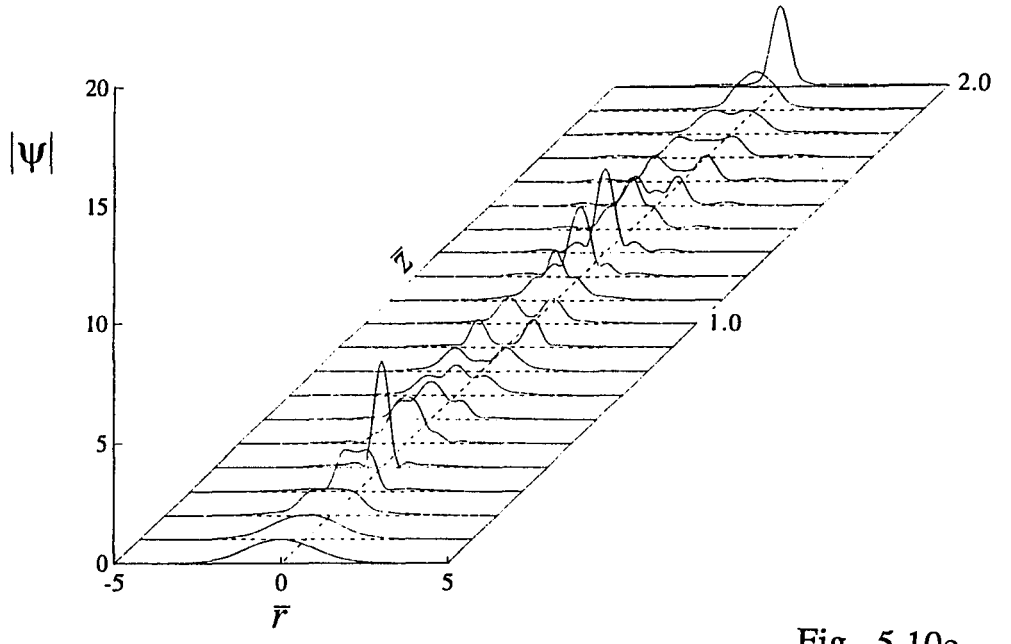

Fig. 5.10e

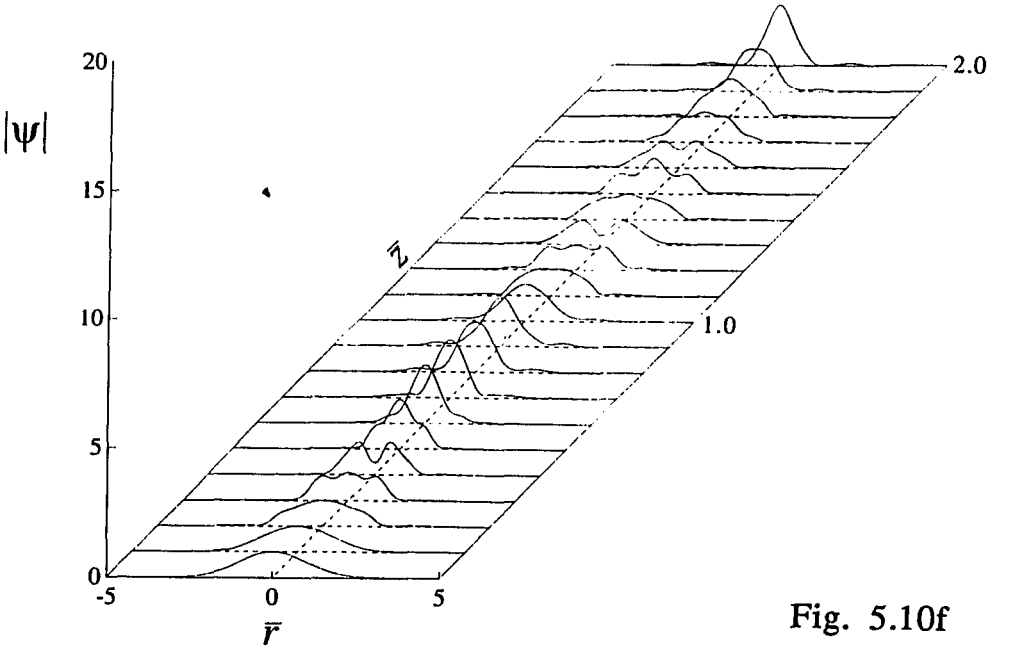

Fig. 5.10f

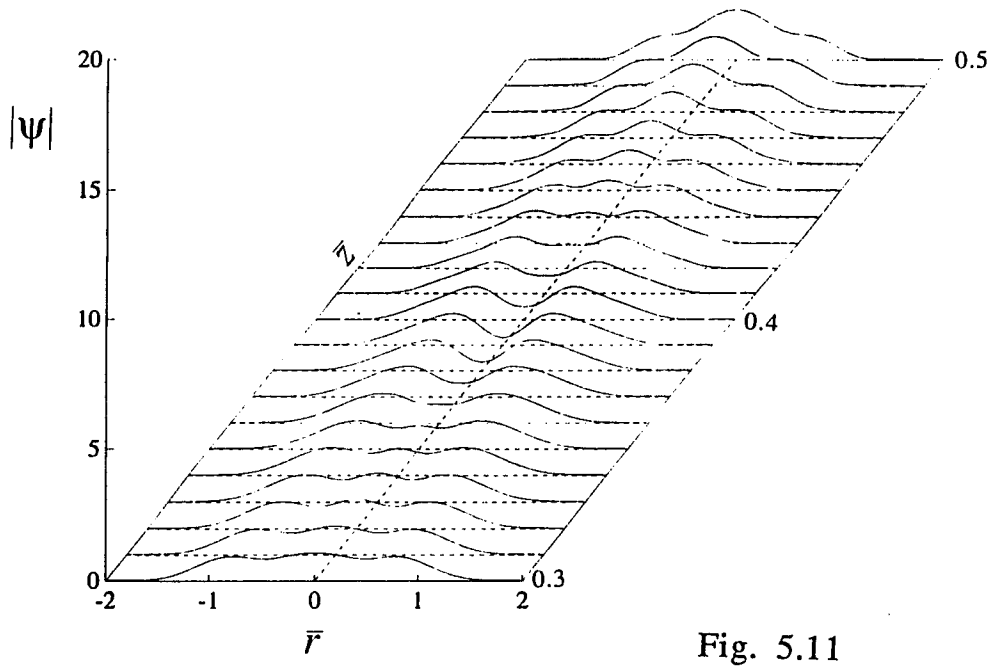

Fig. 5.11

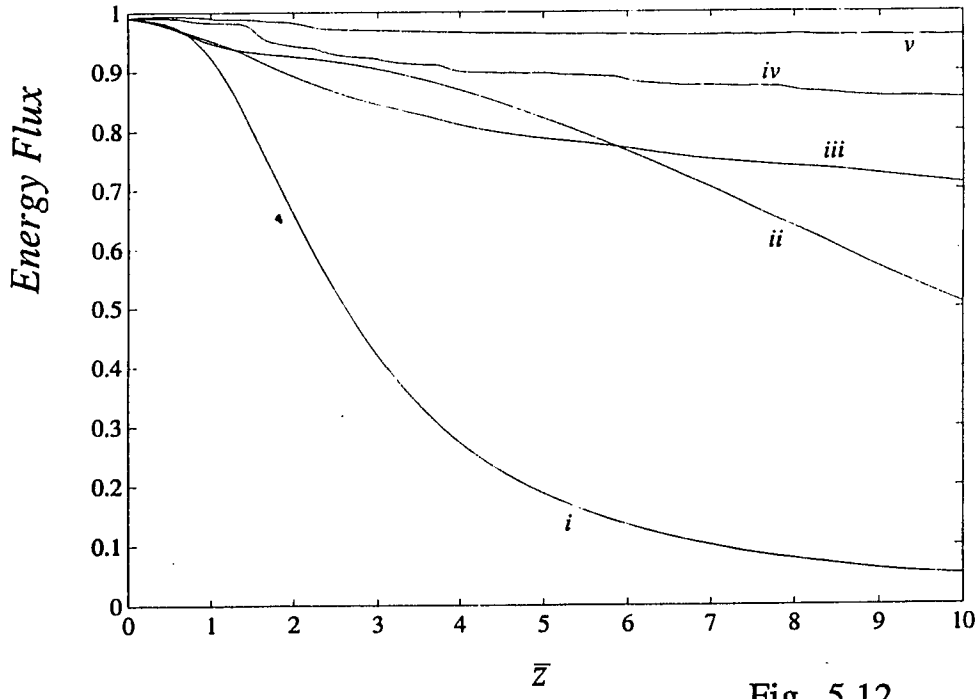

Fig. 5.12

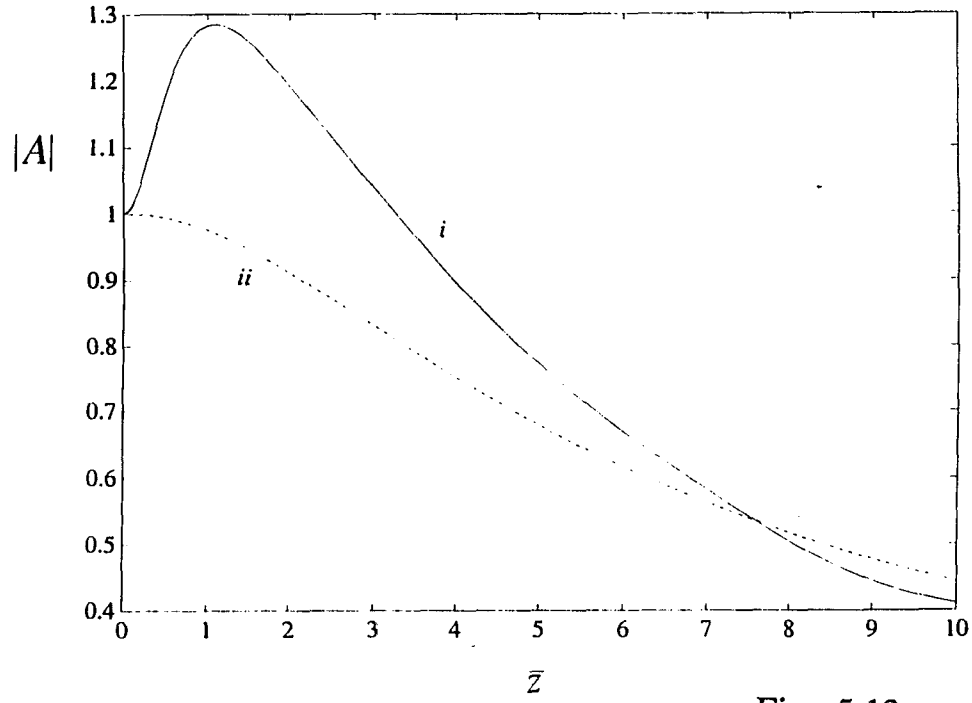

Fig. 5.13a

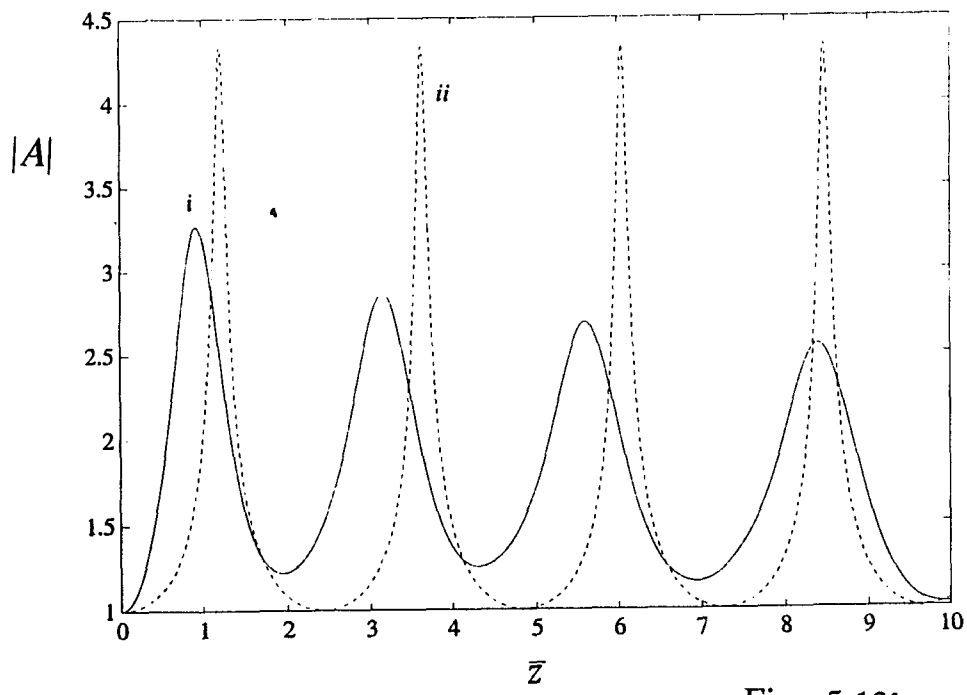

Fig. 5.13b

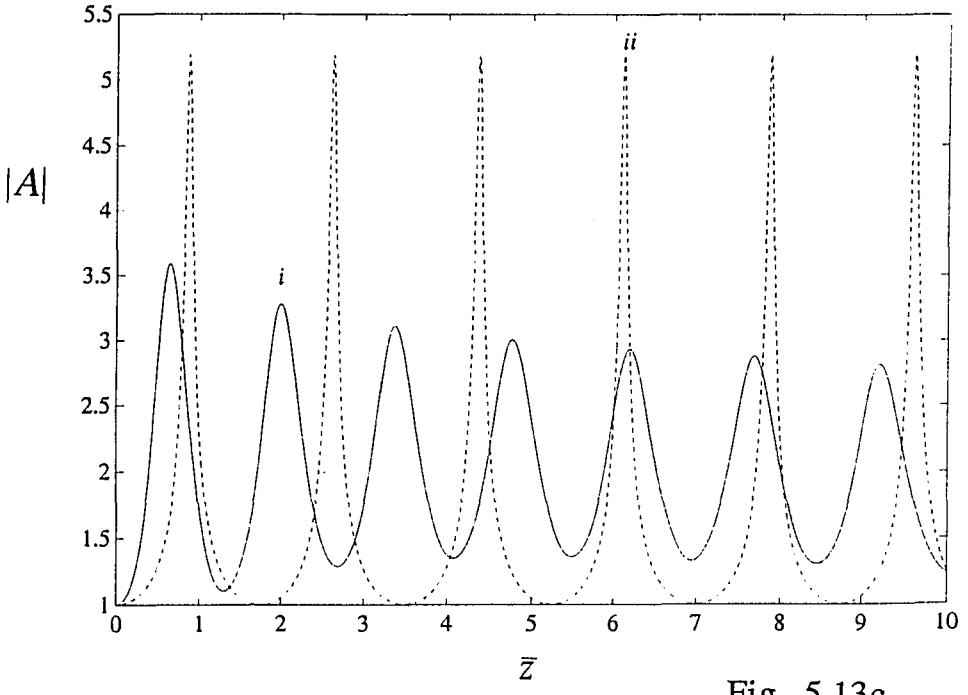

Fig. 5.13c

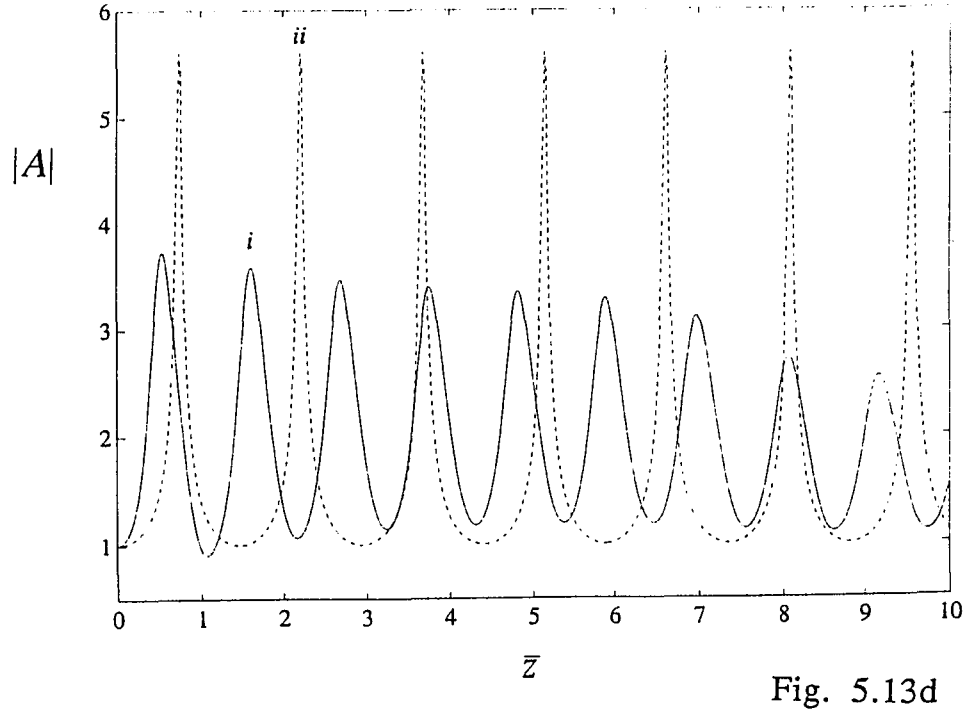

Fig. 5.13d

6.1) Incoherent Signals (Coherence Time Compression) [c]

The study of relaxation processes in material media occupy a central role in ultra-fast spectroscopy. The need to resolve processes on the femto-second scale requires extremely short coherent pulses since it is the pulse duration which sets the limit on the resolution of the experiment.

In 1984, seminal experiments by Beach and Hartmann [80], Asaka et al.[81], and Morita and Yajima [82] showed that the temporal duration of pulses can be irrelevant for short time resolution experiments. What matters is that the field coherence time be short(i.e. wide spectral bandwidth). Long pulses with short coherence times are called incoherent. Correlation times as short as 15 fsec. have been achieved simply by using Nd-Yag lasers to pump dyes and then using the amplified spontaneous emission (ASE) for excitation pulses. A further bandwidth increase in an already incoherent pulse was proven theoretically possible [83] through the self-phase modulation of an incoherent pulse obtained through its propagation in a Kerr medium such as an optical fibre. This self-phase induced spectral broadening ,and corresponding coherence time shortening of incoherent pulses propagating in single mode optical fibers was recently observed by de Araujo, da Cruz and Gouveia-Neto [84]. Both the previous theoretical and experimental results were restricted to regimes where the Kerr medium can to a very good approximation be assumed dispersionless. However, as we have shown, for femtosecond pulses, the effects of group velocity dispersion, self steepening, and Induced Raman Scattering can not be neglected. Consequently in the quest for incoherent pulses with a coherence

time of the order of only few femtoseconds we investigate numerically the propagation of an incoherent pulse in an optical fibre with none of the previously mentioned effects neglected. The general model used requires a numerical solution.

To numerically model the propagation of a noisy signal in a nonlinear Kerr medium, we need to construct the initial ensemble of states with given statistics and a specific form for the correlation function, propagate each state of said ensemble independently, and then obtain from the ensemble of final states the new correlation function as function of the medium and signal parameters. We will consider only Gaussian complex fields [85].

If we define the normalized Fourier transform of the electric field envelope $\mathbf{F}[\phi(U,V)]$ as $\tilde{\phi}(\mathbf{\Omega},V)$ then, including self-phase modulation (SPM), self-steepening (SS), induced Raman scattering (IRS), group velocity dispersion (GVD) and higher order group velocity dispersion (HGVD), the differential equation for $\tilde{\phi}$ is given by:

$$\frac{\partial \tilde{\phi}(\Omega,V)}{\partial V} = \frac{i\,\varepsilon\,K}{2}\left(1-\frac{\Omega}{K}\right)\mathbf{F}\left[|\phi(U,V)|^2\,\phi(U,V)\right] + \frac{i\,\varepsilon\,K}{2}\mathbf{F}\left\{\phi(U,V)\mathbf{F}^{-1}\left[\chi_R(\Omega)\mathbf{F}\left[|\phi(U,V)|^2\right]\right]\right\} + i\left(v_g T_c\right)\left[\frac{\beta^{(2)}\,\Omega^2}{2\,T_c^2}-\frac{\beta^{(3)}\,\Omega^3}{6\,T_c^3}\right]\tilde{\phi}(\Omega,V) \qquad (6\text{-}1.1)$$

where $E = E_0\,\phi$, $\varepsilon = \dfrac{n_2|E_0|^2}{n_0}$, $V = \dfrac{z}{v_g\,T_c}$, $U = \dfrac{z}{v_g\,T_c} - \dfrac{t}{T_c}$,

T_C is the initial coherence time, v_g is the group velocity at the pulse center frequency, n_0 is the linear index of refraction, n_2 is the Kerr nonlinear index of refraction including geometric factors resulting from the transverse averaging of the mode over the fibre cross-section, E_0 is the amplitude of the electric field, $K = \omega_0 T_c$, ω_0 is the center frequency, $\Omega = (\omega_0 - \omega) T_c$, χ_R is the Raman susceptibility and $\beta^{(k)}$ is the k^{th} derivative of the propagation constant with respect to the angular frequency evaluated at the signal center frequency.

The Raman susceptibility is approximated by:

$$\chi_R(\Omega) = \frac{\chi_0 (\Omega_R \Gamma_R)}{\Omega_R^2 - \Omega^2 + i \Gamma_R \Omega} \qquad (6\text{-}1.2)$$

where -i χ_0 is the value of the susceptibility at $\Omega = \Omega_R$, Ω_R is the Raman shift normalized to the coherence time i.e molecular vibrational frequency multiplied by T_C and Γ_R is the normalized phenomological line width. Since the minimum coherence time is expected to decrease as a function of the input field intensity, we work in the normal dispersive regime where the required energetic pulse sources exist.

We shall assume that the electric field envelope initial auto-correlation function to have a Gaussian form

$$\left| K\left(\frac{T}{T_c}, V=0\right) \right| = E_0^2 \left\langle \phi^*\left(U + \frac{T}{T_c}, V=0\right) \phi(U, V=0) \right\rangle$$

$$= E_0^2 f = E_0^2 \exp\left(-\frac{T^2}{T_c^2}\right) \qquad (6\text{-}1.3)$$

where, using the Ergodic theorem, the time averaging can be replaced by an ensemble average and the < > represents such averaging. The main features of complex gaussian fields are that the ensemble average of the product of an odd number of them is zero while the ensemble average of a product consisting of n fields and n conjugate fields is the sum over all permutations of the products of the n paired contractions of one of the fields and one of the conjugate fields, specifically if the two point correlation function is known

$$\left\langle A^*(t_1,0)\,A(t_2,0)\right\rangle = E_0^2\, f(t_2-t_1) \tag{6-1.4}$$

then the n point correlation function is

$$\left\langle A^*(t_1,0)\,A^*(t_2,0)\ldots A^*(t_n,0)A(t_{n+1},0)\,A(t_{n+2},0)\ldots A(t_{2n},0)\right\rangle =$$

$$E_0^{2n}\sum_P f(t_j-t_i)\,f(t_k-t_l)\ldots..\,f(t_p-t_q) \tag{6-1.5}$$

where the subscript of the first variable in the argument of $f \in \{n+1,\ldots..,2n\}$, the subscript of the second variable in the argument of $f \in \{1,\ldots..,n\}$ and all integers from 1 to $2n$ appears only once in each term of the sum . P refers to all permutations of the indices and f is the form function of the second order (or two-point) correlation function.

Now we review the basic algorithms [86] for constructing this ensemble at V=0, and for deducing from the propagated ensemble at an arbitrary V the corresponding field auto-correlation function. We define the process by the matrix $\phi(V)$, its row index (denoted by a

greek letter) specifies the element of the ensemble and its column index (denoted by a latin index) specifies the normalized discretized time.

To construct the initial incoherent signal, start by generating an uncorrelated matrix $\phi^0(V=0)$, such that the elements of each of its column are representatives of a complex random variable with uncorrelated components and such that each component (the real and imaginary parts) has zero mean and unit variance. Let the dimension of this matrix be $L \times M$. Next, construct the Toeplitz matrix, a square matrix with both latin indices and such that

$$\mathbf{T}_{ij} = \exp\left[-\frac{(j-i)^2}{p^2}\right] \tag{6-1.6}$$

where p is the number of sampling points in an initial coherence time, and where i and j go from 0 to (M -1) in integer increments. Next, [87] make a Cholesky decomposition of **T**, i.e find the lower triangular matrix **X** (making **X** lower triangular insures a unique factorization) such that $\mathbf{T} = \mathbf{X}\,\mathbf{X}^{\mathrm{T}}$, where the superscript T attached to a matrix denotes the transpose matrix. The matrix $\phi(V=0)$ is then $\phi^0(0)\,\mathbf{X}^T$. To show that this matrix possesses the desired correlation function, we have

$$\begin{aligned}\left\langle \phi^T(V=0)\phi(V=0)\right\rangle &= \left\langle \mathbf{X}\left(\phi^0\right)^T \phi^0 \mathbf{X}^T \right\rangle \\ &= \mathbf{X}\left\langle \left(\phi^0\right)^T \phi^0 \right\rangle \mathbf{X}^T \\ &= \mathbf{X}\mathbf{I}\mathbf{X}^T = \mathbf{T}\end{aligned} \tag{6-1.7}$$

which by construction of T has the desired correlation function. The matrix $\phi(V)$ is obtained from $\phi(V=0)$ by propagating each row (ensemble element) via the fiber equation. Once obtained, then the correlation matrix **R** is

$$\mathbf{R}_{ij}(V)=\frac{\sum_{\mu=1}^{L}\phi_{\mu i}^{*}(V)\,\phi_{\mu j}(V)}{\left[\sum_{\mu=1}^{L}\phi_{\mu i}^{*}(V)\,\phi_{\mu i}(V)\right]^{1/2}\left[\sum_{\mu=1}^{L}\phi_{\mu j}^{*}(V)\,\phi_{\mu j}(V)\right]^{1/2}} \tag{6-1.8}$$

and the field auto-correlation function at the discretized positive time m is

$$K_m(V)=E_0^2\exp(-i\,\omega_0\,T)\sum_{i=0}^{M-m-1}\frac{\mathbf{R}_{i,m+i}(V)}{M-m} \tag{6-1.9}$$

To test our construction of the above stochastic process algorithm, we compared the numerically evaluated magnitude of the normalized auto-correlation function of a signal propagating in a dispersionless Kerr medium with that corresponding to the exact analytical expression given by [88]

$$K(T,V)=E_0^2\exp(-i\,\omega_0\,T)\frac{f}{\left[1+\alpha^2\left(1-f^2\right)\right]^2} \tag{6-1.10}$$

where f is the two point correlation function and $\alpha=K\varepsilon V/2$. The agreement is remarkably good. It should be pointed out that the larger the dimension of the $\phi(V)$, the more accurate is the correspondence.In general, increasing the ensemble size L decreases

the sidebands (wiggles in the wings) magnitude, and increasing the time sampling rate gives a better fit at t=0. To make sure the evolution equation worked on the incoherent ensemble elements, energy conservation for each element was monitored.

We choose the initial T_c to be 50 fs., the power of the signal to be just under the typical fibre damage threshold, the incoherent signal center frequency to correspond to 1 μm, and the fibre parameters to be typical values for glass.

1) In fig. 6-1, we plot the normalized auto-correlation function for various propagation distances. The coherence time decreases with an increase in εV.

2) In fig. 6-2, the normalized auto-correlation function is compared to the simple Kerr model. The coherence time agrees well with the simple Kerr model [88] for small distances of propagation. This is due to the observation that the dispersion and higher order effects have negligible effects in the initial part of the evolution.

3) In fig. 6-3, the compression ratio of the half-width at half-maximum of the full model is compared with the predictions of the simple Kerr model. The deviation between the two models increases as the parameter εV increases or equivalently as the distance of propagation in the Kerr medium. The simple theory overestimates this quantity for high εV versus the results of the complete theory because of the absence of dispersion, while for low εV the Raman effect in the complete theory adds to the spectral distribution and therefore to the compression ratio. The limiting value of the coherence time can be estimated by noting that this quantity

squared is up to a factor of order one equal to $\beta^{(2)}\lambda/\left(\pi n_2 E_0^2\right)$. This limiting value is manifested by the observed saturation in the compression ratio. For $\varepsilon V=0.3$, and for the parameters chosen, the half-width at half maximum decreases to a value less than 4 fs.. This value is comparable to the shortest coherent pulses so far produced.

4) In fig. 6-4, the spectral distribution is plotted for various propagation distances. The spectral distribution width of the outgoing incoherent light for increasing values of εV increases with εV. and the product of the spectral width by the coherence time remains constant.

It should be emphasized that compression of the coherence time of an incoherent light occurs all within the fibre without the necessity for the external grating-prism system required for the compression of a coherent pulse of equivalent time resolution. The disadvantage is that, although the noise intensity amplitude may be below the material damage limit, some of the spikes maxima are not thus limiting the intensity amplitude for the incoherent signal to a value lower than the peak of the coherent pulse.

6.2) Incoherent Signals (2D Signal Coherence Length Compression).[d]

The study of incoherent pulses in the anomalous dispersive region is complicated by the fact that pulses of sufficiently high power are difficult to achieve. However, the anomalous dispersion of a temporal pulse is mathematically equivalent to diffraction of a spatial 2D beam except there is no analogy to the higher order nonlinear processes (i.e. Self-Steepening etc.). Therefore, by studying the corresponding spatial problem, we accomplish two things.

1) We study a real physical problem of incoherent spatial signals.

2) We are able to draw analogy to the incoherent signal in the anomalous dispersive regime. If sources become available, the results will apply to this case as well.

The method of approach is nearly identical to the previous treatment of incoherent signals with a desired coherence time. The main feature of a 2-dimensional Kerr medium is the possibility of formation of spatial solitons. These solitons have recently been observed in a planar waveguide [48] and in the quasi 2D geometry [49] (i.e. with highly elliptical beams). For this geometry the differential equation for the electrical field envelope is given by

$$-i\frac{\partial A}{\partial z}-\frac{1}{2k}\frac{\partial^2 A}{\partial x^2}=\frac{n_2 k}{n_0}|A|^2 A \qquad (6\text{-}2.1)$$

where n_2 is the nonlinear index of refraction, n_0 is the linear index of refraction, k is the wave number, z is the spatial longitudinal component and x is the transverse component.

The source beam, at the input plane of the nonlinear material, is assumed to be a Gaussian Stochastic complex field [85] in the transverse component. Writing $A(x,z)=E_0\,\phi(x,z)$, the transverse two-points correlation function at the point of observation z is

$$K(X,z)=E_0^2\left\langle\phi^*(x+X,z)\phi(x,z)\right\rangle \qquad (6\text{-}2.2)$$

where the brackets refer to an ensemble averaging. To compute this function for an arbitrary z , we use the standard algorithms for Gaussian processes which were outlined in the previous problem. The initial correlation function of the random process is given by

$$K(X,0)=E_0^2\left\langle\phi^*(x+X,0)\phi(x,0)\right\rangle=E_0{}^2\,\exp\left(-\left(\frac{X}{X_c}\right)^2\right) \qquad (6\text{-}2.3)$$

where X_c is the initial coherence length. The random process is advanced in the same manner that the time problem was except that each ensemble propagates via equation 6-2.1 Calculation of the coherence lengths for any distance proceeds in an analogous manner and will not be repeated here.

1) In fig. 6-5, we plot for $\mathbf{N^2}$=40 and 400 the initial and final state of a representative element of the ensemble. The initial signal (i.e. ensemble element) pulses compress and break-up in cascade leading to spikes at the output plane which are narrower than those at z =0

which will lead to a correlation length at the output shorter than at z =0. The spikes are seen to be narrower as the input power increases. [The parameter α is defined through $\alpha = k n_2 E_0^2 z / n_0$ and corresponds physically to the phase shift associated with the nonlinear index of refraction for a value of the field equal to E_0].

2) In fig. 6-6, the normalized transverse correlation function is plotted for various propagation distances. The computed correlation functions differ in shape from Gaussian and the variance is of the order of a few percent. However, to facilitate comparison, we use the Gaussian least-square fit to the correlation function (since a width is well defined only for a curve described by a single parameter and the gaussian curve is the natural parameterization), for different values of the parameter α, as function of the normalized transverse coordinate. We note that the correlation function narrows, i.e. the transverse coherence length shortens with an increase in the value of α and the rate of this compression decreases with an increase in the value of α.

3) In fig. 6-7, the compression ratio of the gaussian fit to the correlation function is plotted as a function of the propagation distance. The compression ratio is defined as the ratio of the initial transverse coherence length over the coherence length at the point of observation z. We note that the compression curve increases almost linearly for small values of α and hovers around an asymptote for large values of α. To see the reason for these limiting behaviors, first we introduce the length $z_0 = n_0 / \left(k n_2 E_0^2 \right)$ as a scaling factor in the z-dimension. Then it is easy to see that the $\partial^2 / \partial x^2$ term in the field equation can be neglected if the coherence length is much larger than

$\sqrt{z_0 / 2k}$. The propagation equation then reduces to the Self-Phase Modulation equation whose solution can be explicitly written analytically:

$$\lim \phi(x,z) \rightarrow \phi(x,0) \exp\left[i \frac{k n_2 E_0^2 z}{n_0} |\phi(x,0)|^2 \right] \qquad (6\text{-}2.4)$$

and the corresponding correlation function can be analytically computed by using the factorizability property of the Gaussian process to give [88]

$$\lim K(X,z) \rightarrow \frac{E_0^2 f}{\left[1+\alpha^2\left(1-f^2\right)\right]^2} \qquad (6\text{-}2.5)$$

The compression of the coherence length associated with this expression, follows closely for large coherence length (i.e. small propagation distance) the numerically evaluated curve resulting from solving the full equation. We point out that the coherence length compression that we are predicting may be measured through a diffraction experiment. Specifically, Schell's theorem [89] relates the diffraction pattern smoothing to the decrease of the coherence length as a function of the aperture size.

The asymptotic behavior observed for large α is due to the ensemble forming spatial solitons. In this case, the spikes formed in any of the ϕ rows (elements of the statistical ensembles) reaches a stable width which is a function of the field intensity. In this limit, the self-phase modulation term balances the diffraction term in the equation of motion thus satisfying the condition for the formation of

a fundamental spatial soliton configuration. Under these conditions the magnitude of the soliton and the width of the spatial soliton are specifically related. The minimum achievable coherence length is obtained by equating the fundamental width of the fundamental spatial soliton with the minimum coherence length with the proviso of making the adjustment necessitated by the sech shape of the soliton versus the assumed Gaussian form function of the two-point correlation function. The minimum coherence length is then given by

$$(X_c)_{\min} \approx \frac{1.085}{k}\sqrt{\frac{n_0}{n_2 E_0^2}} \qquad (6\text{-}2.6)$$

4) A novel feature not observed in the normal dispersive time correlation problem are oscillations of the compression ratio (coherence length) as a function of propagation distance. Since the soliton widths are related to the local intensity and their velocity related to the local phase information and these vary chaotically about their mean values, the coherence length is expected to fluctuate about its mean value.

5) We note that the compression ratio in the diffractive (anomalous dispersive regime) is almost twice that of the normal dispersive regime for the same input intensity. This affords the hope that if pulses of sufficient power in the anomalous dispersive regime are achievable, then the correlation times can be compressed to even smaller values then those obtained in the normal dispersive regime.

Figure Captions

Fig. 6-1 The magnitude of the normalized auto-correlation function is plotted as function of the normalized time.

*Incoherent Signal Parameters: T_c=50 fs , λ_0=1 μm , $n_2 E_0^2 = 10^{-3}$.

*Material parameters: $\Omega_R = 4.76$, $\Gamma_R = 4.85$, χ_0= 0.275

$$\beta^{(2)} = 2\times10^{-26}\ s^2/m\ ;\ \beta^{(3)} = 5\times10^{-41}\ s^3/m\ .$$

i) εV=0 ii) εV=0.06 iii) εV=0.1 iv) εV=0.2 v) εV=0.26.

Fig. 6-2 Comparison of the magnitude of the normalized auto-correlation function between the full theory and the simple dispersionless theory.The parameters of fig.6-1 are assumed.

i) εV=0.1, full theory ii) εV=0.1, dispersionless theory

iii) εV=0.26, full theory iv) εV=0.26, dispersionless theory.

Fig. 6-3 The compression ratio of the half-width at half-maximum as function of εV. The parameters of fig.6-1 are assumed. τ^{in}_{HWHM}= 41.63 fs.

i) full theory ii) dispersionless theory.

Fig. 6-4 The spectral distribution is plotted as a function of the frequency difference multiplied by the initial coherence time (i.e., the normalized frequency difference). The parameters of fig.6-1 are assumed.

i) εV=0 ii) εV=0.06 iii) εV=0.1 iv) εV=0.2 v) εV=0.26.

Fig.6-5 A representative element of the stochastic Gaussian ensemble is plotted, (i) at the entrance face of the nonlinear material z =0 (ii) at the exit face of the nonlinear material, as a function of the normalized transverse distance. In these units, the spatial coherence length is 1. The parameter α at the exit plane is

$\alpha = k n_2 E_0^2 z / n_0 = 15$. a). $n_2 E_0^2 / n_0 = 2/3 \times 10^{-3}$.

b). $n_2 E_0^2 / n_0 = 2/3 \times 10^{-2}$.

[In all the figures L=50, M=512, and the grid element size is $X_{c,in.} / 200$].

Fig.6-6 The Gaussian least-square fit to the transverse coherence function is plotted as a function of the normalized transverse distance $(X / X_{c,in.})$ for different values of the parameter α $(\alpha = k n_2 E_0^2 z / n_0)$. $X_{c,in.} = 50\lambda$.

a) $n_2 E_0^2 / n_0 = 2/3 \times 10^{-3}$: (i) $\alpha = 0$ (ii) $\alpha = 1$ (iii) $\alpha = 2$ (iv) $\alpha = 4$.

b) $n_2 E_0^2 / n_0 = 2/3 \times 10^{-2}$: (i) $\alpha = 0$ (ii) $\alpha = 2$ (iii) $\alpha = 4$ (iv) $\alpha = 8$.

Fig.6-7 The coherence length compression ratio is plotted as a function of α. (i) numerically evaluated curve for $n_2 E_0^2 / n_0 = 2/3 \times 10^{-3}$;(ii) numerically evaluated curve for $n_2 E_0^2 / n_0 = 2/3 \times 10^{-2}$;(iii) small distance of propagation approximate curve; (iv) large distance of propagation asymptotic value for $n_2 E_0^2 / n_0 = 2/3 \times 10^{-3}$; (v) large distance of propagation asymptotic value for $n_2 E_0^2 / n_0 = 2/3 \times 10^{-2}$. $X_{c,in.} = 50\lambda$.

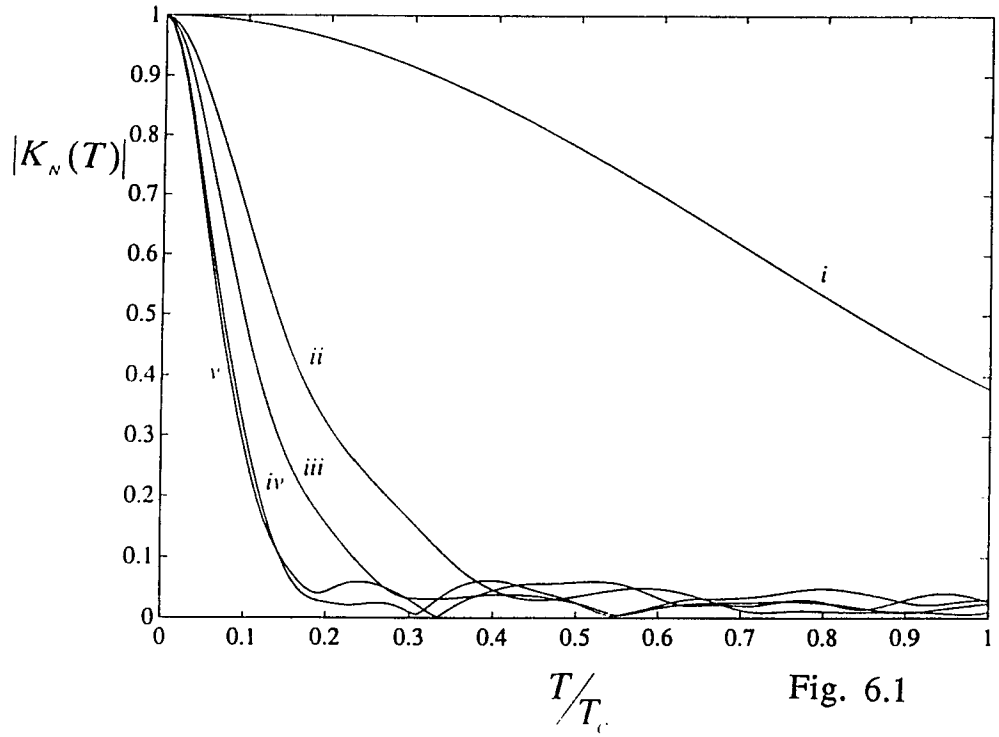
$|K_N(T)|$
1
0.9
0.8
0.7
0.6
0.5
0.4
0.3
0.2
0.1
0
0 0.1 0.2 0.3 0.4 0.5 0.6 0.7 0.8 0.9 1
i
ii
iii
iv
v
T/T_c

Fig. 6.1

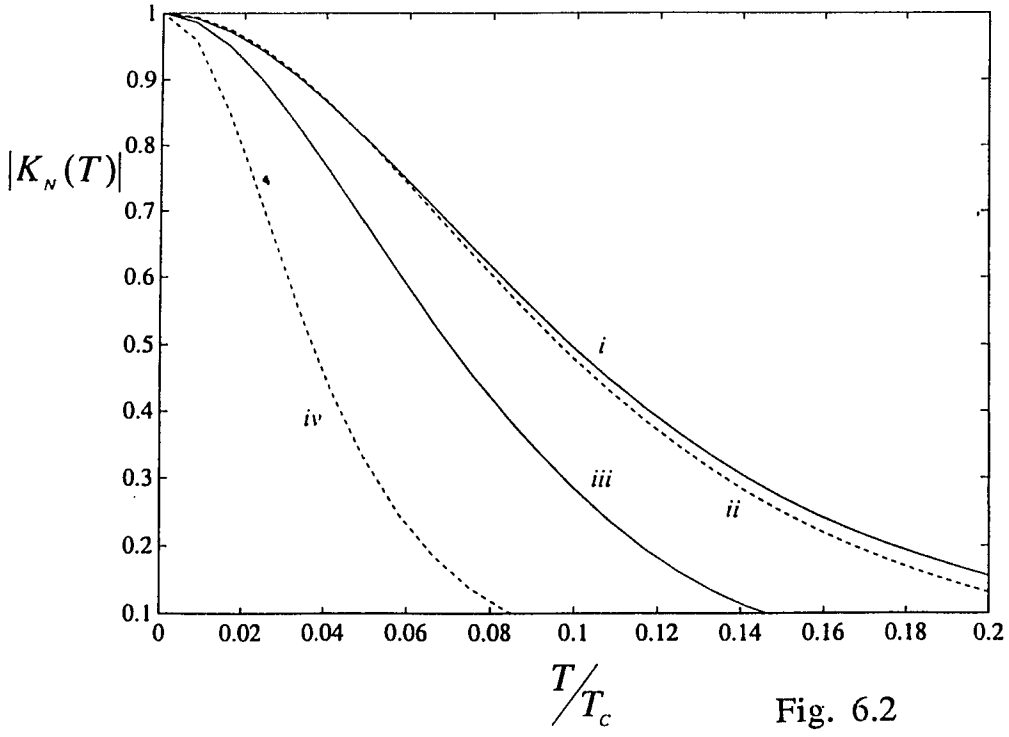
$|K_N(T)|$
1
0.9
0.8
0.7
0.6
0.5
0.4
0.3
0.2
0.1
0 0.02 0.04 0.06 0.08 0.1 0.12 0.14 0.16 0.18 0.2
i
ii
iii
iv
T/T_c

Fig. 6.2

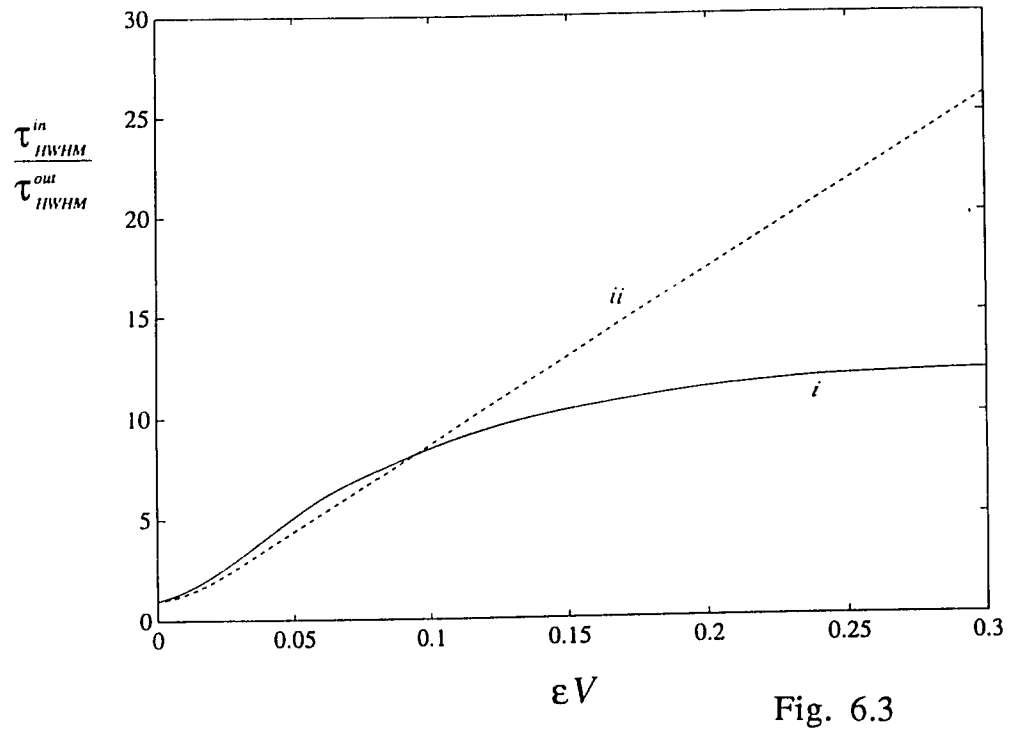
$\frac{\tau^{in}_{HWHM}}{\tau^{out}_{HWHM}}$
30
25
20
15
10
5
0
0
0.05
0.1
0.15
0.2
0.25
0.3
ii
i
εV

Fig. 6.3

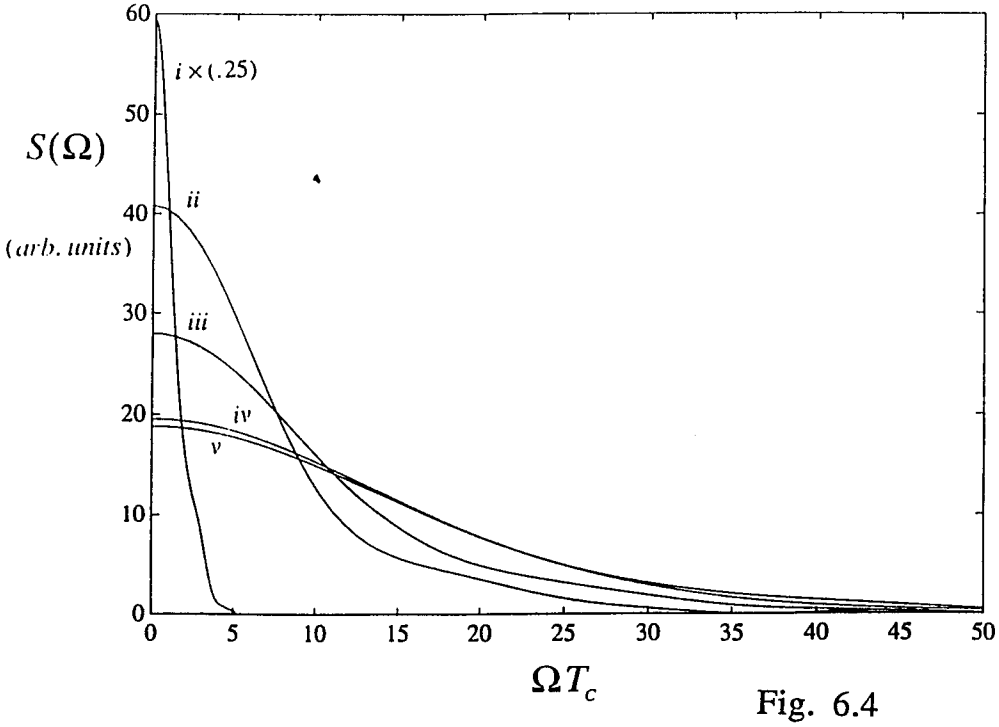
S(Ω)
(arb. units)
60
50
40
30
20
10
0
i × (.25)
ii
iii
iv
v
0
5
10
15
20
25
30
35
40
45
50
ΩT_c

Fig. 6.4

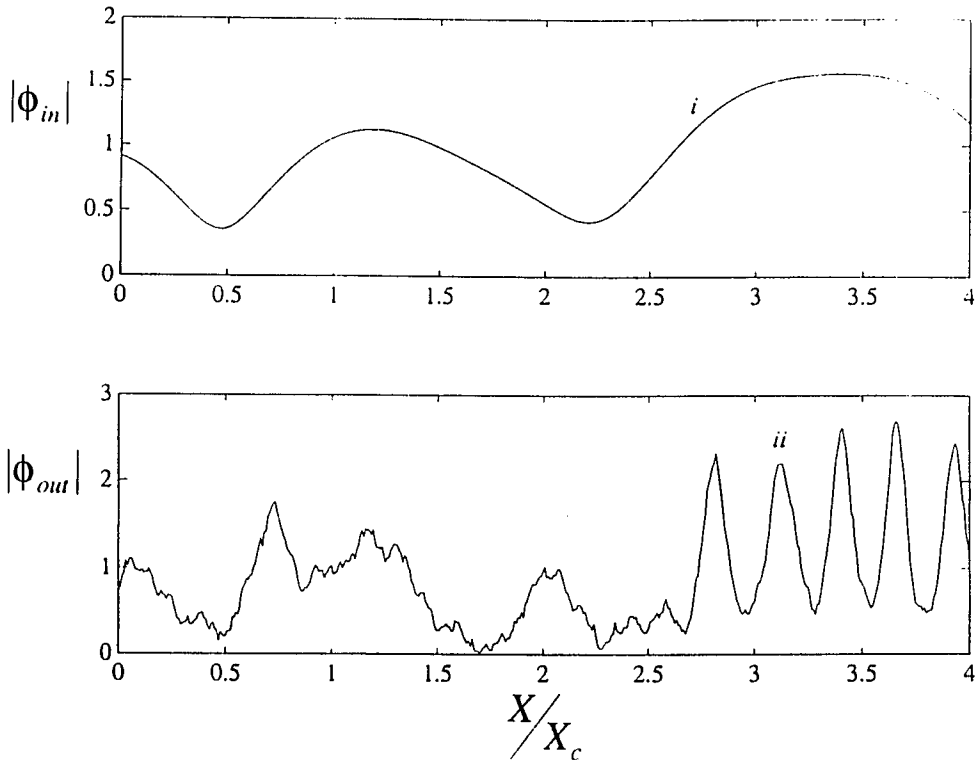

Fig. 6.5a

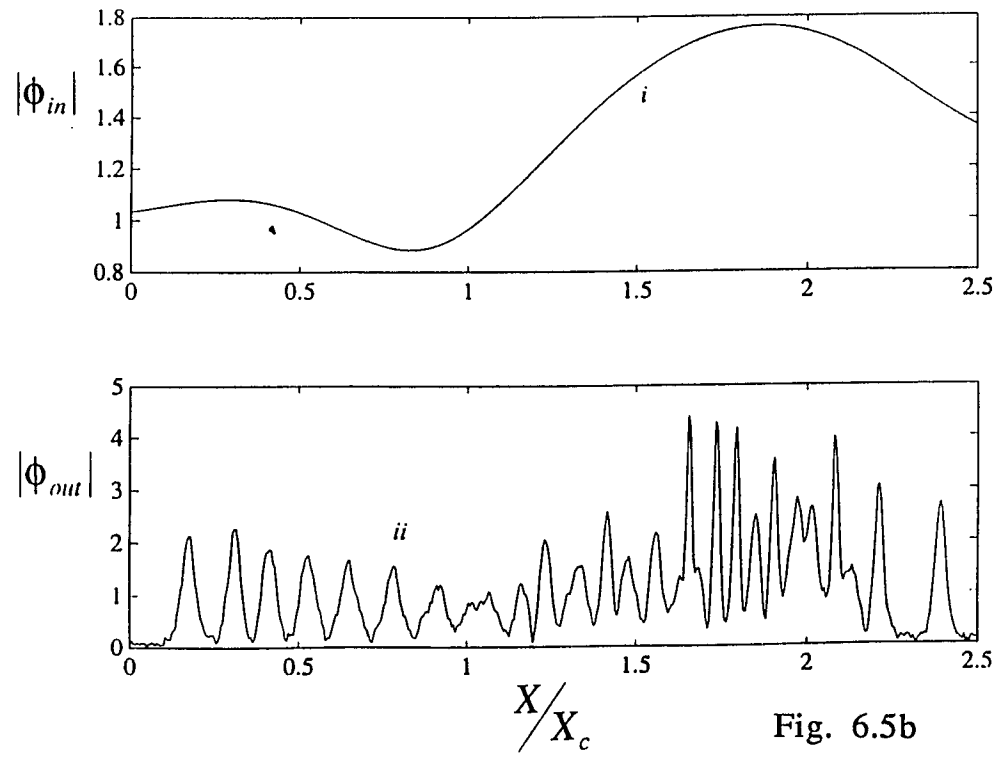

Fig. 6.5b

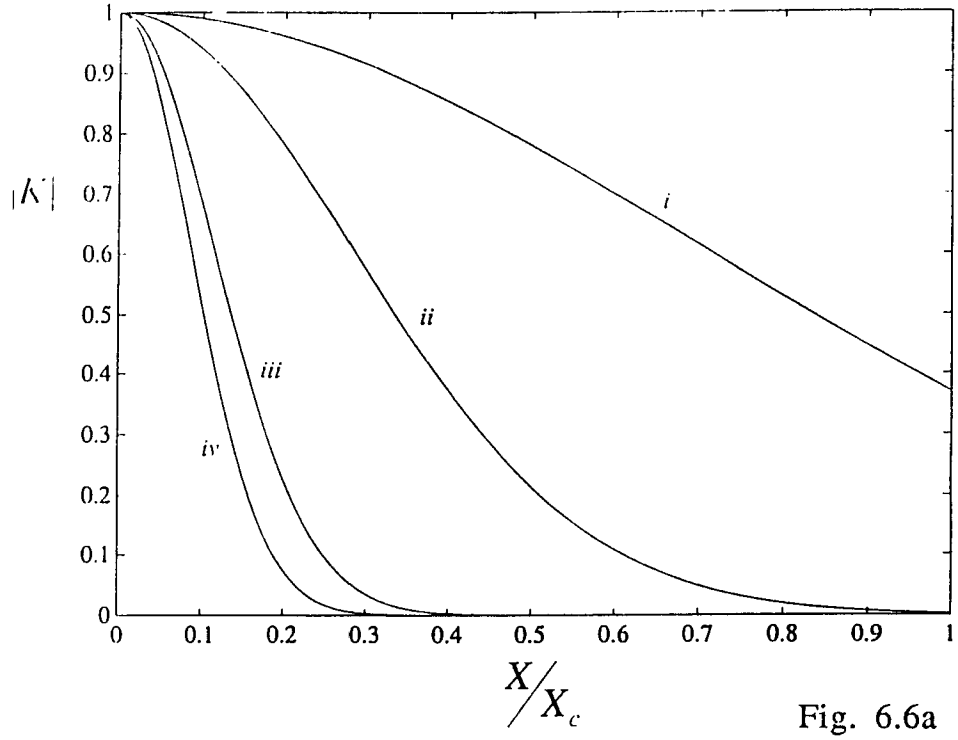

Fig. 6.6a

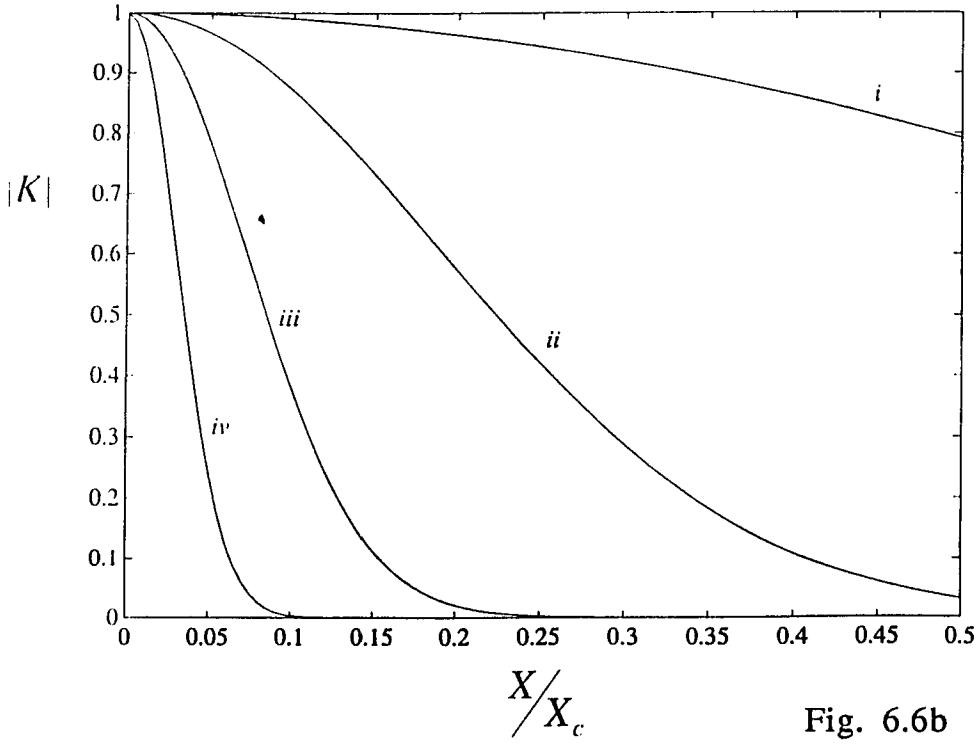

Fig. 6.6b

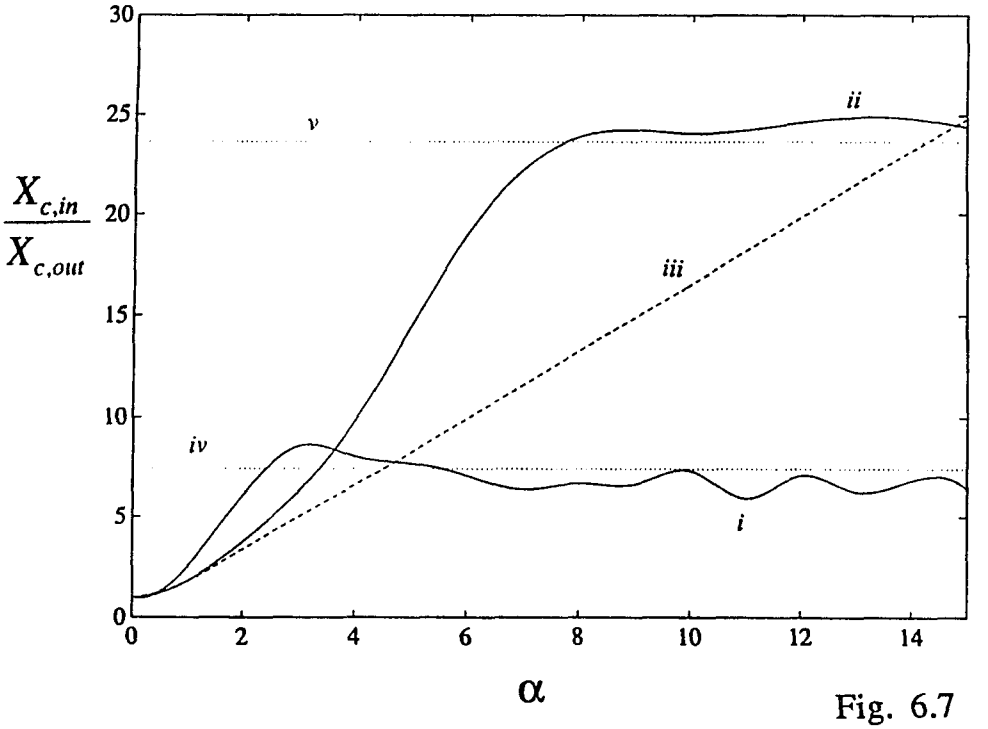

Fig. 6.7

7) Numerical Algorithms

When studying the propagation of intense optical fields, one encounters a nonlinear partial differential equation of parabolic type (i.e. first order in the longitudinal derivative using suitable approximations). This type of equation for a general nonlinear interaction does not have known analytical solutions and one resorts to numerical procedures. The equation we are concerned with is of the form

$$\frac{\partial \psi}{\partial \bar{z}} = F\left(\frac{\partial}{\partial U}, \psi\right) \tag{7.1}$$

where U is the normalized time and $\bar{z}$ is the normalized longitudinal distance. For illustration, we assume that no space transverse coordinates are used in the description (i.e. plane wave approximation) Later, we explain how to generalize our methods to these cases. Numerical algorithms to solve equations of this form can be constructed [90-96].

They may be classified into two broad categories:

1. Finite Difference schemes.
2. Spectral Methods .

Due to the complexity (high degrees of freedom) of the problems undertaken, finite difference methods are too slow [96] and stability problems cause different difference schemes to be unpredictable (i.e. a difference scheme for one type of nonlinearity may not work for another nonlinearity). On the other hand, progress in spectral methods (i.e. Fast Fourier Transforms) and multi-dimensional extensions prove more rapid for achieving the same

accuracy. We concentrate in the spectral methods since they are more efficient and also many of the nonlinear operators we encounter are more easily written in the spectral domain.

Furthermore, the spectral decomposition into monochromatic modes is an important physical realization for temporal pulses. To see the value of spectral methods, we look at the simple case of a linear equation. This is the equation describing dispersion (diffraction). In this case, we have

$$\frac{\partial \psi}{\partial \bar{z}} = F\left(\frac{\partial}{\partial U}\right)\psi \tag{7.2}$$

where F is a polynomial function. In the spectral domain we have

$$\frac{\partial \hat{\psi}}{\partial \bar{z}} = F(i\Omega)\hat{\psi} \quad \text{where} \quad \hat{\psi} = \frac{1}{\sqrt{2\pi}} \int_{-\infty}^{\infty} \exp(i\Omega U)\psi(U,\bar{z})dU \tag{7.3}$$

which when integrated gives

$$\hat{\psi}(\Omega,\bar{z}) = \exp\left(F(i\Omega)\bar{z}\right)\hat{\psi}(\Omega,0) \tag{7.4}$$

If the equation is nonlinear and F depends on the field as well as its time derivatives, Fourier transformation is complicated since the transform of nonlinear terms results in convolutions. To see how spectral methods can be applied to nonlinear problems, we examine a method well known in the literature [97]. Consider the equation

$$\frac{\partial \psi}{\partial \bar{z}} = \left(F_1\left(\frac{\partial}{\partial U}\right) + F_2(\psi)\right)\psi \tag{7.5}$$

where we have separated the dispersive (transverse) and the nonlinear operators. This separation is not possible in all cases considered. Up to order $O(h^2)$, this equation has local solution

$$\hat{\psi}(\bar{z}+h)=\exp\left(hF_1\left(\frac{\partial}{\partial U}\right)\right)\exp\left(hF_2(\psi)\right)\psi(\bar{z}) \qquad (7.6)$$

where the Baker-Hausdorff theorem in noncommuting operators [98] is applied. If h is sufficiently small, F_2 may be evaluated at the initial point of the interval. Under this approximation, the field at the endpoint is given by:

$$\psi(\bar{z}+h)=\Im_U^{-1}\left(\exp\left(hF_1(i\Omega)\right)\Im_\Omega\left(\psi_1(\bar{z})\right)\right) \quad \text{where} \qquad (7.7)$$

$\psi_1(\bar{z})=\exp\left(hF_2(\psi)\right)\psi$ and $\Im_U^{-1}$ is the inverse transform and $\Im_\Omega$ is the fourier transform.

This procedure can then be iterated indefinitely through the medium. This method is known as the split-step Fourier method and has found wide application in many propagation problems. In the context of beam propagation in varying index fibers, the method is commonly referred to as the beam propagation method. The accuracy increases as the step size decreases and more steps are taken. This method has accuracy $O(h^2)$ but by expanding the exponential operator using the Baker-Hausdorff theorem to higher order, better approximations may be made such as the symmetrized split step [99] method which is accurate to $O(h^3)$. Unfortunately, the necessary grid size is difficult or impossible to determine for different operators and one is not guaranteed a given accuracy. To avoid these difficulties,

we propagate using an adaptive technique while still maintaining the advantages of the spectral method.

To illustrate the idea, consider the following parabolic equation:

$$\frac{\partial \psi}{\partial \bar{z}} = F_1(\psi) F_2\left(\frac{\partial}{\partial U}\right) F_3(\psi) \tag{7.8}$$

In all our problems, it is possible to break the operator into a sequence of nonlinear and dispersive (transverse) operators. By folding and unfolding the operators , we have the following formal representation of this equation in the spectral domain

$$\frac{\partial \hat{\psi}}{\partial \bar{z}} = \Im_{\Omega}\left(F_1\left(\Im_U^{-1}(\hat{\psi})\right)\Im_U^{-1}\left(F_2(i\Omega)\Im_{\Omega}\left(F_3\left(\Im_U^{-1}(\hat{\psi})\right)\right)\right)\right) \tag{7.9}$$

which may be put into the general form

$$\frac{\partial \hat{\psi}}{\partial \bar{z}} = F\left(i\Omega, \hat{\psi}\right) \tag{7.10}$$

Therefore the R.H.S can be calculated if the field (transform of the field is known). One may then advance the solution to second order $O(h^2)$.

$$\hat{\psi}(\bar{z}+h) = \hat{\psi}(\bar{z}) + hF\left(i\Omega, \hat{\psi}(\bar{z})\right) + O\left(h^2\right) \tag{7.11}$$

This is formally equivalent to the split-step method. However, the propagation equation is of the form in which longitudinal advancement by more sophisticated adaptive method is possible. The most flexible method is the Runge-Kutta [100] adaptive method which extends the Euler method. The greater number of derivative

evaluations makes the method slower for a given step but the steps are longer and the method is adaptive so slower field variations are covered faster and global accuracy is assured at the call level. Applying the Runge-Kutta technique to a partial differential equation is possible since the partial differential equation is equivalent to N coupled ordinary differential equations for the single frequency modes. Here, N is the number of discretized modes (positive and negative frequency modes being counted separately). If the equation is linear, the coupled system is decoupled and each mode propagates separately. Furthermore, many of the nonlinear interaction terms are most easily represented in the spectral domain (Raman scattering) and it seems most natural to discuss spectral broadening in the spectral domain. Furthermore, this formalism can be extended to multiple fields whose spectra overlap and a time domain method is no longer applicable.

In this chapter, using time as the transverse coordinate is only a convenience in this discussion. This method applies to any transverse system of coordinates. For example if U is replaced by (X,Y), the partial derivative is replaced by the gradient operator and the single dimensional F.F.T's employed are replaced by the corresponding multi-dimensional extensions. Also space and time can be treated as a 3 vector without changing the argument. However, every increase in the degrees of freedom results in a large increase in computation time .

In what follows, we discuss first the important numerical subroutines used. After this, we will go through each program used in the areas where we have given numerical results. The subroutines

occur often and will not be redescribed and only the driver programs which construct the mathematical equations (the function F) to the Runge-Kutta and the main program which initiates the global Runge-Kutta will be explained.

1) Fast Fourier Transforms (F.F.T's)

The value of using spectral techniques to prepare the transverse data is that the transverse differential operators become algebraic operators. Since all numerical problems use finite sampled data, the continuous transform is really a Discrete Fourier Transform (D.F.T.). The discrete transform is defined by the transform pair :

$$\hat{\psi}(k) = \sum_{n=0}^{n=N-1} \psi(n) \exp\left(\frac{2\pi i n k}{N}\right) \tag{7.12a}$$

$$\psi(n) = \frac{1}{N} \sum_{k=0}^{k=N-1} \hat{\psi}(k) \exp\left(\frac{-2\pi i n k}{N}\right) \tag{7.12b}$$

Evaluating the D.F.T from a sample of N points using the above formulae's requires ~ N^2 operations. However, improvements in the speed of evaluating the D.F.T put the operation count ~ $N\log_2(N)$. The fundamental idea in this saving is the observation that the N point transform is the sum of 2 N/2 point transforms on the even and odd positions of the data. Applying this recursively, $\log_2(N)$ times gives the N point transform as a sum of N 1 point transforms. The value of these 1 point transforms is the initial data itself in a position which is calculated using bit reversal technique. The bit reversal supplies the N operations giving the desired operation count. More details may be found in [101-103] and the source of the code is [104].

2) Multi-dimensional Fast Fourier Transforms .

When more than one variable is required to describe the transverse variation of the field, it is convenient to transform the data into the multi-dimensional analog of the frequency space. In our problems in which we encountered multi-dimensional transverse variation, we were looking at 3D beam propagation so the frequency space is the spatial frequency space and the mode solutions are plane waves at various angles to the beam axis. Also, the transverse grid need not be symmetric in spacing or number of points. Here, the discussion focuses on the two Dimensional Discrete Transform and its implementation. In the two dimensional case, the transform pairs are

$$\hat{\psi}(k_1,k_2) = \sum_{n_2=0}^{n_2=N_2-1} \sum_{n_1=0}^{n_1=N_1-1} \psi(n_1,n_2) \exp\left(\frac{2\pi i n_1 k_1}{N_1}\right) \exp\left(\frac{2\pi i n_2 k_2}{N_2}\right) \qquad (7.13a)$$

$$\psi(n_1,n_2) = \frac{1}{N_1 N_2} \sum_{k_2=0}^{k_2=N_2-1} \sum_{k_1=0}^{k_1=N_1-1} \hat{\psi}(k_1,k_2) \exp\left(\frac{-2\pi i n_1 k_1}{N_1}\right) \exp\left(\frac{-2\pi i n_2 k_2}{N_2}\right) \qquad (7.13b)$$

and obvious extension can be made to any finite dimension. From these expressions, one can in general implement the 2 Dimensional transform as N_2 one dimensional transforms of length N_1. This requires a lot of wasted computer effort as the data must continuously be loaded and unloaded. We make use, instead, of a general purpose multi-dimensional F.F.T. The data is stored not as multi-dimensional arrays but as single dimensional arrays. Therefore a special ordering chosen beforehand as a rule must be given. These details are explained in [101] and the source of the code is [105].

3) Numerical integration of 1st order P.D.E. (Runge-Kutta Method).

We have shown that the partial differential equations of parabolic type may be transformed into a system of coupled ordinary differential equations where the dependant variables are the modal fields. These equations are of the form

$$\frac{dy_i}{dx} = f_i\left(x, y_1 \cdots y_N\right), \quad i = 1 \cdots N \tag{7.14}$$

for N modes and the f's are known functions of the dependant and independent variables (not their derivatives). Besides the simple advancement procedures such as the midpoint method and Euler methods, a number of sophisticated advancement procedures have been developed which possess better accuracy [106] . Three of the most useful are

1) Runge-Kutta methods.
2) Richardson extrapolation methods.
3) Predictor Corrector methods.

The general rule is that the Runge-Kutta algorithms work under a wider variety of problems while the other two may be faster but do not have as wide a range of validity. In other words, the Runge-Kutta advance will always work but it may be less than optimally efficient. Since it is our aim to use our algorithms over a wide variety of physical situations, we have concentrated on the Runge-Kutta schemes. Such schemes are difficult to parallel process since the algorithm is recursive. The standard scheme is put into the highly symmetric form

$$y_{n+1} = y_n + \frac{k_1}{6} + \frac{k_2}{3} + \frac{k_3}{3} + \frac{k_4}{6} + O\left(h^5\right) \quad \text{where} \tag{7.15}$$

$$k_1 = hf\left(x_n, y_n\right) \tag{7.16a}$$

$$k_2 = hf\left(x_n + \frac{h}{2}, y_n + \frac{k_1}{2}\right) \tag{7.16b}$$

$$k_3 = hf\left(x_n + \frac{h}{2}, y_n + \frac{k_2}{2}\right) \tag{7.16c}$$

$$k_4 = hf\left(x_n + h, y_n + k_3\right) \tag{7.16d}$$

Here x_n is the initial point, x_{n+1} is the end point, h is the interval size, y_n is the initial dependant vector and y_{n+1} is the estimated dependant vector at the endpoint.

This scheme involves four function evaluations per step. To compare, the midpoint method requires two function evaluations. To apply this directly does not insure any global accuracy over the step. To have this important facility, we require a way to estimate the error over this step and if the error is greater than the desired error, adjust the step size appropriately and try again. The details of the particular method of estimation are not explained here. For details in error estimation for the Runge-Kutta step, see [105] . The actual code used was found in the software package Matlab and converted into Fortran for greater speed and universality.

Now that the subroutines have been explained and the general outline of our propagation scheme given, we explain in more detail the algorithms for each physical problem. In order to propagate equations of the general form 7.1, the function is sampled over the transverse coordinate(s) (in this case U) forming a system of coupled first order differential equations which are of the form 7.14. The functions y_i are the sampled functions

$$y_i(\bar{z}) = \psi(i\Delta U, \bar{z}) \tag{7.17}$$

where i is a discretization index and ΔU is the sampling interval. A generalization to multi-dimensional transverse problems is straight forward. Once the equation is reduced to the system of O.D.E's, standard prepackaged subroutines can be used to solve these systems. All that is required is the construction of the driving functions $f_i(y_k,z)$ where i and k are indices labeling the discretization.

In chapter 2, the propagation of an intense femtosecond pulse in a fiber was shown to be described by the equation

$$\begin{aligned}\frac{\partial \tilde{\phi}(\Omega,V)}{\partial V} = {} & \frac{i\varepsilon K}{2}\left(1-\frac{\Omega}{K}\right)\mathbf{F}\left[|\phi(U,V)|^2\phi(U,V)\right] \\ & + \frac{i\varepsilon K}{2}\mathbf{F}\left\{\phi(U,V)\mathbf{F}^{-1}\left[\chi_R(\Omega)\mathbf{F}\left[|\phi(U,V)|^2\right]\right]\right\} \\ & + i\left(v_g\tau\right)\sum_{k=2}^{\infty}(-1)^k\frac{\beta^{(k)}\Omega^k}{k!\,\tau^k}\tilde{\phi}(\Omega,V)\end{aligned} \tag{7.18}$$

The symbol descriptions are the same as those given in Chapter 2. In this case, the transverse variable used is Ω since the differential equation takes on a simpler form in this domain and the propagation variable is V. If we discretize the frequency coordinate and make the following identifications:

$$\tilde{y}_i(V) = \tilde{\phi}(i\Delta\Omega, V) \qquad \text{where} \quad i = -\frac{N}{2}\cdots\frac{N-1}{2} \qquad \text{and} \quad \Delta\Omega = \frac{2\pi}{\Delta U}$$

then the forcing functions f_i are given by

$$f_i(\tilde{y}_k(V)) = \left(\begin{array}{l} \dfrac{i\varepsilon K}{2}\left(1-\dfrac{\Omega_k}{K}\right)\mathbf{F}\left[|y_l(V)|^2 y_l(V)\right] \\ +\dfrac{i\varepsilon K}{2}\mathbf{F}\left\{y_l(V)\mathbf{F}^{-1}\left[\chi_R(\Omega_k)\mathbf{F}\left[|y_l(V)|^2\right]\right]\right\} \end{array} \right)_i$$

$$+i\left(v_g\tau\right)\sum_{k=2}^{\infty}(-1)^k\frac{\beta^{(k)}(\Omega_i)^k}{k!\,\tau^k}\tilde{y}_i(V) \qquad (7.19)$$

Here F is the Fast Fourier Transform Operation and F^{-1} is the Inverse Fourier Transform Operation defined by equations 7.12a,b. They give a quick means of transforming between the time and frequency spaces. The dependant functions in both representations are connected by the reciprocal relations

$$\tilde{y}_i = \mathbf{F}[y_k] \qquad y_i = \mathbf{F}^{-1}[\tilde{y}_k] \qquad \textit{where} \qquad y_i = \phi(i\Delta U, V)$$

The multiplications are done as array operations and the order of operations is from right to left. This procedure yields N complex 1st order O.D.E's where N is the number of sample points. In general, the commercial algorithms require the system to be real. This is done by separating the N complex equations into 2N real equations by separating the real and imaginary parts of the system.

In Chapter 3, we investigate the self-focusing problem in Kerr media. In this case, there is no frequency spectrum since we use a continuous wave approximation. Instead, the field depends on 2 transverse spatial coordinates. This added dimensionality requires the modification of our algorithm. By Fourier transformation, the propagation equation 3-2.1 can be written in the spatial frequency space as

$$-\left(\lambda_{\bar{x}}^2+\lambda_{\bar{y}}^2\right)\hat{\psi}-2i\frac{\partial\hat{\psi}}{\partial\bar{z}}+p\mathbf{F}_{\lambda_{\bar{x}},\lambda_{\bar{y}}}\left(|\psi|^2\psi\right)=0 \quad \textit{where} \qquad (7.20)$$

$$\psi=\mathbf{F}_{\bar{x},\bar{y}}^{-1}\left(\hat{\psi}\left(\lambda_{\bar{x}},\lambda_{\bar{y}}\right)\right) \qquad (7.21)$$

The discretization of this equation is straight forward. We have

$$\tilde{y}_{i,j}(\bar{z})=\hat{\psi}\left(i\Delta\lambda_{\bar{x}},j\Delta\lambda_{\bar{y}},\bar{z}\right) \quad \underset{F^{-1}}{\overset{F}{\longleftrightarrow}} \quad y_{k,l}(\bar{z})=\psi(k\Delta\bar{x},l\Delta\bar{y},\bar{z})$$

$$i,k=-\frac{N_x}{2}\cdots\frac{N_x-1}{2}, \quad j,l=-\frac{N_y}{2}\cdots\frac{N_y-1}{2}, \quad \Delta\lambda_{\bar{x}}=\frac{2\pi}{\Delta\bar{x}} \quad \Delta\lambda_{\bar{y}}=\frac{2\pi}{\Delta\bar{y}}\tilde{y}_{i,j}$$

Here, N_x is the number of sampling points in the x direction and N_y is the number of sampling points in the y direction. The requisite driver functions are then given by

$$f_I\left(\tilde{y}_{i,j}(\bar{z})\right)=\left(\frac{-ip}{2}\mathbf{F}\left[\left|y_{k,l}\right|^2 y_{k,l}\right]\right)_I$$
$$-\frac{1}{2}\left(\left(i\Delta\lambda_{\bar{x}}\right)^2+\left(j\Delta\lambda_{\bar{y}}\right)^2\right)\tilde{y}_{i,j}(\bar{z}) \qquad (7.22)$$

The general index I is used to label the dependant variables in the system. The system consists of N_xN_y complex or $2N_xN_y$ real coupled O.D.E's. The single index I is related to the double subscription by a consistent convention. The one which we use here is the normal ordering procedure described in reference [101] . If this ordering is consistently used, no ambiguity in the Runge-Kutta algorithm will occur. As was implicitly assumed, the size and the spacing of the sample grids are independent in the x and y directions. We also note that the beam geometry only enters in the initial conditions and

therefore an independent discussion for the axially symmetric and nonsymmetric beams is not required.

Leaving chapter 4 until later, we discuss the algorithms used to model the propagation of 2D and 3D beam in resonant media. In the 3D case, the propagation equation 5-4.4 in the spatial frequency domain is given by

$$-\left(\lambda_{\bar{x}}^2+\lambda_{\bar{y}}^2\right)\hat{\phi}-2i\frac{\partial\hat{\phi}}{\partial\bar{z}}+\mathbf{F}_{\lambda_{\bar{x}},\lambda_{\bar{y}}}\left(\frac{ig_0(\Delta+i)\phi}{\left(\Delta^2+1+s|\phi|^2\right)}\right)=0 \qquad (7.23)$$

where the symbol definitions are the same as those given in the text. The construction of the driver functions used in this case are similar to the Kerr model. If the discrete transforms are related by

$$\tilde{y}_{i,j}(\bar{z})=\hat{\phi}\left(i\Delta\lambda_{\bar{x}},j\Delta\lambda_{\bar{y}},\bar{z}\right) \quad \underset{F}{\longleftarrow}\underset{F^{-1}}{\longrightarrow} \quad y_{k,l}(\bar{z})=\phi(k\Delta\bar{x},l\Delta\bar{y},\bar{z})$$

$$i,k=-\frac{N_x}{2}\cdots\frac{N_x-1}{2},\quad j,l=-\frac{N_y}{2}\cdots\frac{N_y-1}{2},\quad \Delta\lambda_{\bar{x}}=\frac{2\pi}{\Delta\bar{x}}\quad \Delta\lambda_{\bar{y}}=\frac{2\pi}{\Delta\bar{y}}$$

$$f_I\left(\tilde{y}_{i,j}(\bar{z})\right)=\left(\frac{-i}{2}\mathbf{F}\left[\frac{g_0(\Delta+i)y_{k,l}}{\Delta^2+1+s|y_{k,l}|^2}\right]\right)_I$$
$$-\frac{1}{2}\left(\left(i\Delta\lambda_{\bar{x}}\right)^2+\left(j\Delta\lambda_{\bar{y}}\right)^2\right)\tilde{y}_{i,j}(\bar{z}) \qquad (7.24)$$

where all the subscripts have the same meaning as in the Kerr medium case. In the 2D case, the driver functions are built up in a similar manner except for the use of 1 dimensional transforms and an appropriate modification of the diffraction operator. In this case, the appropriate driver functions are

$$f_i\left(\tilde{y}_k(\bar{z})\right)=\left(\frac{-i}{2}\mathbf{F}\left[\frac{g_0(\Delta+i)y_l}{\Delta^2+1+s|y_l|^2}\right]\right)_i$$
$$-\frac{1}{2}\left((i\Delta\lambda_{\bar{x}})^2\right)\tilde{y}_k(\bar{z}) \qquad (7.25)$$

and the connection between the transforms is given by

$\tilde{y}_i=\mathbf{F}[y_k]$ $\quad y_i=\mathbf{F}^{-1}[\tilde{y}_k]$ $\quad$ *where* $\quad y_i=\phi(i\Delta U,V)$

In chapter 6, we study the statistical properties of an incoherent signal propagating in an optical fiber. We describe the algorithm required to build up the desired signal, propagate it and measure its correlation properties. The code handling the propagation of incoherent signals consists of 3 parts.

1) The generation of the initial ensemble with the correct coherence time. This part is completely explained in chapter 6 (see 6-1.6 and 6-1.7 for details). For the Cholesky decomposition.,we use the code developed by Matlab Mathworks as part of the matlab software package. The random variables that form the columns were generated by the Matlab random number generator which calculates random variables of zero mean and unit variance.

2) The propagation of each ensemble element independently of each other. Each row of the initial random matrix propagates via the propagation equation. For the time signal, the evolution equation is given by 6-1.1 and for the spatial beam equation by 6-2.1. In each case, the construction of the driver functions follows .

3). A supplementary self-explanatory program which calculates the correlation function from the ensemble of states. This procedure is a coded version implementing equations 6-1.8 and 6-1.9

We have already noted that the code required to propagate the ensemble (each element) is of the same form as that used in the supercontinuum propagation. However, some technical details concerning ensembles in general create some new wrinkles.

1) The initial state is read in from the initial states generated by implementing the Cholesky decomposition method. Each initial ensemble state is not band limited as is the case in coherent propagation. Therefore, we must keep a careful watch on the total energy of each ensemble to ensure aliasing errors do not occur.

2) A control loop which loops around the ensemble elements is added. To speed up the program implementation, each ensemble state can be mapped into an independent processor in the computer,when available, since the propagation of each ensemble can run independently.

In chapter 4, we study pulse propagation through a resonant medium within the context of fiber amplifiers. We note that our algorithm requires the construction of driver functions of the form

$$f_i\left(\tilde{y}_k(\bar{z})\right) \quad , \tag{7.26}$$

where the notation is consistent with previous examples. It is clear that the driver function is a sum of two parts: $f_i=f_i(\text{fiber}) + f_i(\text{res})$. The construction of the fiber term has already been discussed so we concentrate here on constructing $f_i(\text{res})$ which is built by realizing the active two-level resonant term which is the last term of eqn. 4-2.4 when coupled to the Bloch equations 4-1.7a,b. The driver functions of the resonant term are symbolically

$$f_j = i\Psi K\tilde{\chi}(\Omega_j, \bar{z}) \tag{7.27}$$

and the discretization is given by

$$\tilde{\chi}(\Omega_j, \bar{z}) = \tilde{\chi}(j\Delta\Omega, \bar{z}) \qquad \text{where} \quad j = -\frac{N}{2} \cdots \frac{N-1}{2} \qquad \text{and} \quad \Delta\Omega = \frac{2\pi}{\Delta U}$$

and the physical meaning of the parameters are the same as eqn. 4 – 2.4 Unfortunately, the driver functions as written are not functions of the envelope functions in the spectral domain so are not yet of Runge-Kutta type. We require a connection between the discrete polarization and the discrete field. This is accomplished by integrating the bloch equations. As we have seen, the bloch equations are given by

$$-i\frac{\partial \chi}{\partial U} = \left[\Delta - i\Gamma_2\right]\chi - \frac{\theta}{2}(n\phi) \tag{7.28a}$$

$$-i\frac{\partial n}{\partial U} = \theta\left(\chi^*\phi - \phi^*\chi\right) + i\Gamma_1\left(n_i - n\right) \tag{7.28b}$$

where the dimensionless parameters θ, Δ, Γ_1, and Γ_2 are defined as in equations 4-1.7a,b. If the initial conditions are known:

$$n(U = \infty, \bar{z}) = -1, \chi(U = \infty, \bar{z}) = 0 \tag{7.29}$$

the bloch equations can be integrated for all further times using a standard Runge-Kutta algorithm. Therefore, the polarization is known in the time domain and can be easily converted onto the discretized frequency domain. In other words, knowledge of the field gives the polarization which in turn gives the driver functions. Schematically, this is represented by the following flow chart.

$$\tilde{\phi}(\Omega_k, \bar{z}) = \tilde{y}(k) \xrightarrow{\text{Ifft}} y(i)$$

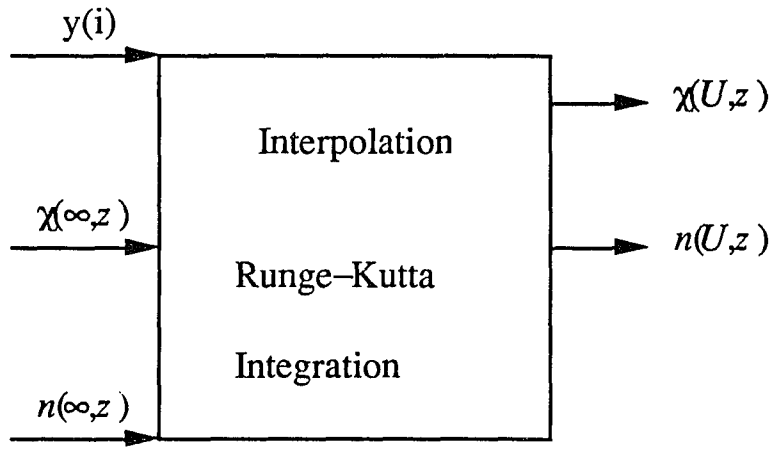

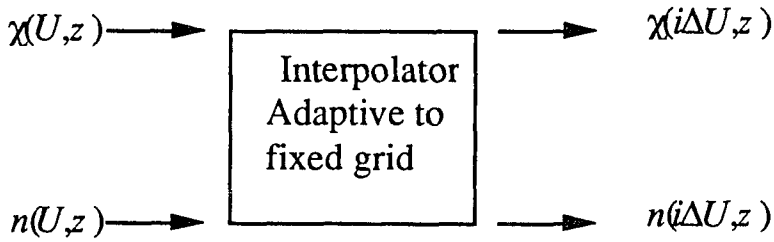

$$\chi(i\Delta U, \bar{z}) \xrightarrow{\text{fft}} \tilde{\chi}(k\Delta\Omega, \bar{z}) \Rightarrow f_j = i\Psi K\tilde{\chi}(j\Delta\Omega, \bar{z})$$

$$n(i\Delta U, \bar{z}) \xrightarrow{\text{fft}} \tilde{n}(k\Delta\Omega, \bar{z}) \qquad \text{(this term is not required)}$$

The need for the two interpolating subroutines are

1) Since the Bloch equations are integrated on an adaptive grid, the field must be available for any time. However, the initial field is known only over the fixed grid points. Therefore, we interpolate the field so that it is known for any time.

2) Similarly, the bloch vector must be mapped back onto the equidistant grid or the longitudinal step cannot be made. Another interpolation is done to accomplish this mapping.

8) Summary of Results

By numerically integrating the relevant partial differential equations of motion, we obtain the following results:

1) The classical description of supercontinuum generation in a Kerr Medium is shown to be incomplete when describing the evolution of intense femtosecond pulses. A more complete model which accounts for dispersive effects, self-steepening and Raman Scattering is developed and numerically integrated.

a) In the normal dispersive regime, the complete model shows that for sufficiently high intensity, the self-frequency shift (the shift of the central frequency) will be towards the blue in contrast to pico-second pulse propagation in which Raman Scattering is dominant causing a net red-shift.

b) In the anomalous regime, the complete model extends past work in describing the evolution of a Raman Generated stokes pulse. Quantitative differences with the classical model are shown to exist.

2) The propagation of an intense beam in a Kerr Medium leads to a catastrophic self-focusing above a certain threshold power. The semi-analytic methods in the literature are shown to be incomplete in describing the quantitative features of self-focusing. A numerical investigation shows clearly the regions of applicability of the semi-analytic methods. It is shown that near the critical power the variational method is more accurate but as the initial power of the beam is increased, the variational method becomes less accurate and the paraxial method becomes more accurate. The analysis is applied to reconcile the behavior of the regularized phase which is defined as

the total longitudinal phase - the diffractive longitudinal phase. The numerical investigation shows that the regularized phase is monotonic in the propagation distance which is qualitatively different from the paraxial prediction. This result has consequences in pulse compression studies (i.e. a pulse cannot be compressed without the aid of external gratings).

The study of beam propagation in a Kerr Medium is extended to the propagation of elliptical gaussian beams. By varying the initial ellipticity of the beam from one to infinity, a careful analysis of the transition from 3D to 2D beam propagation is accomplished. The numerical results are compared to the semi-analytical methods in the literature and quantitative and qualitative differences are seen to occur. For example, for sufficiently high beam intensity, pulse splitting occurs along both axes of definition which cannot be explained in the abberationless schemes employed.

3) The propagation of femtosecond pulses in a resonant medium in which the carrier frequency is near to the transition frequency of the medium cannot be described by the Kerr model but requires coupling the inhomogeneous Maxwell wave equation to the optical Bloch equations which describe the evolution of the density matrix elements to an external excitation. From the Bloch equations, the material response (polarization) is determined and the Maxwell equation is well defined. The above method is applied to yield a rigorous model of a fiber amplifier (a fiber doped with an active ion concentration). The model describing the fiber amplifier includes the response of the fiber (including the higher order nonlinear and dispersive effects for femtosecond pulses) as well as the active two-

level medium. The model is applied to the study of an Erbium Doped Fiber Amplifier and is compared to approximate models of the amplifier. Quantitative and Qualitative differences in the temporal and spectral evolution are observed and explained.

4) The propagation of intense beams through material medium can cause higher order soliton states in a 2D geometry and Self-focusing in a 3D geometry. In reality, the Kerr medium approximation can be improved in applying the optical Bloch equations. If the beam is quasi monochromatic, the transient effects of the medium response vanish and a steady state theory is developed which accounts for nonlinear saturation and dispersion effects. In the 2D geometry, the propagation of the beam is shown to vary qualitatively as a function of detuning. In the 3D case, the self-focusing of the beam does not occur due to saturation effects. The high saturation is applied to waveguiding possibilities and it is shown that efficient waveguiding for intense pulses does indeed occur. The resonant results are compared to a variational treatment of the problem which neglects the absorption effects, only qualitative agreement is present.

5) The use of lasers as probes in quantifying the relevant relaxational processes of a particular transition are limited in resolution to the pulse duration of the optical pulse. This in turn fueled the search for compression techniques of optical pulses in the femtosecond regime. In general, the compression of coherent optical pulses require sophisticated experimental set ups including precision alignment of external gratings, etc. Recent theoretical and experimental work have shown that the fundamental limit to

ultrafast resolution experiments is in making wide spectral bandwidth sources. In the context of coherent pulses, the bandwidth and the pulse duration are transform limited but in incoherent pulses the bandwidth is transform limited to the coherence (correlation) time of the signal.

A numerical investigation of an intense incoherent signal propagating through a fiber is accomplished. This is motivated by work which shows that the Kerr effect on an incoherent pulse will compress the initial correlation time and that the compression is linear in the propagation distance. In real fibers, higher order nonlinear processes and dispersive effects cannot be neglected. The complexity of the resulting model requires a numerical approach. It is shown that dispersion limits the effective compression achievable and that the maximum compression increases with initial field intensity. Numerical simulations show that, for field intensities below material damage for a wavelength in the normal dispersive regime, final correlation times of a few femtoseconds is achievable which compares favorably with the shortest coherent pulses obtainable.

Due to the lack of pulsed lasers in the anomalous dispersion regime with the necessary intensity to yield effective correlation compression, we study the mathematically equivalent problem of an incoherent beam propagating in a Kerr medium. The anomalous dispersion is now spatial diffraction and the higher order effects have no corollary in the spatial environment. Applying the same numerical algorithm to the spatial problem, the correlation length compression is studied. It is shown that for an equivalent intensity, the anomalous dispersion would more effectively compress the

correlation time. Also, since this regime supports spatial solitons, qualitative differences in the dynamics of the correlation compression are manifested. These results agree well for small and large propagation distances with a simplified model used to describe the fiber.

9. Publications

[a] " Amplification of a Probe Propogating in a Pressure Self-Broadened Saturated Two-Level Atom System ", Physics Letters A . **157**, 14 (1991). - with J.T. Manassah

[b] " The Spectral Distribution and the Frequency Shift of the Super-continuum ", Physics Letters A **160**, 21 (1991). - with J.T. Manassah

[c] " Compressing the Coherence Time of Incoherent Signals to Few Femtoseconds ", Optics Letters **16**, 1835 (1991). - with J.T. Manassah

[d] " Modification of a Quasi-Monochromatic Beam Spatial Coherence Function through Propogation in a 2-Dimensional Kerr-Medium ", Optics Letters **17**, 166 (1992). - with J.T. Manassah

[e] " Numerical Solutions of the Maxwell-Bloch Equations for a Fiber Amplifier ", Optics Letters **17**, 340 (1992). - with J.T. Manassah

[f] " The Supercontinuum in the Anomolous GVD Regime ", J. Opt. Soc. Am. B **9** (1992). - with J.T. Manassah

[g] " Comparison of the Paraxial Ray Approximation and the Variational Method Solutions to the Numerical Results for a Beam Propagating in a Self-Focusing Kerr Medium ", Optics Letters **17**, 976 (1992). - with J.T. Manassah

[h] " Effects of Detuning of the Propagation of a 2D Beam in a Resonant Two-Level Medium ", Laser Physics (1992). - with J.T. Manassah

[i] " Waveguiding Efficiency of a 3D Beam Propogating in a Two-Level Medium ", Laser Physics (1992). - with J.T. Manassah

[j] " Numerical Solution of an Elliptic Gaussian Beam Propogating in a Kerr Medium", Physics Letters A **169**, 371 (1992). - with J.T. Manassah

References

1. N. Bloembergen and P.Lallemand, Phys. Rev. Lett. **16**, 81 (1966).

2. R.G. Brewer, Phys. Rev. Lett. 19, **8** (1967).

3. A.C. Cheung, D.M. Rank, R.Y. Chiao and C.H. Townes, Phys. Rev. Lett. **20**, 786 (1968).

4. W.J. Jones and B.P. Stoicheff, Phys. Rev. Lett. **13**, 657 (1964).

5. B.P. Stoicheff, Phys. Lett. 7, **186** (1963).

6. P. Lallemand, Appl. Phys. Lett. **8**, 276 (1966).

7. F. Shimuzu, Phys. Rev. Lett. **19**, 1097 (1967).

8. R.R. Alfano and S.L. Shapiro, Phys. Rev. Lett. **24**, 584,592,1219 (1970).

9. W.J. Tomlinson, R.H. Stolen and C.V. Shank, J. Opt. Soc. Am. **B1**, 139 (1984).

10. D. Grischowsky and A. Blatant, Appl. Phys. Lett. **41**, 1 (1986).

11. J.W. Goodman, Introduction to Fourier Optics. McGraw Hill, New York (1968).

12. E.B. Treacy, I.E.E.E. J. Quantum Electron. **QE-5**, 454 (1969).

13. O.A. Martinez, J.P. Gordon and R.L. Fork, J. Opt. Soc. Am. **A1**, 1003 (1984).

14. H. Nakatsuka and D. Grishchowsky, Opt. Lett. **6**, 13 (1981).

15. B. Nikolaus and D. Grischowsky, Appl. Phys. Lett. **43**, 228, (1983).

16. R.L. Fork, C.H. Brito Cruz, P.C. Becker and C.V. Shank, Opt. Lett. **12**, 483 (1987).

17. R.L. Fork, C.V. Shank, C. Hirlman and R.Yen, Opt. Lett. **8**, 1 (1983).

18. F.M. Mitschke and L.F. Mollenauer, Opt. Lett. **11**, 659 (1986).

19. F. DeMartini, C.H. Townes, T.K. Gustafson and P.L. Kelley, Phys. Rev. **164**, 312 (1967).

20. G.Z. Yang and Y.R. Shen, Opt. Lett. **9**, 510 (1984).

21. Y.R. Shen and G.Z. Yang, " The SuperContinuum Laser Source", Chapt 1, R.R. Alfano Ed: (1989).

22. J.P.Gordon Opt. Lett. **11**, 662 (1986).

23. J.T. Manassah, M.A. Mustafa, R.R. Alfano and P.P. Ho, I.E.E.E J. Quantum Electron. **QE-22**, 197 (1986).

24 J.T. Manassah and M.A. Mustafa, Phys. Lett. A. **133**, 51 (1988).

25. J.T. Manassah and M.A. Mustafa, J. Opt. Soc. Am. **B6**, 1258 (1989).

26. R.H. Stolen, J.P. Gordan, W.J. Tomlinson and H.A. Haus, J. Opt. Soc. Am. **B6**, 1159 (1989).

27. R.A. Fischer and W. Bischel, J. Appl. Phys. **46**, 4921 (1975).

28. R.A. Fischer, B.Suydam and D. Yevich, Opt. Lett. **8**, 611 (1983).

29. V.E. Zakharov and A.B. Shabat, Sov. Phys. JETP **34**, 62 (1972).

30. A. Hasegawa and F. Tappert, Appl. Phys. Lett. **23**, 142 (1973).

31. P.L. Francois, J. Opt. Soc. Am. **B8**, 276 (1991).

32. Y.R. Shen and N.N. Bloembergen, Phys. Rev. **137A**, 1787 (1965).

33. L.F. Mollenaur, R.H. Stolen and J.P. Gordon, Phys. Rev. Lett. **45**,1095 (1980).

34. W.Hodel and H.P. Weber, Opt. Lett. 12, 924 (1987). In this paper, the linear form of the Raman susceptibility and the expression for self-steepening obtained from the S.V.E.A approximation (2 times our value) are used.

35. R. Y. Chiao, E. Garmire and C.H. Townes, Phys. Rev. Lett. **13**, 479 (1964).

36. P.L. Kelley, Phys. Rev. Lett. **15**, 1005 (1965).

37. J.H. Marburger, Jr. Prog. Quantum Electron. **4**, 35 (1975).

38. J.T. Manassah, P.L. Baldeck and R.R. Alfano, Opt. Lett. **13**, 589,1090 (1988).

39. J.T. Manassah, Opt. Lett. **14**, 396 (1989).

40. D. Anderson, Phys. Rev. A **27**, 3135 (1983).

41. M. Karlson, D. Anderson, M. Desaix and M. Lisak, Opt. Lett. **16**, 1373 (1991).

42. M. Desaix, D. Anderson and M.Lisak, J. Opt. Soc. Am. **B8**, 2082 (1991).

43. J.T. Manassah, Opt. Lett. **16**, 563 (1991).

44. Y. Silberberg, Opt. Lett. **15**, 1282 (1990).

45. E.L. Dawes and J.H. Marburger, Phys. Rev. **179**, 862 (1968).

46. M.G. Boshier and W.S. Sandle, Opt. Comm. **42**, 371 (1982).

47. M.D. Feit and J.A. Fleck Jr., J. Opt. Soc. Am. **B5**, 633 (1988).

48. J.S. Aitchinson, A.M. Weiner, Y. Silberberg, M.K. Oliver, J.L. Jackel, D.E. Leaird, E.M. Vogel and P.W.E. Smith, Opt. Lett. **15**, 471 (1990).

49. F. Reynaud and A. Barthelemy, Europhys. Lett. **12**, 5 (1990).

50. V.V. Vorob'ev Izv. Vys. Uch. Zav. Radiofizika **13**, 1905 (1970).

51. C.R. Giuliano, J.H. Marburger and A. Yariv, Appl. Phys. Lett. **21**, 58 (1972).

52. F. Cornolti, M. Lucchesi and B. Zambon, Opt. Comm. **75**, 192 (1990).

53. A.M. Goncharenko, Yu. A. Logvin, A.M. Samson and P.S. Shapovalov, Opt. Comm. **81**, 225 (1991).

54 A.M. Goncharenko, Yu. A. Logvin, A.M. Samson, P.S. Shapovalov and S.I. Turovets, Phys. Lett. A **160**, 138 (1991).

55. V.P. Ermakov, Univ. Izv. Kiev **20**, 1 (1980).

56. R.P. Feynman, F.L. Vernon and R.W. Hellwarth, J. Appl. Phys. **28**, 49 (1957).

57. L.I. Schiff, "Quantum Mechanics" 3rd Ed. McGraw Hill New York, (1968).

58. F. Bloch, Phys. Rev. **70**, 460 (1946).

59. Y.R. Shen, " Principles of Non-Linear Optics" , Chapt. 21; John Wiley & Sons (1984).

60. S.L. McCall and E.L. Hahn, Phys. Rev. Lett. **18**, 908 (1967). Phys. Rev **183**, 457 (1969).

61. R.H. Dicke, Phys. Rev. **93**, 99 (1954).

62. P. A. Bélanger, L. Gagnon, and C. Paré, Opt. Lett. **14**, 943 (1989).

63. B. J. Ainslie, K. J. Blow, A. S. Gouveia-Neto, P. G. J. Wigley, A. S. B. Sombra, and J. R. Taylor, Electron. Lett. **26**, 186 (1990).

64 A. B. Grudinin, E. M. Dianov, D. V. Korobkin, A. Yu. Makerenko, A. M. Prokhorov, and I. Yu. Khrushchev, JETP Lett. **51**, 135 (1990).

65. G. P. Agrawal, Opt. Lett. **16**, 226 (1991).

66. I. V. Melnikov, R. Nabiev and A. V. Nazarkin, Opt. Lett. **15** , 1348 (1991).

67. L. Gagnon and P. A. Bélanger, Phys. Rev. A **43** , 6187 (1991).

68. V. Petrov and W. Rudolph, Opt. Comm. **76**, 53 (1990).

69. M. Nakazawa, E. Yamada and H. Kubota, Phys. Rev. Lett. **66**, 2625 (1991).

70. T. Y. Wang and S. Chi, Opt. Lett. **16**, 1575 (1991).

71. I. Yu. Kruschev, A.B. Grudinin, E.M. Dianov, D.V. Korobkinjun, V.A. Semenov and A.M. Prokhorov, Elect. Lett. **26**, 456 (1990).

72. M. Nakazawa, K,Kurokawa, H. Kubota, K. Suzuki and Y. Kimura, Appl. Phys. Lett. **57**, 659 (1990).

73. G.P. Agrawal, I.E.E.E. Phot. Tech. Lett. **2**, 875 (1990).

74. E. Courtens, Laser Handbook V.2 eds. F.T. Arecchi and E.O. Schulz-Dubois (North-Holland, Amsterdam, 1972).

75. W. G. Wagner, H. A. Haus, and J. H. Marburger, Phys. Rev. **175**, 256 (1968).

76. M. LeBerre, E. Ressayre, A. Tallet, K. Tai, H. M. Gibbs, M. C. Rushford and N. Peyghambarian,J. Opt. Soc. Am. **B1** , 591 (1984).

77. M. LeBerre, E. Ressayre, and A. Tallet, Phys. Rev. A **29**, 2669 (1984); 78. M. LeBerre, E. Ressayre, A. Tallet, and F. P. Mattar, J. Opt. Soc. of Am. **B2**, 957 (1985).

79. A. W. McCord, R. G. Ballagh, and J. Cooper, J. Opt. Soc. of Am. **B5**, 1323 (1988).

80. R. Beach and S. R. Hartmann, Phys. Rev. Lett. **53**, 663 (1984).

81. S. Asaka, H. Nakatsuka, M. Fujiwara and M. Matsuoka, Phys. Rev. A **29**, 2286 (1984).

82. N. Morita and T. Yajima, Phys. Rev. A **30**, 2525 (1984).

83. J. T. Manassah, Opt. Lett.**15**, 329 (1990).

84. M. T. de Araujo, H. R. da Cruz, and A. S. Gouveia-Neto, J. Opt. Soc. Am. B**8**, (1991).

85. N. Wax (Ed.): Noise and Stochastic Processes (Dover, New York,1954).

86. See for example, A. Papoulis, Probability, Random Variables, and Stochastic Processes (McGraw-Hill, New York, 1984).

87. L. Scharf, Statistical Signal Processing (Addison Wesley: Reading 1990).

88. J.T. Manassah, Opt. Lett. **16**, 1638 (1991).

89. A. C. Schell, Ph.D. Thesis, MIT (1961).

90. V.I. Karpman and E.M. Krushkal, Sov. Phys. JETP **28**, 277 (1969).

91. N. Yajima and A. Outi, Prog. Theor. Phys. **45**, 1997 (1971).

92. R.A. Fischer and W.K. Bischel, Appl. Phys. Lett. **23**, 661 (1973).

93. M.J. Ablowitz and J.F. Ladik, Stud. Appl. Math. **55**, 213 (1976).

94. I.S. Greig and J.L. Morris, J. Comp. Phys. **20**, 60 (1976).

95. B. Fornberg and G.B. Whitham, Phil. Trans. Roy. Soc. **289**, 373 (1978).

96. M. Delfour, M. Fortin and G. Payre, J. Comp. Phys. **44**, 277 (1981).

97. G.P. Agrawal, NonLinear Fiber Optics (London: Academic Press 1989)

98. G.H. Weiss and A.A. Maradudin, J. Math. Phys. **3**, 771 (1962).

99. J.A. Fleck, J.R. Morris and M.D. Feit, Appl. Phys. Lett. **10**, 129 (1976).

100. J.R. Rice Numerical Methods, Software and Analysis, (New York: McGraw Hill 1983).

101. H.J. Nussbaumer, Fast Fourier Transform and Convolution Algorithms, (New York: Springer Verlag 1982).

102. D.F. Elliot and K.R. Rao, Fast Transforms, Algorithms, Analyses and Applications, (New York: Academic Press 1982).

103. E.O. Brigham, The Fast Fourier Transform, (Englewood Cliffs N.J. Prentice Hall 1974).

104. L. Rabiner and R. Schafer, Digital Signal Processing - Theory and Applications, (Englewood Cliffs N.J. Prentice Hall 1975)

105. W.H. Press, B.P. Flannery, S.A. Teukolsky and W.T Vetterling, Numerical Recipies - The Art of Scientific Computing, (Cambridge University Press 1986).

106. W.C. Gear, Numerical Initial Value Problems in Ordinary Differential Equations, (Englewood Cliffs N.J. Prentice Hall 1974).